Building Integrated Cell-based Microsystems – Fabrication Methodologies, Metrology Tools and Impact on Cellular Physiology

by

Salil P. Desai

B. S. Electrical and Computer Engineering
Carnegie Mellon University, 2000
S. M. Electrical Engineering and Computer Science
Massachusetts Institute of Technology, 2002

SUBMITTED TO THE DEPARTMENT OF ELECTRICAL ENGINEERING AND COMPUTER SCIENCE IN PARTIAL FULFILLMENT OF THE REQUIREMENTS FOR THE DEGREE OF

DOCTOR OF PHILOSOPHY IN ELECTRICAL ENGINEERING AND COMPUTER SCIENCE
AT THE
MASSACHUSETTS INSTITUTE OF TECHNOLOGY

JUNE 2009

Signature of Author _____
Department of Electrical Engineering and Computer Science
May 20, 2009

Certified by: _____
Joel Voldman
Associate Professor of Electrical Engineering and Computer Science
Thesis Supervisor

Accepted by: _____
Terry P. Orlando
Professor of Electrical Engineering and Computer Science
Chairman, Committee for Graduate Students

Building integrated cell-based microsystems: Fabrication methodologies, metrology tools and impacts on cellular physiology

by

Salil P. Desai

Submitted to the Department of Electrical Engineering and Computer Science in partial fulfillment of the requirements for the Degree of Doctor of Philosophy in Electrical Engineering and Computer Science

ABSTRACT

This thesis presents the development of new tools for the realization and characterization of complex, integrated biological microsystems. These tools involve – (1) the implementation and characterization of a new material system for biological microsystems, and its application to the design of a single-bioparticle trap, (2) the creation of a lipid vesicle-based metrology tool for the characterization of dielectrophoresis-based microsystems, and (3) the construction of live-cell stress reporters for the characterization of electric-field effects on cell physiology in microsystems. .

Materials for biological microsystems have been dominated by the elastomer polydimethylsiloxane (PDMS) and the photopolymer SU-8 which form the core of soft lithography based fabrication. The design of highly integrated microsystems in which microfluidic conduits are coupled with electrical manipulation techniques, however, is difficult to realize with soft lithography. This thesis presents a new fabrication technique based on photopatternable silicones. I show that these photopatterned silicones are able to generate free-standing structures, exhibit low autofluorescence, enable alignment with pre-patterned substrates, and are biocompatible. These unique properties enable the generation of a new type of single-particle trap, which would be challenging to realize using traditional techniques. This new material system is now well poised to enable the design and construction of new biological microsystems that could not be previously realized.

In addition to new material systems and fabrication technology, designing highly integrated cell-based biological microsystems requires the use of synthetic, cell-like particles. To date, polystyrene microspheres have served as surrogates for cells in characterizing these systems, despite the fact that they serve as poor models of cells. This thesis presents a new metrology tool for the characterization of microsystems, based on phopsphohlipid vesicles. I show the ability to modulate the electrical properties of such vesicles and generate electrically addressable vesicles and for use in the characterization of dielectrophoretic-based microsystems.

Finally, as biological microsystems gain in complexity, the need to characterize their impact on living cells is of paramount importance. This thesis presents the construction of stress reporting cell lines that form the core of live-cell metrology tool for assaying physiological impact in Microsystems that utilize electric fields to manipulate cells. Specifically, the response of these stress reporter cells to conditions typically experienced in a dielectrophoretic trap are explored over a wide range of voltages, frequencies and durations. The results obtained point to the role of multiple stressing agents and provide new insight in to stress initiation across frequency. The use of such sensors is now well poised to study the physiological impact of microsystems across a wide range of conditions. Together, the tools presented in this thesis promise to enable the development of systems with unprecedented flexibility of design as well as functionality.

Thesis Supervisor: Joel Voldman
Title: Associate Professor of Electrical Engineering and Computer Science

ACKNOWLEDGEMENTS

My name appears on this thesis but this was by no means an individual effort. I am deeply indebted to Joel Voldman for letting me pursue my ideas (even though at first they showed little promise) and for putting up with my irrational habit of disregarding deadlines. My thesis committee members, Sangeeta Bhatia and Frank McKeon were exceedingly kind and were always willing to help out with technical issues. Amongst members of the Voldman Lab, I owe many thanks to Mike Vahey for his keen intellect and ability to seamlessly bridge the experimental and theoretical worlds. Much of this work has been heavily influenced by discussions with Mike, especially the work on electrically addressable vesicles which would never have reached fruition without his tremendous help and dedication. I look forward to continue getting his advice and working with him again in the future. Brian Taff deserves extra special mention, his insanely methodical approach has been an inspiration and the hours spent in the fab making "pachinkos" were both entertaining and rewarding. It was always good to know he would be willing to push the limits, and I aspire to emulate his attitude when trying to get the job done. "Pat" Sampattavanich is a stem cell guru and a true friend, I hope to see him reach the heights of science and fulfill his tremendous potential. Katarina Blagovic has added levity to my work and made the lab a more boisterous environment to be in. I have enjoyed working with her and greatly appreciate her willingness to help out, no matter what the task. Joseph Kovac has been an impressive perfectionist who seems unperturbed by the stresses of research, I only wish I could get work done so effortlessly. I hope his passion for mountaineering continues and he reaches the Roof of the World some day. I greatly admire Nick Mittal's ability to balance work and enjoy life, his probing questions have made me think more deeply about my work. As for newer members of the lab – Laralynne Pryzbyla, Yi-Chin Toh, Melanie Hoehl, and Wei-Mong Tsang, I have enjoyed very much hanging out with them and hope to hear of their deserved successes as they continue their research. I owe special thanks to my former advisors, Kaigham "Ken" Gabriel and Denny Freeman for their advice through various stages of my career. I would never have made it through MIT without their help and belief in my ability. Luke Theogarajan provided great technical advice and constant needling to make sure I didn't continuously pursue random projects, his hard questions were always annoying and made me squeamish, but in the end made sure I wasn't being to cavalier in my research work.

I am indebted to my family for their support over the years. I hope that I could my education to good use and maybe even use it to help others. I am continuously amazed and inspired by my brother, Ravi, whose brilliant mind I have always admired, I wish I had been able to share more of my experiences with him and look forward to the day when we live in the same city again. Finally, I thank my parents for their love and support over the years.

TABLE OF CONTENTS

Chapter 1 – Introduction 11
1.1 Biological Microsystems 11
1.2 Fabrication technologies 12
1.3 Measuring physiological impact of biological microsystems 13
1.4 Generalized metrology tools for biological microsystems 14
1.5 Scope and organization of the thesis 15
Chapter 2 – Fabrication Technologies 16
2.1 INTRODUCTION 16
2.2 RESULTS 18
2.2.1 Feature resolution 18
2.2.2 Free-standing structures 19
2.2.3 Biocompatability 20
2.2.4 Autofluorescence 20
2.2.5 Multi-level alignment fidelity 21
2.2.6 Functional device operation 22
2.2.7 Single bio-particle traps 23
2.2.8 Descum process for PPS 23
2.3 DISCUSSION 23
2.4 CONCLUSIONS 26
2.5 MATERIALS & METHODS 26
2.6 ACKNOWLEDGEMENTS 29
2.7 SUPPLEMENTARY INFORMATION 30
2.7.1 Spin curve data 30
2.7.2 Residual On-chip Thin Films 30
2.7.3 Additional Processing Details 34
2.7.4 BioMEMS materials choices 35
2.7.5 Free-standing microstructures 36
Chapter 3 – Vesicle-based metrology tools 37
3.1 INTRODUCTION 37
3.2 RESULTS: 39
3.2.1 Creating EAVs 39
3.2.2 Controlling EAV size 40

3.2.3 EAVs as test particles 41
3.2.4 Determining membrane characteristics from cross-over frequency. 42
3.2.5 Modulating membrane capacitance 44
3.3 DISCUSSION 44
3.4 CONCLUSIONS 47
3.5 MATERIALS AND METHODS 48
3.6 ACKNOWLEDGEMENTS 49
3.7 SUPPLEMENTARY INFORMATION 50
3.7.1 EAV core conductivity sensitivity 50
3.7.2 Vesicle purification techniques 50
3.7.3 PEGylated EAV image processing 51
3.7.4 Lipid patterning 52
Chapter 4 – Electric-field Impact on Cellular Physiology 53
4.1 INTRODUCTION 53
4.2 Hypotheses and Objectives 54
4.3 Dielectrophoresis (DEP) 55
4.4 Electric field effects on cells 56
4.4.1 Thermal effects and cellular stress 56
4.4.2 Direct cell-field interactions 57
4.4.3 Electrochemical Effects 59
4.4.4 Migratory Effects 59
4.5 Prior studies 60
4.6 Assaying physiological state 62
4.7 Assay platforms 65
4.8 Assay methodology 66
4.9 RESULTS 66
4.10 DISCUSSION 68
4.11 CONCLUSIONS 69
4.12 MATERIALS & METHODS 69
4.13 ACKNOWLEDGEMENTS 73
4.14 SUPPLEMENTARY INFORMATION 74
4.14.1 Blocking buffers for immunofluorescence assays 74
4.14.2 RNA extraction protocol using QIAGen RNeasy kit 74
4.14.3 Primers for PCR 75

4.14.4 Protocols for PCR 75
4.14.5 Image processing algorithm for image cytometry 76
4.14.6 PEG-thiol methods and results 77
4.14.7 Polystyrene patterning methods and results 78
Chapter 5 – Live-cell based metrology tools 80
5.1 INTRODUCTION 80
5.2 RESULTS 83
5.2.1 Single cell cloned reporter cell line 83
5.2.2 Microfabricated platform 83
5.2.3 Image cytometry 84
5.2.4 Voltage sweep 85
5.2.5 Frequency sweep 85
5.2.6 Membrane loading 87
5.2.7 Reactive species generation 87
5.2.8 MCF-10A verification assays 88
5.3 DISCUSSION 88
5.4 CONCLUSIONS 89
5.5 MATERIALS & METHODS 89
5.6 ACKNOWLEDGEMENTS 98
5.7 SUPPLEMENTARY INFORMATION 98
5.7.1 Western Blotting buffers and protocol 98
5.7.2 Plasmid Maps 100
5.7.3 Modeling 101
5.7.4 Plasmid purification 102
5.7.5 Ringer's Solution 103
5.7.6 Resistor calibration 103
5.7.7 Autofocus routines 104
Chapter 6 - Conclusions 105
6.1 Thesis contributions 105
6.2 Perspectives on future work 107
6.2.1 Fabrication technologies 107
6.2.2 Vesicle-based metrology tools 109
6.2.3 Live-cell metrology tools for biological microsystems 111
6.2.4 High-content screening platform 113

6.2.5 Electric field impact on cellular physiology 114
References 116

TABLE OF FIGURES

Figure 1-1: Thesis objectives overview. 12
Figure 2-1: Motivation for the design of new single-cell traps 17
Figure 2-2: PPS sidewall angle and resolution. 18
Figure 2-3: Free-standing microstructures. 19
Figure 2-4: Biocompatability. 20
Figure 2-5: Autofluorescence. 21
Figure 2-6: Alignment and cell-patterning. 22
Figure 2-7: Single bio-particle traps. 22
Figure 2-8: Descum process results. 23
Figure 2-9: Spin curves. 30
Figure 2-10: Residual PPS films. 30
Figure 2-11: Electrical model. 31
Figure 2-12: Impact of residual PPS films. 34
Figure 2-13: Biological microsystems materials choices. 35
Figure 2-14: Free-standing PPS microstructures. 36
Figure 3-1: Vesicle electroformation. 38
Figure 3-2: Electrically addressable vesicles. 39
Figure 3-3: Controlling EAV Size 40
Figure 3-4: EAVs as test particles. 41
Figure 3-5: Modulating membrane thickness. 43
Figure 3-6: EAV core conductivity sensitivity. 50
Figure 3-7: Vesicle purification techniques. 50
Figure 3-8: Imaging PEGylated EAVs. 51
Figure 3-9: Lipid patterning. 52
Figure 4-1: Dielectrophoretic trapping. 55
Figure 4-2: Lumped element electrical model of the cell. 57

Figure 4-3: Cellular stress response 63
Table 4-1: Probes for physiological state 64
Figure 4-4: Microfabricated assay platform. 65
Figure 4-5: Assay methodology. 65
Figure 4-6: Immunofluorescence and image cytometry. 66
Figure 4-7: Gene expression assays. 66
Figure 4-8: Kinase assay. 67
Figure 4-9: Cells on electrodes. 67
Figure 4-10: Amplicon sizes. 75
Figure 4-11: PEG-thiols 77
Figure 4-12: Polystyrene patterning 78
Figure 5-1: Electrical perturbation of cells. 80
Figure 5-2: HSP70 pathway. 81
Figure 5-3: Stress reporter clones. 82
Figure 5-4: RT-PCR results. 83
Figure 5-5: Fabricated device and platform. 83
Figure 5-6: Quantitative imaging. 84
Figure 5-7: Frequency sweep. 85
Figure 5-8: Voltage sweep. 85
Figure 5-9: Frequency sweeps. 86
Figure 5-10: Membrane polarization assay 87
Figure 5-11: ROS assay. 87
Figure 5-12: MCF-10A reporter results. 88
Figure 5-13: Fabrication processes. 93
Figure 5-14: Electrical stimulation setup. 95
Figure 5-15: Quantitative microscopy. 96
Figure 5-16: Western blot. 99

Figure 5-17: pDsRed map. 100
Figure 5-18: pY9 plasmid map. 101
Figure 5-19: Model for transmembrane potential. 102
Figure 6-1: Vesicles for membrane metrology. 110
Figure 6-2: BA/F3 reporter cells. 112
Figure 6-3: Blue fluorescent fibroblasts. 113

Chapter 1 – **Introduction**

In this chapter I will begin with an overview of microsystems technology as applied to biological sciences with an emphasis on some of the challenges facing the development and use of this technology. This will lead to the introduction of the main themes of this thesis – from biological microsystems fabrication techniques to metrology tools and the characterization of the physiological impact of these microsystems on living cells. Next, I will present the need to integrate new materials and fabrication techniques to develop microsystems for the manipulation of single cells. This leads to the compelling question of how such complex biological microsystems might impact cellular physiology. I will then provide an overview of the current techniques that encompass biological microsystems metrology. Generalized metrology tools have an important place in biological microsystems, however, the use of live-cell metrology tools are increasingly important for studying the direct impact of microsystems on overall cellular health and function. The use of such types of live-cell reporter systems will be discussed. Finally, I will conclude with an outline for the rest of the thesis and the scope of the work presented herein.

1.1 Biological Microsystems

Biological microsystems or bioMEMS are used for the capture, processing and analysis of biological entities. As these microsystems can leverage both conventional microfabrication and soft-lithography-based fabrication techniques they are used in conjunction with a wide range of biological entities spanning the size spectrum of individual proteins [3], to bacterial and yeast cells [4, 5] to mammalian cells [6, 7] and even multi-cellular colonies [8].

This thesis is focused on cell-based microsystems, and specifically with microsystems for use with mammalian cells. Systems for manipulating mammalian cells have significant implications for both fundamental biology and biotechnology. The development of these microsystems has been the subject of considerable past study. Three-dimensional cell organization and cell culture have been performed in biological microsystems by the integration of complex cell ensembles [9], engineered scaffolds to guide cell proliferation [10], and microfluidic perfusion systems for transport of nutrients and other soluble factors [11]. These soluble factors, for example, cytokines, can be presented to the cells in complex spatiotemporal patterns using integrated microfluidic systems [12]. In addition to positioning and stimulating cells, biological microsystems technology can perform complex phenotypic sorts on heterogeneous cell populations into more homogeneous populations [13]. Such sorts can be performed with techniques that enable single-cell selection [14], where different cell types can be analyzed separately. Biological microsystems have considerable flexibility in the incorporation of techniques for the analysis of both biochemical reactions within living cells and techniques for gene and protein-level analysis of cell lysates [15]. These considerable applications of biological

microsystems are achieved by leveraging mature technologies in microfabrication. This makes microfabrication an invaluable tool in the study of fundamental cell biology.

Cell-based microsystems have matured greatly over the past decade and are beginning to prove competitive with standard benchtop systems. Although significant challenges face routine applications of biological microsystems that in effect integrate cells on chips, a future in which chips effectively compete with laboratory-scale technologies in the analysis of complex biological phenomena is clearly in sight [16]. Highly integrated cell-based microsystems are poised to find applications in basic biomedical and pharmaceutical research, whereas cost-effective and disposable microsystems could be used as platforms for processing clinically-relevant samples and as point-of-care devices.

Realizing this potential requires further innovation in three primary areas: the ability to fabricate a wider array of features with a wider array of materials; improved understanding of how the system itself may be perturbing the sample under study; and better tools to optimize the design and operation of these systems. To this end, the objectives of this thesis are summarized in Figure 1-1.

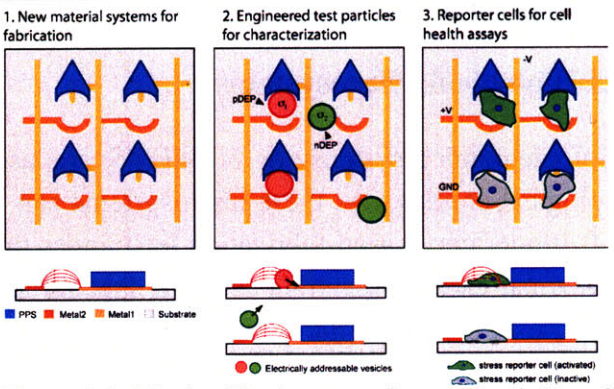

Figure 1-1: Thesis objectives overview. The design of integrated systems requires the use of new types of material systems (blue, left panel). The integration and processing of such material systems enables new architectures. The development of electrically distinct cell surrogate particles (middle panel) enables the testing of microsystems over a wide range of physiological conditions (a feat challenging to achieve with current techniques). Finally, the use of live-cell stress reporters (right panel) enables studying the impact of microsystems on cellular physiology and provides guidelines to the types of assays that can be performed.

1.2 Fabrication technologies

The capture, processing and analysis of single cells have important implications for fundamental biological research and biotechnology. Studying a population of single cells provides unique information about cell behavior that is difficult to obtain using standard biological assays, which report ensemble behaviors. The subsequent capture of unique cells from this single-cell population of cells presents important implications for studying mutants and is important for downstream biological analysis. However, this paradigm of single-cell analysis requires the fabrication of robust systems in which the cells can be easily loaded, arrayed, and addressed.

Single-cell capture systems typically involve the sequestering of a large array of cells using either electrical or hydrodynamic trapping techniques. Hydrodynamic techniques are passive and therefore difficult to address at a single site level. Electrical systems provide addressability but building arrayed, addressable single-cell traps that function in physiological media presents a significant technological challenge. This thesis directly addresses this challenge by presenting

new materials and fabrication technologies that enable the realization of unique single-cell trap architecture.

The need for new fabrication technologies and materials stems from the fact that polydimethylsiloxane (PDMS) or other elastomeric materials (such as RTV) molded using soft lithography suffer from several limitations – (1) high-aspect-ratio structures are susceptible to mechanical collapse, (2) wafer-scale integration and micron-scale alignment with patterned substrates is challenging, and (3) free-standing, mechanically isolated microstructures are difficult to realize. Further, while PDMS films can be spun cast onto wafers, they are not easily directly patterned using conventional photolithographic techniques. Past work in developing photopatternable PDMS has involved adding photoinitiators to conventional PDMS pre-polymer or custom synthesis of polymers with inherent photopatterning capabilities and enhanced feature resolution [17-19]. However, these techniques either do not provide the feature resolution required for single-cell capture or require considerable custom synthesis. The limitations of soft lithography point to the need for integration of a new material system, a photopatternable silicone that encompasses the advantageous features of both photoresists and silicones in the construction of highly-integrated biological microsystems. This thesis describes the processing and characterization of such a photopatterned silicone and highlights its capabilities in the context of the design of a single-cell trap.

1.3 Measuring physiological impact of biological microsystems

Important to the design and adoption of cell-based microsystems is knowledge of how these systems themselves alter cell state. Such measurements can be difficult to perform, primarily due to the difficulty in performing conventional molecular biology assays with limited numbers of cells in micro-scale devices. As a result, assays to measure the impact of microsystems on cell physiology are typically limited to general characteristics such as viability, morphology, and growth. As biological microsystems increase in complexity and in the fidelity of the assays they perform, it's imperative that techniques for measuring the physiological impact of such systems be developed.

The measurement of such physiological impact is important for two main reasons – (1) to understand the operating regimes of the system that have minimal physiological impact for cells, and (2) to determine whether such physiological effects might confound downstream biological analysis. This thesis lays the foundation for the development of cell-based stress sensor that can be used as a canonical cell line for studying physiological in a wide variety of microsystems. The sensor was specifically characterized in the context of electric-field generated stresses as a means for understanding the physiological impact of dielectrophoretic cell manipulation.

The work presented in this thesis explores the use of this sensor as a means for studying the impacts of electric field manipulation. However, a more general scheme of using such a sensor can be envisioned in the context of understanding various impacts of a microsystem. For example, in the case of perfusion-based microsystem, shear stresses would be important to measure. The development of such a live-cell-based measurement systems has important implications for testing physiological conditions within microsystems. The characterization of microsystems has lead to the design of generalized tools for the measurement of key parameters within a microsystem.

1.4 Generalized metrology tools for biological microsystems

To be effective, microsystems typically require careful design across multiple physical domains. Accordingly, in addition to the challenge of characterizing the biological impact of a microsystem, there is also the challenge of characterizing its physical operation, so that it may be optimally designed.

Cell-based biological microsystems involve the manipulation, measurement, culture and separation of cells. This means that effective techniques to characterize such systems necessitate the use of cells. The impact of the microsystem on cells is an important aspect of the characterization but does not form a general means for the characterization of such a system. This thesis explores the first steps for the creation of more generalizable metrology tools for microsystems that could serve as cell surrogates and characterize microsystems. These surrogates are built from lipid vesicles that form simple structures for the use. Such surrogate particles have several advantages over live cells – (1) have exquisite control over electromechanical properties, (2) can be generated on-demand with specific fluorescent signatures, and finally, (3) do not have physiological environment constraints and can be used over a wide range of microsystem operating conditions. To date such surrogate particles have seen limited use in microsystems and have been used for studying flow profiles in microsystems [20].

This thesis presents the first steps to the creation of electrically addressable test particles. I will show the use of phospholipid vesicle electroformation techniques to develop a new class of metrology tools with specifically engineered electrical properties to enable identifiable dielectrophoretic responses in microfabricated systems. These electrically addressable vesicles (EAVs) enable the creation of electrically distinct populations of test particles for dielectrophoresis. EAVs offer control of both their inner aqueous core and outer membrane properties; by encapsulating solutions of different electrolyte strength inside the vesicle and by incorporating functionalized phospholipids containing PEG brushes attached to their hydrophilic head group in the vesicle membrane, I demonstrate control of the vesicles' electrical polarizabilities. This combined with the ability to encode information about the properties of the vesicle in its fluorescence signature, form the first steps toward the development of EAV

populations as metrology tools for any dielectrophoresis-based microsystem. Indeed, the development of such test particles could prove synergistic with the ability to understand the physiological impact by making in situ measurements of dielectrophoretic or optical traps which could provide valuable information about the environment within such traps.

1.5 Scope and organization of the thesis

This thesis describes fabrication techniques used to realize fundamentally new biological microsystems, metrology tools to interrogate such systems and live-cell reporters to determine the impact of such systems in the context of live cell manipulations. The results are presented in the form of a series of papers that have been published (as in Chapters 2 and 3) or are to be published (as in Chapter 5) in different scientific or engineering journals. As such, the following chapters are self-contained, which implies a certain duplication of information, particularly in the methods and introduction sections. The readers' assumed background varies somewhat from chapter to chapter, in large part owing to the different audiences reached by different journals. Chapter 2 presents the characterization of a new material system for biological microsystems. This photopatterned silicone material is characterized and applied to the design of a new type of single, bioparticle trap. Chapter 3 presents the development of a metrology tool for characterizing dielectrophoresis-based microsystems. This metrology tool is based on phospholipid-based giant vesicles which can be tuned to exhibit a wide range of electrical responses. Chapter 4 presents the background of electric-field effects on cells and the types of assays that could potentially be used to determine the physiological state of a cell after it has been electrically manipulated. Initial results of a dielectrophoresis system for electrical trapping and stimulating cells along with preliminary results are presented. Chapter 5 provides the design, implementation and results obtained from a more high-throughput system for electrical stimulation of cells. Chapter 6 includes concluding remarks and perspectives on future work.

Chapter 2 – **Fabrication Technologies**

This chapter describes the characterization of a new material system for cell-based biological microsystems and its application to the construction of a single-bioparticle trap. I show the application of a commercially available photopatternable silicone (PPS) that combines the advantageous features of both PDMS and SU-8 to address a critical bioMEMS materials deficiency. Using PPS I have demonstrated the ability to pattern free-standing mechanically isolated elastomeric structures on a silicon substrate; a feat challenging to accomplish using soft lithography-based fabrication. PPS readily integrates with many cell-based bioMEMS since it exhibits low-autofluorescence and cells easily attach and proliferate on PPS-coated substrates. Due to its inherent photopatternable properties, PPS is compatible with standard microfabrication processes and easily aligns to complex featured substrates on a wafer-scale. By leveraging PPS's unique properties, I demonstrate the design of a simple dielectrophoresis-based bioMEMS device for patterning mammalian cells. Additionally, PPS is used in the design of a new class of single bioparticle traps that combine the benefits of passive, hydrodynamic loading and active, dielectrophoretic unloading. The key material properties and integration capabilities explored in this work should present new avenues for exploring silicone microstructures for the design and implementation of increasingly complex bioMEMS architectures.

The results presented in this chapter have been previously published in *Langmuir* and *Applied Physics Letters* [1, 21]. This chapter extends on this previous work and provides additional processing and methods details on methods as well as additional results not previously reported. It is important to note that the experiments and processing performed here were performed in collaboration with Brian M. Taff.

2.1 INTRODUCTION

Polydimethylsiloxane (PDMS) has emerged as one of the most commonly used bioMEMS materials because it displays low autofluorescence, presents well-characterized biocompatibility [22, 23], and molds with reasonably high resolution [24]. PDMS devices are most commonly molded from photolithographically defined masters using either positive- or negative-tone photoresists, in a process termed soft lithography. Consequently, the geometry of PDMS structural features is defined by the resolution and fabrication constraints of the photoresist used when manufacturing the master. Moreover, PDMS or other elastomeric materials (such as RTV) molded using soft lithography suffer from several limitations – (1) high-aspect-ratio structures are susceptible to mechanical collapse, (2) wafer-scale integration and micron-scale alignment with patterned substrates is challenging, and (3) free-standing, mechanically isolated microstructures are difficult to realize. Further, while PDMS films can be spun cast onto wafers, they are not easily directly patterned using conventional photolithographic techniques. Past work in developing photopatternable PDMS has involved adding photoinitiators to conventional PDMS (Sylgard 184) pre-polymers [17, 25] or custom synthesis of polymers with inherent

photopatterning capabilities and enhanced feature resolution [19]. None of these photopatternable PDMS formulations are commercially available. To avoid synthesizing photopatternable PDMS, SU-8 has been used as a photolithographically defined film to produce free-standing features in several bioMEMS applications [26-28]. While SU-8 is easily photopatterned, it is highly autofluorescent and thus poorly suited for the high-contrast fluorescence imaging that is critical to many bioMEMS applications. In our work, we demonstrate the use of a commercially available photopatternable silicone, PPS, (WL-5150, Dow Corning Corporation) that combines several key advantages of both PDMS and SU-8. PPS obviates the need for custom synthesis and its inherent photopatternability helps address some limitations associated with soft-lithography-based methods. This material thereby presents new capabilities in the design and fabrication of biological microsystems.

PPS was originally developed for the electronics industry and has been used for several advanced packaging applications [29-31]. PPS chemistries are considered proprietary and the exact chemical compositions are not freely available. In general, the chemical composition of PPS is a silicone resin dissolved in a plasticizing matrix [32]. The ratio of solvent (typically mesitylene) added to this mixture facilitates spin-coating and control of the final film thickness. UV exposure followed by thermal curing results in a cross-linking reaction of the silicone constituents that produce a three-dimensional network structure. The light-activated catalyst provides chemical cross-linking that is more thermally stable than that obtained using traditional epoxy-based cure chemistries and further allows for minimal shrinkage during cure [32].

The unique properties of PPS that are outlined in this chapter make it an ideal candidate choice for the construction of single bioparticle traps. Previous single cell traps have leveraged dielectrophoresis-based mechanisms to either push or pull cells towards electrode structures (see Figure 2-1). Specifically, positive-dielectrophoresis (or pDEP) structures provide the capability to hold live cells in an arrayed manner, however, they require the use of non-physiological

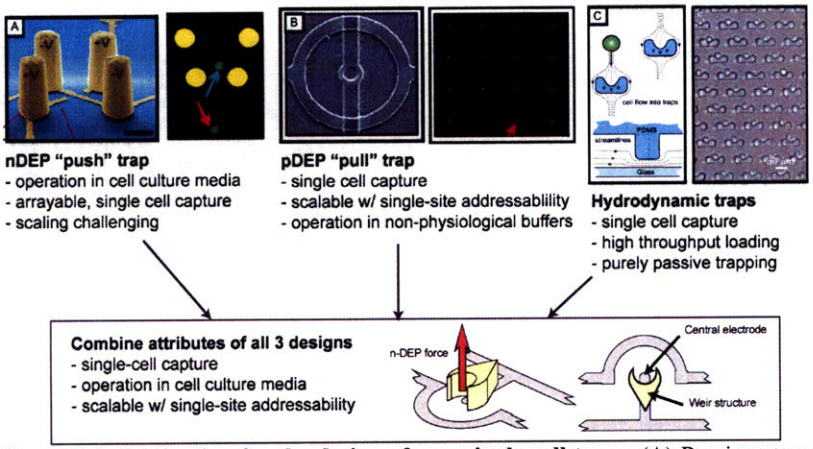

Figure 2-1: Motivation for the design of new single-cell traps. (A) Previous trap designs have incorporated negative dielectrophoresis (nDEP) based traps that push the cell in to an electric field minima. (B) Enhancements to (A) have been made by planarizing the structures to create a electric field maxima at the center of the "ring-dot" structure and generate a positive dielectrophoresis (pDEP). Such traps are designed to operate in non-physiological buffers. (C) Hydrodynamic cell traps enable efficient loading of large numbers of cells but cannot be individually addressed. This motivated the design for a new trap which combined the benefits all three architectures in the ability to capture single-cells, operate in cell culture media and provide single site addressability.

media for operation. As with negative dielectrophoresis (or nDEP) traps these traps are capable of both holding and then releasing single cells. Passive, hydrodynamic traps are readily fabricated using soft lithography and can be quickly loaded to hold a large population (~100) of single cells [33]. Such traps are readily used for monitoring single cells [34] but provide no mechanism for the release of target cells for downstream collection and analysis. The goal was to build a new single bioparticle-trap that could combine the advantageous features of all these three trap architectures (as shown in Figure 2-1).

It follows that these new types of traps require a material system that provides the following five attributes – (1) cell-scale resolution, to trap cells the features achievable must be at the very least on the size-scale of cells, (2) capability to build free-standing structures, (3) have demonstrated biocompatibility, (4) exhibit low autofluorescence to be compatible with cell imaging techniques, (5) capability to align structures to pre-patterned electrodes. The results presented in this chapter thoroughly characterize these five key properties of PPS, and show its application in the design of a canonical dielectrophoresis-based system. While other commonly used materials for bioMEMS such as PDMS and SU-8 can also provide some of these benefits (as discussed in the supplementary information section), they do not provide all these five functionalities. Hence, PPS clearly presents a new material system for bioMEMS that can encompass the advantageous features of both PDMS and SU-8 to realize new trap architectures.

2.2 RESULTS

2.2.1 Feature resolution

To date, in the bioMEMS community, SU-8 negative photoresists are the dominant materials for polymeric feature fabrication. In our work we have evaluated the recently developed PPS chemistry developed by Dow Corning and compared some of its key properties to those of SU-8. In Figure 2-2 we compare patterns created using SU-8 and PPS. One important parameter in a structural material is sidewall angle. While SU-8 offers re-entrant profiles of ~94° ± 2° (n = 12), PPS provides sidewall angles of ~76° ± 1° (n = 8) (Figure 2-2A, B). SU-8 is available in a variety of different solvent formulations that provide micron-scale pattern resolution across a range of tunable thicknesses. To assess the resolution of PPS in the context of SU-8 patterning capabilities, we used a standard resolution test target (USAF 1951) to photopattern features with both materials. As

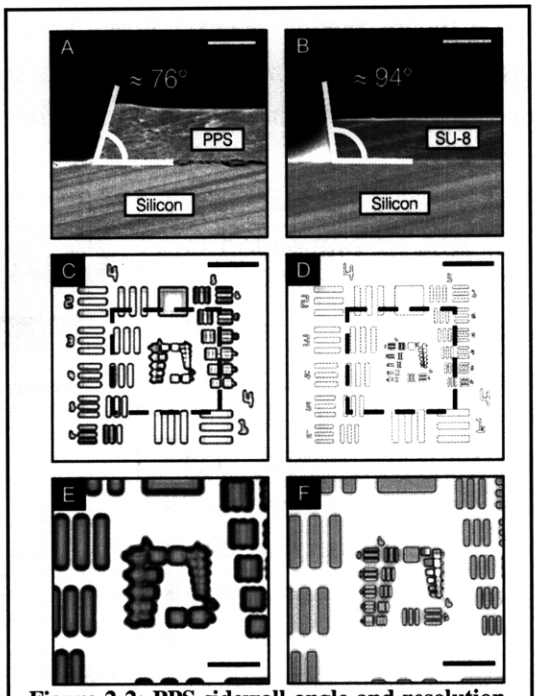

Figure 2-2: PPS sidewall angle and resolution. In (A & B) we show scanning electron micrographs of sidewall angles formed using PPS and SU-8. Scale bars = 25 μm. In (C) and (D) we provide bright-field microscopy images of the standard USAF 1951 resolution test pattern photopatterned in PPS and SU-8 respectively. Scale bars 50 μm. (E) and (F) examine the outlined regions in (C) and (D), respectively, in closer detail. Scale bars 25 μm.

expected from its tapered sidewall profile, the resolution of our nominal 20-μm-thick PPS test structures is reduced when compared to SU-8 structures of equivalent thickness. The ultimate resolution that we could repeatedly print was ~10 μm, as opposed to ~6 μm for SU-8.

One interesting and important feature of PPS is its robust adhesion to the substrate. In all cases, when we examined the smallest patterned PPS features, though they were ill-formed, they did remain firmly fastened to the substrate. In contrast, many small SU-8 features (line width ~5 μm) were missing entirely from the wafer, suggesting that they had suffered from poor adhesion. In subsequent probe tests PPS structures stretched away from the substrate and even ripped prior to separation from the underlying wafer (data not shown). This behavior comes in stark contrast to similar SU-8 features, which completely detached from the wafer when subjected to comparable probing forces.

2.2.2 Free-standing structures

Free-standing mechanically isolated microstructures are challenging to produce using soft lithographic fabrication techniques. Prior attempts to create such structures have employed various specialized techniques where thin structured membranes were formed by either sandwiching poured PDMS between photolithographic masters[35] or by carefully adjusting the pour height such that the tops of the masters protrude from the film[36]. In all of these implementations a thin residual layer of PDMS remained affixed to the end-fabricated substrate such that any patterned features were linked together by means of a common membrane backbone. To the best of our knowledge, physically isolated polymer microstructures patterned on a substrate have never been realized using molding techniques. In contrast, using PPS, it is possible to fabricate free-standing elastomeric microstructures (Figure 2-3). By patterning numerous types of cylindrical posts with square and circular top-down geometries we readily reproduced structures with aspect ratios of 3:1 (measured as height:width).

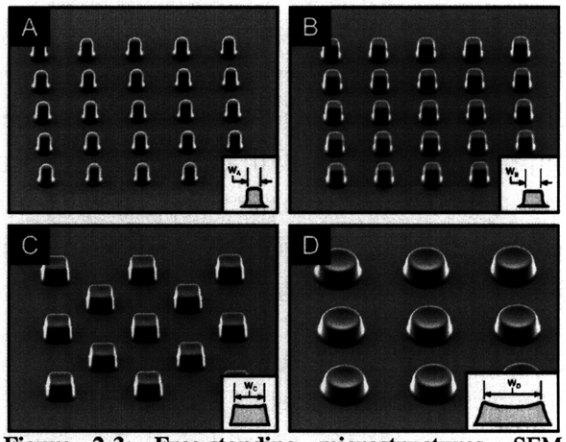

Figure 2-3: Free-standing microstructures. SEM images of free-standing circular, (A) and (D), and square, (B) and (C), pillars patterned on a silicon substrate. In each sub-portion of the figure we provide an inset schematic portraying the cross-sectional geometry of each feature (w_A □15 μm, w_B □20 μm, w_C □45 μm, and w_D □ 80 μm). Internal film stresses and feature edge geometries produce differing top surface profiles. Shapes with smaller footprints offer slightly convex tops while features with larger footprints exhibit concave geometries.

Features exhibiting higher aspect ratios (>5:1) proved challenging to fabricate reliably using our current processing techniques (see supplementary information section). This complication likely reflects a fundamental limitation of the currently available PPS elastomer chemistry. Even with process optimization, we were unable to bring PPS aspect ratios to the level of SU-8. When attempting to fabricate high-aspect-ratio features in PPS we commonly

witnessed deformed posts that bent over and adhered to the substrate. Though the mechanisms are not entirely clear, the observed failure mode suggests that the patterned designs' mechanical properties are insufficient for self-support.

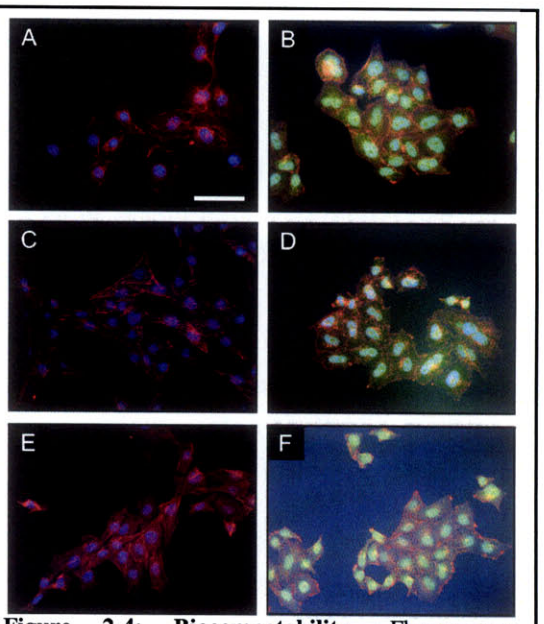

Figure 2-4: Biocompatability. Fluorescence microscopy images showing NIH3T3 (A) and HeLa (B) cells grown on PPS for four days. To compare, (C) and (D) respectively offer images of 3T3 and HeLa cells plated and grown on TCPS dishes over the same duration. As an additional comparison, (E) and (F) respectively offer images of 3T3 and HeLa cells plated and grown on PDMS-coated substrates over the same duration. The images in (A, C & E) represent merged actin (red) and DNA (blue) channel fluorescence while those in (B, D & F) additionally provide the constitutive EGFP expression (green) of the HeLa cell line. Scale bar 50 μm.

2.2.3 Biocompatability

For widespread adoption of PPS as a material choice in the bioMEMS community, it is imperative to characterize its biocompatibility. As a first step we cultured both NIH 3T3 and HeLa cells, two lines commonly used in bioMEMS applications, on PPS-coated substrates for a span of four days (Figure 2-4A & B). At the end of the four-day cultures we stained the cells' actin and nuclei using standard immunofluorescence techniques. Cells cultured on PPS surfaces (Figure 2-4A & B) as well as those grown on comparative bioMEMS control surfaces—silicon nitride, SU-8, PDMS (data not shown)—exhibited morphologies closely matching those typically seen in standard tissue-culture polystyrene (TCPS) dishes (Figure 2-4C & D). This preliminary result shows that PPS does not result in any noticeable changes in cell morphology and furthermore does not significantly alter growth and proliferation of cells over four days. Because PPS' chemistry closely matches that of PDMS[19], our results suggest that PPS may behave similarly to other biocompatible silicones.

2.2.4 Autofluorescence

Fluorescence-based assays are widely used in bioMEMS applications. Tracking, locating and interrogating cells in microdevices commonly involves the use of various types of fluorescence imaging. It is thus imperative that the materials used in devices are not so autofluorescent as to impair image-based assays. To address this issue we have characterized the autofluorescence of PPS in the context of cell-based bioMEMS. HeLa cells with red, green and blue fluorophores were imaged on TCPS and on silicon substrates coated with PPS, PDMS, SU-8, and silicon nitride (Figure 2-5A). The red, green and blue fluorescence channels are representative of those used in most cell-based imaging. Exposure times for all the channels were chosen so as to enable high-contrast imaging on most of the substrates. Under these conditions, some of the images recorded on the SU-8 surfaces saturated with background fluorescence. This saturation is caused by the higher autofluorescence of SU-8. To determine the intrinsic fluorescence of the

different substrate coatings, we measured the autofluorescence of blank substrates (without cells) in the red, green and blue fluorescence channels with the same exposure times used for cell imaging. Even though the exact same exposure times were used for obtaining images of different substrates with or without cells, it is not possible to make direct comparisons of the background fluorescence intensity in the images with cells (Figure 2-5A) to the quantitative measures of autofluorescence (Figure 2-5B). The images with cells (Figure 2-5A) provide a qualitative measure of the intrinsic fluorescence of the various substrates since the background fluorescence in these images could contain artifacts from cell staining procedures.

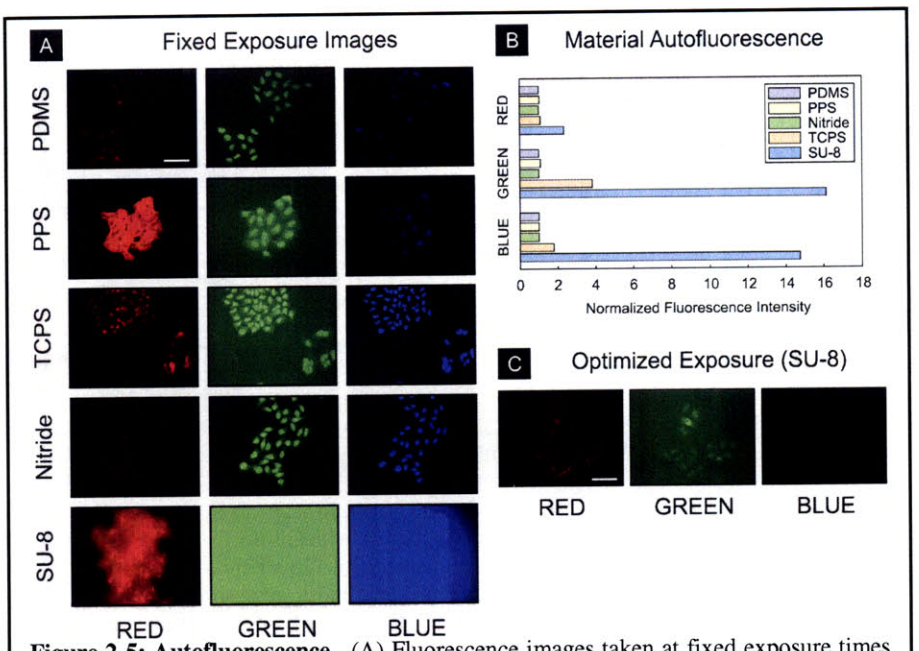

Figure 2-5: Autofluorescence. (A) Fluorescence images taken at fixed exposure times for red (750 ms), green (3000 ms) and blue (150 ms) channels of dual-stained EGFP+HeLa cells imaged on PDMS, PPS, silicon nitride, TCPS and SU-8. Scale bar = 50 μm. (B) Quantitative comparison of fluorescence intensities of PDMS, PPS, Nitride, TCPS and SU-8 (normalized to PDMS), indicating high auto-fluorescence of SU-8 in green and blue channels, explaining the saturated images in (A). Fluorescence imaging can be performed on SU-8 substrates by optimizing for exposure times. Representative images are shown in (C). Scale bar = 50 μm.

Fluorescence levels from PPS-coated substrates were similar to PDMS: ~1 % greater in blue, 10 % greater in green, and 4 % greater in red (Figure 2-5B). SU-8 coated substrates exhibited much higher autofluorescence than PPS (Figure 2-5B), especially at shorter wavelengths (~2.5× brighter in red and ~15× brighter in blue & green). These results explain the saturated images obtained on SU-8 in Figure 2-5A. While it is certainly possible to optimize SU-8 exposure conditions to image cellular fluorescence (Figure 2-5C), the autofluorescence of SU-8 (Figure 2-5B) fundamentally decreases the contrast between sample and background, limiting the ability to perform sensitive fluorescence-based assays[27].

2.2.5 Multi-level alignment fidelity

In contrast to standard master-molded PDMS, PPS enables wafer-scale feature alignment. Because it behaves as a standard negative photoresist, it is straightforward to position patterned PPS features onto underlying substrate registration marks with in-plane placement accuracies in the 2-3 μm range across 150-mm wafers (Figure 2-6, A-C). This large-area alignment extends well beyond the typical capabilities of molded PDMS. Specifically, the flexible nature of molded PDMS slabs makes it challenging to align them to other patterned geometries.

2.2.6 Functional device operation

Finally, we wanted to demonstrate that the ability to align PPS to underlying features (in this case, metal) allowed for the creation of functional bioMEMS devices. We first fabricated a simple bioMEMS device (Figure 2-6D) that consisted of patterned strips of PPS aligned over a bank of underlying interdigitated electrodes. We then pipetted DsRed-expressing BA/F3 cells onto the devices and stimulated the on-chip electrodes using a 5 Vpp signal delivered at 500 kHz. As shown in Figure 2-6E, prior to voltage application, cells are randomly distributed across the chip surface. Applying voltages, in turn, created negative dielectrophoretic (DEP) forces in regions of the device where uncovered electrodes were present. These DEP forces lifted stimulated cells vertically away from the interdigitated electrode edges. Subject to this stimulation, the cells organized into distinct levitating bands. Alternatively, the regions covered with PPS patterns left cells unaffected by DEP forces as the overlying PPS insulated the solution from on-chip electric fields (Figure 2-6F). The fact that DEP forces are created in the unmasked areas suggests that little or no PPS film remains in those regions; in highly conductive cell culture media, even nanometer-thick residual insulating films left on the device surface would be sufficient to eliminate the electric field in the solution (See Supporting Information).

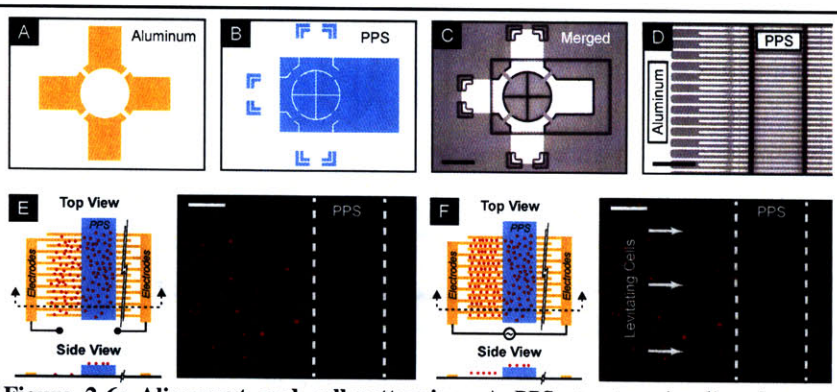

Figure 2-6: Alignment and cell-patterning. A PPS structure is aligned to an aluminum metal layer outlined schematically in (A) and (B). (C) presents a brightfield image of the resulting structure. Scale bar = 500 μm. (D) shows a brightfield image detailing the top-down view of a simple dielectrophoretic cell manipulation structure where a 20-μm-tall PPS strip is aligned to an interdigitated aluminum electrode array positioned within a surrounding flow chamber. Scale bar = 200 µm. (E) and (F) demonstrate the basic functionality of this device. Schematics show that when no voltage appears across the electrodes (orange), cells (red circles) initially settle randomly across the device surface (E). After electrode activation, cells respond to imposed negative DEP forces in select regions of the device causing overlying cells to levitate and organize into bands (F). Both (E) and (F) show fluorescent images from actual devices operating with DsRed+BA/F3 cells. In (E) cells that initially resided upon the patterned PPS strip (slightly out of focus due to their elevated height with respect to the substrate-affixed electrodes) are left in their original unorganized state. In (F) arrows highlight a few of the organized levitating cell bands. Scale bars 50 µm.

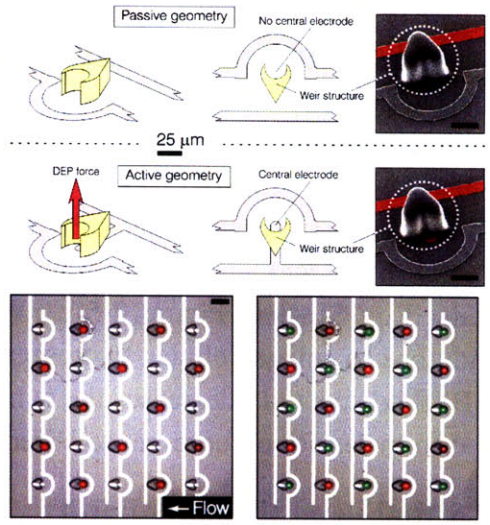

Figure 2-7: Single bio-particle traps. Top panel shows the SEMs of both active and passive traps realized with the integration of PPS. Bottom panel shows results obtained with loading differentially labeled beads in to such traps. Scale bar 25 µm. Adapted from Taff *et al.* [1].

2.2.7 Single bio-particle traps

Single bio-particle traps were successfully fabricated using PPS by leveraging its unique processing and alignment capabilities (as shown in Figure 2-7). Such traps were used to load and eject single polystyrene microspheres. The successive loading and ejection of three-different types of fluorescently labeled beads exemplifies the capabilities of this trap architecture and points to the stability of loaded particles (i.e. particles that are loaded and then not ejected remain in the trapped position and are not perturbed by incoming particle streams). More details of results obtained with these traps are presented in [1] and have not been included here as the large part of the experiments of trapping with single cells and beads were performed by Brian M. Taff.

2.2.8 Descum process for PPS

A descum process for PPS was implemented (as detailed in the Methods section) and used to further sharpen the features of the single bio-particle traps. As is evidenced in Figure 2-2, PPS structures exhibit sloping sidewalls. These sidewalls are likely due to the fact that the PPS films are processed using proximity and not contact lithography. The reactive ion etching process used for the descum removes any excess material that could be coating the electrodes ensuring the propagation of electric fields. Further, it is a "self-masking" process and therefore the original features act as a mask that protect the true structural features, whereas residual materials and excess materials on the sidewalls are effectively removed. As shown in Figure 2-8, both SEMs and optical micrographs indicate the removal of significant amounts of material. The results presented here are preliminary but with additional process optimization and the use of profilometry the exact sharpening effects of the descum process can be quantified.

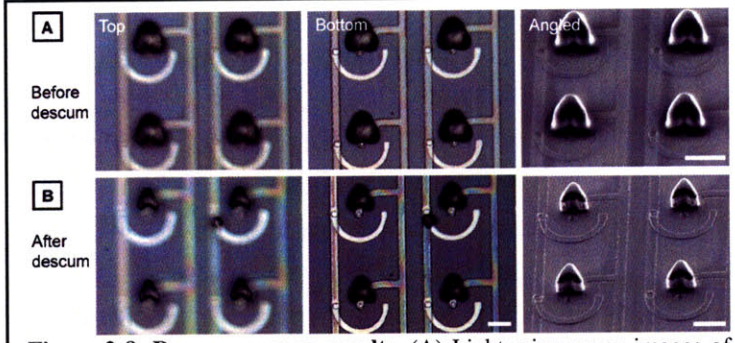

Figure 2-8: Descum process results. (A) Light microscopy images of top (left) and bottom (center) of trap structures, and angled SEM image (right) of structures as fabricated. (B) Corresponding images after descum processing. Top (left) image shows enhancement of trap geometry with clearly defined capture cup whereas bottom (center) shows removal of footprints that cover the electrode region. Angled SEM images also show improved structural features with increased electrode area. Scale bars 25 μm.

2.3 DISCUSSION

PPS was originally developed for the electronics packaging industry. To date, its major applications have included new approaches for flip-chip solder-bump designs [30, 31] and wafer-scale pressure sensor enclosures [29]. It is commercially available in numerous solvent formulations and photopatterning resolutions. We chose a chemistry suitable for creating the micron-scale geometries typically found in many bioMEMS devices. In our work, we have explored and leveraged PPS' properties integrating the material for the first time in devices

designed for use with mammalian cells. Examining its capabilities and its limitations in the context of the demands imposed by biological microsystems applications sheds new light on its overall functionality and usability.

A primary feature of PPS is its low autofluorescence. With a response in concert with that of PDMS, this material provides a significant advantage over SU-8 for biological imaging (Figure 2-5). In microsystems where one wishes to perform fluorescence imaging, PPS offers significantly enhanced contrast over SU-8. This low autofluorescence is somewhat surprising, since many photopatternable polymers (including SU-8) demand cationic activation of epoxy side chain groups and an associated crosslinking of shared aromatic hydrocarbon backbones [37]. Such aromatic constructs, with characteristically delocalized □-bond p-orbital overlap, permit a multitude of electron energy states which typically provide affiliated compounds with substantial, widely reported [38-43], native autofluorescence characteristics. Thus, PPS' low autofluorescence was welcome and fundamental to our enthusiasm for the material.

We found the resolution of PPS to be moderate, primarily limited its sidewall angle. SU-8, in contrast, patterns with much higher resolution (for equivalent thicknesses) due to its almost vertical re-entrant profile. The resolution of PDMS structures are determined by the master from which they are cast, and can vary from tens of microns to the sub-micron regime. Since many bioMEMS devices only require moderate resolution, PPS offers wide applicability, though for small structures or those with near-vertical re-entrant sidewalls, PDMS or SU-8 are better choices.

Though the resolution of PPS is lower than that of SU-8 and PDMS, its ability to form mechanically isolated low-autofluorescent structures distinguishes it from these two materials. Specifically, SU-8 enables isolated highly fluorescent structures, while PDMS suits applications requiring contiguous, low-autofluorescent structures. The enhanced flexibility provided by PPS-based low-autofluorescent isolated features directly addresses many of the limitations in prior microsystems with image-dependent applications spanning from actin cortex studies [44] to single-cell analyses [28] and manipulation [27], and even DNA microstructure analyses for advanced fluorescent *in situ* hybridization (FISH) assays [45].

One potential limitation of PPS is the current upper bound for fabricated structure thicknesses. SU-8 and PDMS both provide the flexibility to form features that are greater than one hundred microns in height using a single spun layer. In contrast, single layers of PPS currently enable feature heights of only ~40 μm and lower. This characteristic is likely not intrinsic to the material, but rather a limitation of the viscosities of available formulations. It may be possible to increase PPS layer thicknesses by varying the product formulation, though the likely continued presence of a 75° sidewall angle would ultimately limit the utility of thick (>100 μm) structures. While the 40 μm single-spin layer thickness limitation precludes the use of PPS for many

structural applications, we believe that it still enables remarkable design flexibility serving a wide variety of uses. The material opens avenues for assembling fluid chambers where micropatterned PPS gaskets separate rigid top and bottom planes. This enhancement enables designs where pressure driven flow will not deform cross-sectional chamber geometries in high-throughput applications. Because PPS readily plasma bonds to glass, it additionally avoids the additional process complexity needed for bonding of SU-8 gaskets to glass [46]. Thus, PPS, even in its current formulations, offers benefits for designing structures of moderate heights. In contrast SU-8 and PDMS are likely better choices for applications requiring precisely formed tall structures.

PPS is processed as a conventional photoresist and thereby benefits from the alignment capabilities of photolithography. This functionality is similar to SU-8, but a significant advantage over PDMS, which requires alignment of a flexible substrate after separation from its master. In addition, PPS adheres to underlying metals, unlike PDMS, and in our hands offers better adhesion to the substrate than SU-8. This flexibility offers a means to form multi-layer structures that combine metals, dielectrics, and low-autofluorescent structural layers. We demonstrate one such device in Figure 2-6. Essentially any microsytems-based design that utilizes on-chip electrodes presents a potential application space for this photopatterned polymer system. A wide variety of bioMEMS electroporation and electrofusion devices [47] are thus well positioned to benefit from the integration capabilities offered by PPS. In some electrokinetic flow devices [48], external power source demands could be reduced by positioning electrodes on-chip. Elaborate microscaffold architectures for 3-D cell perfusion [49], stand-alone flow-through chip designs [50], neuronal patterning structures [51], and even patch clamp applications [52] could benefit from enhanced fluorescence imaging capabilities through PPS-based structures. If low autofluorescence is not mandated, SU-8 may better suit multi-level applications, due to its maturity, resolution, and thickness range but PPS does present a compelling alternative for designs involving fluorescence assays.

One key application for SU-8 and PDMS is relief casting, where SU-8 serves as a mold for casting PDMS. While it may prove feasible to silanize PPS patterns and subsequently form relief-based architectures in PDMS, PPS is better suited for other applications. Though PPS' non-reentrant sidewalls could ease PDMS mold removal, the thicknesses and resolutions achievable in the template geometries would generally underperform equivalent designs formed using SU-8. The photopatternability of PPS provides benefits for alignment that confound the material's relevance to the context of relief molding. While rapid PDMS prototyping leverages repeated castings from a single master, PPS features cannot be recreated without returning to the cleanroom.

In this chapter we have taken preliminary steps to characterize the relevance of PPS as a biomaterial. Admittedly, the notion of biocompatibility is far too general a concept to examine

exhaustively [23, 53-57]. Proving that a given material presents no biological effects for all applications is impossible. Our initial examinations do however suggest that PPS holds promise as a biomaterial. In the context of polymer-based biological materials researchers have significantly more experience with both SU-8 and PDMS. PDMS, has seen routine use with cells for better than 20 years [58, 59]. SU-8 has also been used with cells, even primary cells [49, 60], although researchers often perform a solvent extraction step beforehand to aid biocompatibility [61]. The dearth of historical familiarity with PPS as a biomaterial thus presents a notable barrier to its widespread adoption.

In sum, the properties of PPS position it for a suite of applications not currently covered by SU-8 and PDMS. PPS will admittedly require further support and characterization before widespread adoption is likely. As an effort to fill this information void, we have presented here the key properties and functionalities associated with PPS in the context of the material's applicability to biological microsystems. Through continued research, PPS may become more commonplace in designs and offset a number of limitations associated with the current suite of materials for bioMEMS device fabrication.

2.4 CONCLUSIONS

We have examined some of the functional properties of a newly available commercial photopatternable silicone from the perspective of biological microsystems applications. PPS provides a unique combination of properties currently lacking in any one polymer commonly used for bioMEMS device architectures. It can readily form freestanding features on wafer-scale substrates and its low-autofluorescence provides a means to construct substrate-attached polymer structures suitable for high-contrast fluorescence-based imaging. Because the non-exposed regions in PPS patterns are largely residue-free, it ideally suits applications where substrate electrode geometries must remain uncovered. As its pattern formation leverages standard photoresist processing, aligning the material with pre-patterned features on a substrate is straightforward. Finally, the lack of any obvious morphological changes in cell cultures grown in direct contact with PPS holds promise for its incorporation in biological microsystems. With its unique set of properties, we believe PPS is poised to join SU-8 and PDMS as a widely used bioMEMS material.

2.5 MATERIALS & METHODS

Surface Preparation for Cell Culture. We cultured cells on the following surfaces: 1) SU-8 2015 (Microchem), 2) Sylgard 184 polydimethylsiloxane (PDMS) (Dow Corning), 3) PPS (Dow Corning), 4) silicon nitride, and 5) Nunclon Delta 35mm tissue culture polystyrene (TCPS) dishes (Nunc). For SU-8, PDMS, and PPS we coated each film onto an underlying 100-mm silicon wafer targeting nominal cured thicknesses of 20 μm (confirmed by DEKTAK profilometry readings – data not shown). To prepare wafers, we cleaned them in an oxygen

plasma for 7 minutes followed by a 10 minute dehydration bake at 250°C. When coating the SU-8, we followed standard processing recipes except in that we slowly ramped temperatures during bakes. We prepared the PDMS films using a 10:1 base-to-hardener mixture that we spun onto our wafers and then cured for 15 minutes at 100 °C. For the PPS coatings, we spread the film for 10 seconds at 500 rpm followed by 30 seconds at 2100 rpm. We then baked the films on a hotplate (2 min at 120 °C), flood-exposed at 10 mJ/cm^2 (i-Line) using a mask aligner, and postbaked (3 min at 150 °C on a hotplate). We developed the samples for 6 minutes in mesitylene (tri-methylbenzene, Sigma Aldrich, St. Louis, MO) and cured them at 150 °C for 2 hours. For our nitride surfaces we used Plasma Enhanced Chemical Vapor Deposition (PECVD) to deposit a 250-Å-thick nitride film on a 150-mm silicon wafer. After die saw separation, we cleaned the chips in ethanol. On the day prior to cell seeding, we soaked chips and the TCPS dishes in DI water for 12-16 hours. This procedure adhered to those previously described [61] which aimed to leach out any potential remnant solvents in the culture surfaces.

Plasmids. The DsRed T4 plasmid has been described previously[62], and was a gift from Susan Lindquist (Whitehead Institute, Cambridge, MA). Plasmids were amplified using chemically-competent E.coli strains (DH5α, Invitrogen). Plasmids were purified using a standard plasmid purification kit (Midiprep, Qiagen, Valencia, CA) from cultures grown in Luria broth overnight (standard E.coli culture protocols were used). Plasmid purity and concentration were subsequently assessed using a spectrophotometer (ND-1000, NanoDrop Technologies, Wilmington, DE).

Cell Culture and Transfection. NIH 3T3 fibroblasts were purchased from ATCC (Manassas, VA) and cultured as previously described [63]. EGFP+HeLa human carcinoma cells were a gift from Sangeeta Bhatia (MIT, Cambridge, MA). BA/F3 mouse pro B cells and WeHi-3B myelomonocytic leukemia cells were provided by Susan Lindquist (Whitehead Institute, Cambridge, MA). B cells were cultured in RPMI medium supplemented with 10% (vol/vol) fetal bovine serum (FBS), 10% (vol/vol) WeHi-3B conditioned medium as a source of murine IL-3, 2% (vol/vol) L-glutamine taken from 200 mM stock (Gibco), 100 units/mL penicillin (Gibco), and 100 μg/mL streptomycin (Gibco). WeHi-3B leukemia cells were cultured in Iscove's modified Dulbecco's medium (IMDM) supplemented with 10% FBS, 2 mM L-glutamine and 25 μM mercaptoethanol. WeHi-3B conditioned media was prepared as previously described[64]. BA/F3 cells were transfected using electroporation protocol I1 (Amaxa Nucleofection) and subsequently underwent antibiotic selection in 1 mg/ml G-418 (Geneticin, Invitrogen) supplemented media for 4 weeks. Stably transfected cells were then sorted for the brightest clones using flow cytometry (Mo-Flo, Center for Cancer Research Flow Cytometry Core, MIT).

Cell Growth and Staining for Fluorescence-based Imaging. Surface-coated chips and 35-mm TCPS dishes were first prepared as described above. Subsequently, all surfaces (surface-coated

chips and TCPS dishes) were plasma oxidized for 1 minute, soaked in 80% ethanol for ~10-minutes, and dried under nitrogen. We then aseptically transferred individual surface-coated chips to separate wells in a 6-well plate (n=2 for each chip type) and seeded all our surfaces with either NIH3T3 or HeLa cells using 2 mL of media/well at 1×10^4 cells/mL. We grew cultures for 4 days. On day 4 we fixed and permeabilized the cells and then stained for actin (rhodamine phalloidin R415 - Invitrogen, Eugene, OR) and DNA (Hoechst 33258, pentahydrate - Invitrogen, Eugene, OR) using standard protocols. All PBS washes used $MgCl_2$- and $CaCl_2$-supplemented PBS to minimize cell detachment. We used 1% BSA throughout to minimize nonspecific staining. We first stained actin and then DNA, and in preparation for imaging, we mounted coverslips using Flouromount G (Invitrogen) preservative.

Light microscopy. Silicon die with PPS and SU-8 resolution targets were imaged using an AxioImager microscope (Carl Zeiss MicroImaging, Thornwood, NY). Images were taken using 20× (0.5 NA) and 40× (0.75 NA) LD epiplan objectives (Carl Zeiss MicroImaging). All bright field images were captured at 8-bit resolution using a cooled camera (LA Vision). Fixed cells were imaged in epifluorescence mode. Fluorescence illumination was provided by an XCite 100 (EXFO Life Sciences and Industrial Division, Mississauga, Ontario) illumination source. EGFP (Set 38, Carl Zeiss MicroImaging), TRITC and DAPI filter sets (31000 and 31002, Chroma Technology, Rockingham, VT) were used for imaging constitutive EGFP expression, rhodamine phalloidin, and Hoechst nuclear stains respectively. Fluorescence images were acquired with 12-bit resolution. To assess background fluorescence, silicon die coated with PPS, SU-8, and PDMS were imaged using epifluorescence microscopy and a 20× (0.5 NA) objective. Care was taken to ensure that all images were recorded with identical acquisition parameters (exposure time, camera gain/gamma control and microscope aperture settings).

Descum processing. PPS-patterned die were placed on a blank wafer and loaded in to a reactive ion etch (RIE) chamber. The etch was performed on an Electron Cyclotron Resonance (ECR) based RIE system (Astex-Plasmaquest) using oxygen (O_2) and fluorine (SF_6) chemistries. Specifically, flows for O_2 and SF_6 were set at 100 sccm, the chamber pressure was set to 100 mTorr and the radio frequency (RF) power was set to 50 Watts. The DC bias power was set to 400 Watts. The process time was empirically optimized to be 25 minutes. The samples were carefully removed from the wafer chuck and subsequently imaged using light or electron microscopy techniques.

Scanning electron microscopy. Individual die were cleaned with acetone and isopropanol and subsequently dried with nitrogen. Die were then sputtered coated with ~50Å of gold in an argon plasma. Die were then mounted on standard flat mounts or angle mounts for imaging. Images were acquired at 5 kV acceleration and magnifications ranging from 250-400×.

Image processing. Images were post-processed using MATLAB. Autofluorescence of uniformly coated substrates was determined by taking the average intensity of the entire fluorescence image for each fluorescence channel. Sidewall angles were assessed by analyzing SEM images with AutoCAD (Autodesk) and are measured from within patterned features using the wafer surface as a reference.

Aligned Electrode and PPS Device Fabrication. We fabricated our aligned electrode PPS devices on silicon substrates. We first grew a 1.5-μm-thick silicon dioxide substrate isolation layer using wet thermal oxidation. We then sputter deposited a 5000-Å-thick aluminum layer onto the wafers and etched electrodes using BCl_3- and Cl_2-plasma-enhanced chemistries. We then deposited and patterned an aligned PPS layer (as described in the preceding subsection). Because PPS spun films are exceptionally tacky, even after prebake steps, we placed cellophane (0.001" thick) rings around the perimeter of each wafer prior to soft contact mode exposure on a mask aligner. This ring of cellophane prevents direct contact between the wafer and the mask, eliminating failures due to mask-wafer adhesion. We protected the wafer surfaces using standard positive photoresist and then separated chips with a die saw.

Chip Packaging. For our PPS-electrode devices, we packaged individual chips by mounting them on glass slides using double-sided tape. We then affixed the slides to a standard upright microscopy stage insert. We used laser-cut PDMS gaskets (250 μm thick, Bisco Silicones Inc.) around the active chip areas to form flow chambers. We then filled the chambers with cell suspensions and capped them with coverslips. We made electrical connections to the on-chip electrodes using alligator clips and delivered signals using an arbitrary waveform generator (Agilent 33250A).

2.6 ACKNOWLEDGEMENTS

We thank Alice Chen (from Sangeeta Bhatia's lab) and Sara Cullinan (from Susan Lindquist's lab) for providing us with cell lines, Luke Whitesell (from Susan Lindquist's lab) for help in plasmid preparation and Prakash Rao (from Harvey Lodish's lab) and Calvin Jan (from David Bartel's lab) for assistance with transfection. We thank Herman Meynen for helpful technical discussions regarding PPS processing, Scott Manalis and the Media Laboratory at MIT for laser cutter facilities access, and Nicky Watson of the WM Keck Foundation at the Whitehead Institute for SEM assistance. Michael Vahey provided valuable feedback pertinent to electrical modeling of residual on-chip PPS films. This work was supported in part by the NIH (RR199652, EB005753), the Singapore-MIT Alliance, and NSF Graduate Fellowship funding.

2.7 SUPPLEMENTARY INFORMATION

2.7.1 Spin curve data

Spin-curves for PPS have not been previously measured. To ensure the accurate fabrication of features spin-curves were measured by patterning features with distinct final spin speeds ranging from 500 rpm to 4000 rpm. The feature heights were measured using profilometry and were made at different points across a single wafer to provide an accurate representation of structural heights across a wafer. Four such measurements were averaged for each measurement point across a wafer and are plotted in the curve shown in Error! Reference source not found..

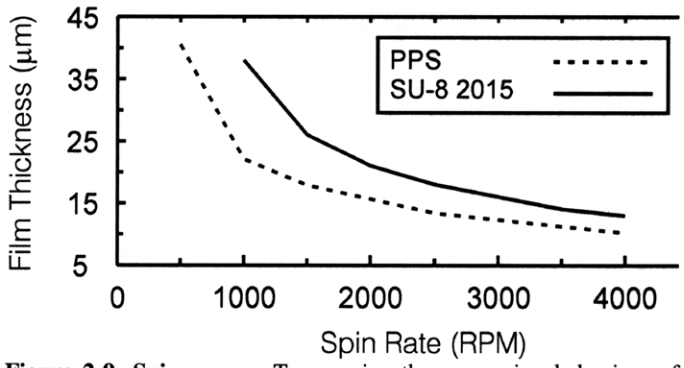

Figure 2-9: Spin curves. To examine the processing behaviors of PPS we provide a spin curve that directly compares its tunable thicknesses to those associated with standard SU-8 2015 formulations. Each point in the PPS curve is an average of four measurements taken at distinct points across a single wafer. The standard deviation across such measurements was less than 0.7 μm for each point.

2.7.2 Residual On-chip Thin Films

A key feature of PPS-based design is the ability to position aligned features directly onto prepatterned substrates. For devices dependent upon the effective propagation of electric fields into on-chip fluid environments, the residual film layers in non-UV-exposed portions of the substrate must be minimized or eliminated altogether. Here we examine this need for minimal residue using a model-based approach.

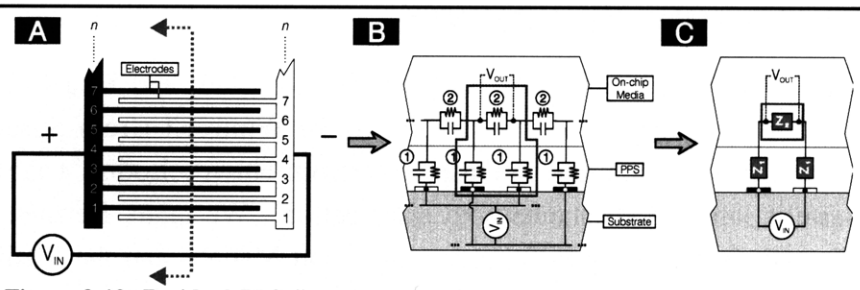

Figure 2-10: Residual PPS films. (A) Top-down schematic of the on-chip electrode designs used in our simple PPS-based bioMEMS device. By examining the cross section demarked in (A), **(B)** offers a linear system description of the various conductive paths linking nominally positive (black) and nominally negative (white) electrodes. The resistive and capacitive elements connected in parallel and labeled with 1's characterize the residual PPS films on the top surface of the device while the elements labeled with 2's describe electrical paths through the on-chip media. As boxed in (B), **(C)** examines the key "unit cell" necessary for understanding system behavior. Z's label the different on-chip impedances. Z_2, as highlighted in (C), becomes the focus of Figure 2-11.

For the simple interdigitated device architectures fabricated in our work, one can examine and model the system using a linear network of resistors and capacitors. In the case of our

geometries, we explored cell-based DEP effects on a bank of interdigitated electrodes where 169 nominally positive electrodes where interwoven with 169 nominally negative electrodes. Figure 2-10A provides a detail of this layout as well as its reduced linear system model (B). The model consists of parallel connections grouping resistances and capacitances associated with overlying residual PPS films (demarked with 1's in Figure 2-10B) that link series-wise to the parallelized resistances and capacitances associated with the on-chip fluid environment (demarked with 2's in Figure 2-10B). The system is characterized by repetitions of a single "unit cell" (outlined in Figure 2-10B) whose characteristic impedances are labeled in Figure 2-10C. Because of the largely independent electrical behavior of each subunit in the model, examining our 169 unit device as a system with infinite subunits provides a reasonable approach to obtain a function-based understanding of our design.

For effective operation, the device must enable a voltage drop within the on-chip fluid environment that largely tracks the potential difference delivered by the off-chip electrode activation source. Residual films that mask or attenuate in-fluid voltage drops reduce the electric field present in the device which in turn truncates on-chip DEP forcing capabilities. To examine the ratio of on-chip voltages to externally-imposed voltages we developed the transfer function outlined here.

$H = \frac{V_{OUT}}{V_{IN}}$, where V_{OUT} and V_{IN} are defined as labeled in Figure 2-10.

Figure 2-10C labels the characteristic impedances associated with the residual PPS films (Z_1) as well as the electrical paths traversing the on-chip media environment (Z_2). Each of these impedances lumps a single resistive element (R_x) connected in parallel with a single capacitive element (C_x). Their specific expressions are provided here.

$Z_1 = \frac{R_1}{1 + i\omega R_1 C_1}$ and $Z_2 = \frac{R_2}{1 + i\omega R_2 C_2}$, where the subscripts on the resistive and capacitive elements correspond with their associated impedance blocks.

Detailed even further, the individual resistance and capacitance values adhere to the following group of formulations.

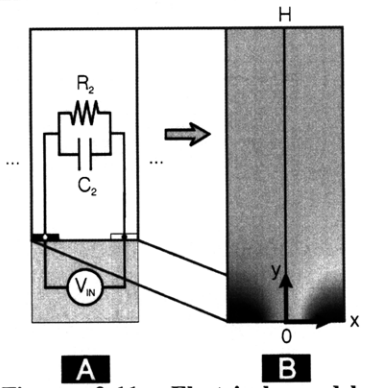

Figure 2-11: Electrical model. By examining the device when no PPS films blanket the top surface of the chip, we can tease out details related to the R_2 and C_2 parameters in the Z_2 impedance block (see Figure 2-10C). (A) details the relevant electrical model and (B) displays the associated simulated on-chip voltage profile. By integrating the current density along the centerline y-axis (from 0 to H) we obtain essential parameters necessary for evaluating the system transfer function.

$$R_1 = \frac{t_{PPS}}{\sigma_{PPS} w l} \qquad C_1 = \frac{\varepsilon_{PPS} \varepsilon_0 w l}{t_{PPS}}$$

$$R_2 = \frac{t_{MEDIA}}{\sigma_{MEDIA} h_{MEDIA} l} \qquad C_2 = \frac{\varepsilon_{MEDIA} \varepsilon_0 h_{MEDIA} l}{t_{MEDIA}}$$

In these expressions, t's describe PPS or effective media thickness values, σ's demark electrical conductivities, ε's provide electrical permittivities, w's represent on-chip electrode widths, l's describe electrode lengths, and h_{MEDIA} represents the effective height used to model the in-media cross-sectional areas of the electrically resistive and capacitive paths bridging oppositely polarized electrodes.

Using a voltage division analytical approach, we can easily expand the original transfer function representation to characterize both a single subunit within our electrical systems model as well as the overall infinite series of connected subunits. We explore this development here.

$$H = \frac{V_{OUT}}{V_{IN}} = \left[\frac{\left(\frac{R_2}{1 + i\omega R_2 C_2} \right) \frac{1}{n}}{\left(\frac{2R_1}{1 + i\omega R_1 C_1} \right) \frac{1}{n} + \left(\frac{R_2}{1 + i\omega R_2 C_2} \right) \frac{1}{n}} \right]$$

$$= \frac{1}{\frac{2R_1}{R_2} \left(\frac{1 + i\omega R_2 C_2}{1 + i\omega R_1 C_1} \right) + 1}$$

where n denotes the number of "unit cells" in the device. From this reduction, three key relationships appear: $\frac{R_1}{R_2}$, $R_2 C_2$, and $R_1 C_1$. Using prior expressions we can explicitly represent the last two relationships as:

$$R_2 C_2 = \frac{\varepsilon_{MEDIA} \varepsilon_0}{\sigma_{MEDIA}} \qquad R_1 C_1 = \frac{\varepsilon_{PPS} \varepsilon_0}{\sigma_{PPS}}$$

In these formulas all values are known enabling direct evaluation. In contrast, when expressing $\frac{R_1}{R_2}$ as: $\frac{R_1}{R_2} = \frac{\sigma_{MEDIA}}{\sigma_{PPS}} \left[\frac{t_{PPS} h_{MEDIA}}{w t_{MEDIA}} \right]$

the specific values for h_{MEDIA} and t_{MEDIA} are not known. To address this shortfall, one can determine instead a value for the ratio $\frac{h_{MEDIA}}{t_{MEDIA}}$ by examining the resistive and capacitive paths present in the system when no PPS residues exist. This scenario (diagramed in Figure 2-11) provides a description of the impact levied on the system by the fluid paths alone.

Using a generalized quasistatic simulation of our 2D non-PPS-coated system "unit cell" where the standard electrode widths, w, are reduced to $\frac{w}{2}$, the applied potential across paired electrodes is set to 1 V and the on-chip media conductivity is pinned to 1 S/m, we solve the Laplace equation and determine the associated voltage profile. We plot this COMSOL-simulated voltage response in Figure 2-11B. We then compute a boundary integral on the centerline that separates the two electrodes and evaluate the associated current density. The COMSOL simulation renders the following equality:

$\int_0^H J_x(y)dy = 0.500954$ [A/m], where $J_x(y)$ represents the x-directed (see Figure 2-11B) current density along the subunit centerline.

Using our prior representation of R_2 in combination with Ohm's law and the COMSOL integration value, we produce the following relation:

$$R_2 l = \frac{t_{MEDIA}}{\sigma_{MEDIA} h_{MEDIA} l} l = \frac{1 \text{ [V]}}{0.500954 \text{ [A/m]}}$$

$$\Rightarrow \frac{h_{MEDIA}}{t_{MEDIA}} = 0.500954 \text{ [S/m]}$$

With this $\frac{h_{MEDIA}}{t_{MEDIA}}$ ratio in hand we can evaluate the remaining $\frac{R_1}{R_2}$ relationship as described earlier and then directly compute the transfer function, $H = \frac{V_{OUT}}{V_{IN}}$.

Figure 2-12 provides two sets of magnitude and phase plots examining the transfer function response for media conductivities of 1.5 S/m (typical of many cell culture medias) and 0.01 S/m (typical of p-DEP device operation). In both cases, we survey a collection of varying PPS residual film thicknesses. Ideally, in the typical DEP frequency operation band (100 kHz - 100 MHz) one would hope for a magnitude response of 1 and, though less significant, a phase response of 0°. In the case of the 1.5 S/m on-chip solution even 10 nanometers of a residual PPS layer would begin to undesirably mask on-chip voltages. For the 0.01 S/m solution, residual films impact system operation in less notable ways, though again peak performance would aim for minimal on-chip PPS in untargeted regions. The fact that our simple interdigitated electrode-

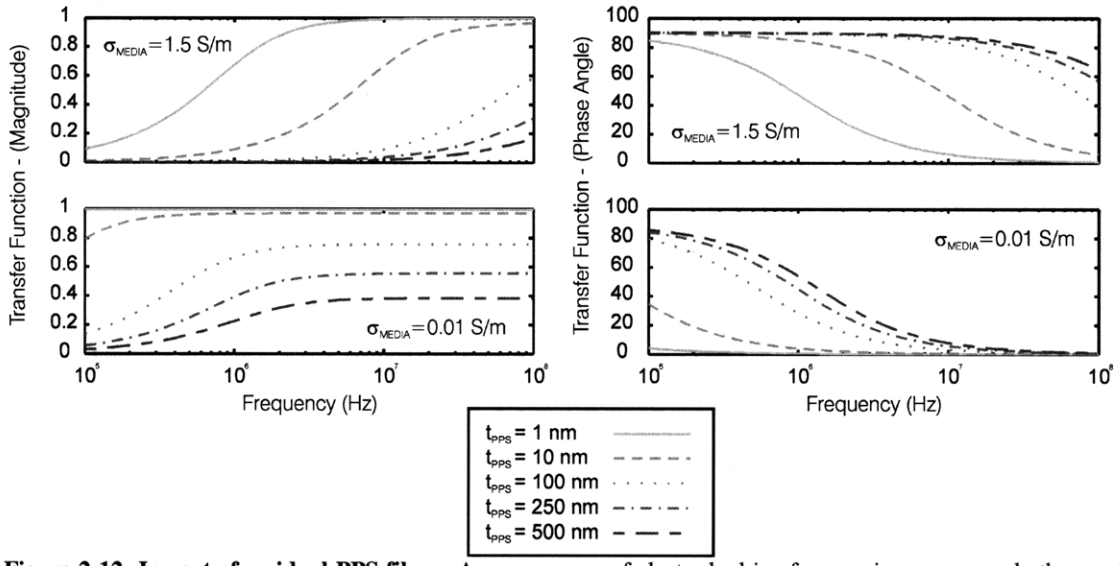

Figure 2-12: Impact of residual PPS films. Across a range of electrode drive frequencies we survey both magnitude and phase angle behaviors. Higher on-chip media conductivity frustrates the ability to exert DEP forces by reducing the potential drop produced in the system flow chamber. Increasing residual film thicknesses, similarly impact the system response in notable and potentially detrimental ways.

based chip designs function with cell culture media reinforces the notion that remaining PPS films are minimal for our processing conditions.

2.7.3 Additional Processing Details

Surface Preparation for Cell Culture. For the sample chips used in our fluorescence assays all processing bakes were performed using exhaust-connected leveled hotplates run in an open ambient cleanroom environment. When coating samples with SU-8 special care was taken to initially douse the entire front surfaces of the wafers with the raw polymer before executing a 10 second spread at 500 rpm followed by a 30 second spin at 3000 rpm. For our SU-8 samples, our 6 minute ramped prebake routine was comprised of: (1) a minute-long soak at 65 °C, (2) a three minute ramp to 90 °C, and (3) a two minute soak at 90 °C. Our exposures used a 10 mJ/cm^2 (i-Line) flood, followed by an 8 minute post bake routine. The postbake repeated the process used for the prebake byt extended the 90 °C soak from two minutes to three. We removed residual solvents using a 6 minute PM acetate-based development and ran a final 135 °C hotplate cure

bake. All samples prepared for fluorescence assays were front-side protected using a masking layer of diesaw tape prior to chip separation.

Cell Growth and Staining for Fluorescence-based Imaging. In our staining protocols we ran our extractions using 0.1% (v/v) Triton X-100 solutions in PBS. We additionally used Invitrogen's recommended 1 unit per coverslip concentration for the phalloidin staining (20 minute staining time) and set our Hoechst 33258 pentahydrate (bis-benzimide) concentrations to 1:100 dilutions in PBS (original stock solution concentrations were 10 mg/mL concentrations). The staining time was set for 15 minutes). Throughout the staining we took care to protect samples from excessive light exposure by housing them in laboratory drawers.

Aligned Electrode and PPS Device Fabrication. To avoid damaging patterned PPS features we coated the device wafers with standard positive photoresist prior to die separation. Because of the hydrophobic behavior of PPS in its "just developed" state we promoted photoresist adhesion using a 1.5 minute oxygen plasma ash followed by a brief HMDS exposure.

2.7.4 BioMEMS materials choices

As is presented in this chapter, the design of new types of traps requires a material system that provides the following five attributes – (1) cell-scale resolution, to trap cells the features achievable must be at the very least on the size-scale of cells, (2) capability to build free-standing structures, (3) have demonstrated biocompatibility, (4) exhibit low autofluorescence to be compatible with cell imaging techniques, (5) capability to align structures to pre-patterned electrodes. As is seen in Figure 2-13, PDMS and SU-8 only encompass a set of these properties. PDMS can be molded with cell-scale resolution, has well-characterized biocompatibility and low autofluorescence but it is exceedingly difficult to make isolated free-standing microstructures using soft-lithography based fabrication techniques. This is primarily due to the fact that structures fabricated using relief-casting would have to be connected with a contiguous sheet of material. Even the connecting sheet could be made thin enough it

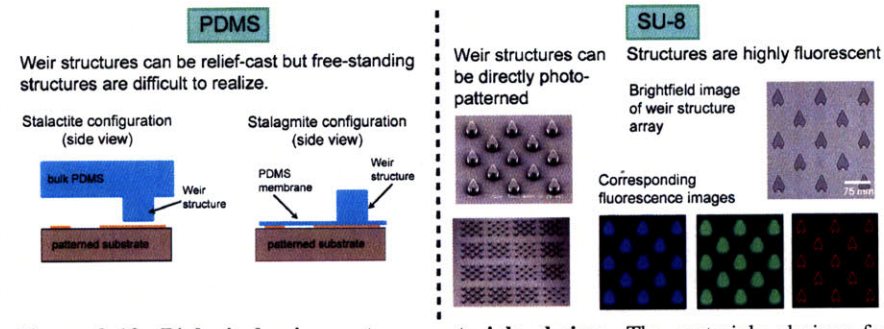

Figure 2-13: Biological microsystems materials choices. The materials choices for biological microsystems have typically involved PDMS and SU-8. PDMS (left panel) provides, low autofluorescence and appropriate feature resolution but the alignment of such weir structures to a patterned would prove to be extremely challenging. SU-8 (right panel) over comes the limitation of PDMS in the ability to pattern weir structures directly on the substrate but suffers from high-autofluorescence in the fluorescence channels typically used for biological imaging. Fluorescence images of SU-8 weir structures distinctly display this autofluorescence (and it has been quantified in Figure). These limitations point to the need for the application of a new material system for which PPS is an ideal candidate.

would be extremely difficult to align to a pre-patterned substrate. SU-8 overcomes this limitation of PDMS and can be directly photopatterned and aligned to electrodes, however it suffers from high autofluorescence, making imaging of cells a challenging task. Hence PPS combines the advantages of both PDMS and SU-8 as a power new material choice for bioMEMS.

2.7.5 Free-standing microstructures

As has been seen in this chapter, robust free-standing structures can be fabricated, however, there are limitations on the aspect ratio of structures achievable (as seen in Figure 2-14). As is seen in the SEM images, aspect ratios of 1:1 and 3:1 can be reliably realized. Aspect-ratios higher than 5:1 are extremely challenging to fabricate and result in the collapse and sticking of structures to the substrate. This is likely due to the fact that a wet development process is used for developing the exposed structures. It is possible that optimizations of the development process could result in the realization of such structures, but generating a consistent yield with such structures. Another important note about the processing involves the use of a short oxygen plasma clean (90 seconds) for switching making the PPS patterned surface more hydrophilic and easier to coat with photoresist. The photoresist coat is important for the protection of the wafer during the process of die-sawing in to individual chips. As is evidenced in the images in (A) and (B) of Figure 2-14, the PPS features are cracked and show defects (due to the long, 5 minute oxygen plasma clean). SEMs of the single particle trap structures as seen in Figure 2-8 do not exhibit such defects as they have been processed with the optimized plasma exposure time.

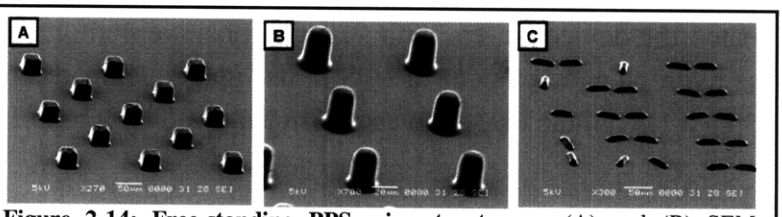

Figure 2-14: Free-standing PPS microstructures. (A) and (B) SEM images of comparatively low aspect ratio structures (< 3:1). (C) SEM image of high-aspect ratio structures (~5:1) that show mechanical collapse and adhesion to the substrate. Such comparatively high-aspect ratio structures are challenging to fabricate with PPS.

Chapter 3 – **Vesicle-based metrology tools**

In this chapter I will describe the development and application of a new metrology tool for biological microsystems. Specifically this tool consists of giant lipid vesicles with customizable electrical properties for the characterization of dielectrophoresis-based microsystems. Dielectrophoresis (DEP) has emerged as an important tool for the manipulation of bioparticles ranging from the submicron to the tens of microns in size. Here we show the use of phospholipid vesicle electroformation techniques to develop a new class of metrology tools with specifically engineered electrical properties to enable identifiable dielectrophoretic responses in microfabricated systems. These electrically addressable vesicles (EAVs) enable the creation of electrically distinct populations of test particles for DEP. EAVs offer control of both their inner aqueous core and outer membrane properties; by encapsulating solutions of different electrolyte strength inside the vesicle and by incorporating functionalized phospholipids containing PEG brushes attached to their hydrophilic head group in the vesicle membrane, we demonstrate control of the vesicles' electrical polarizabilities. This combined with the ability to encode information about the properties of the vesicle in its fluorescence signature, form the first steps toward the development of EAV populations as metrology tools for any DEP-based microsystem.

The results presented in this chapter have been previously published in *Langmuir* [65]. Additional information and techniques are presented in this paper along with a strategy for patterning lipids with the ultimate goal of forming monodisperse vesicle suspension. It is important to note that this work was performed in collaboration with Michael D. Vahey.

3.1 INTRODUCTION

Giant unilamellar vesicles (GUVs) have garnered considerable interest as model cells and model membranes. GUVs have been used as model systems for studying a range of cellular phenomena and machinery ranging from cellular compartmentalization [66, 67], actin polymerization [68], gene expression [69] and membrane fusion [70]. GUVs serve as good model systems due to their large size (1 – 100 μm) and ease of visualization with conventional light microscopy. They also offer exquisite control over both their inner aqueous core and outer membrane properties. Various techniques have been explored for encapsulating particles and molecules ranging from mammalian cells [71] to large DNA strands [72] within the aqueous core of vesicles. Additionally, standard formation techniques for GUVs allow for the creation of complex mixtures of lipids and small molecules within the membrane [73, 74]. We have leveraged this inherent flexibility in the preparation of GUVs to generate vesicles with distinct electrical properties which have identifiable dielectrophoretic responses. By modulating these electrical properties we have demonstrated the concept of electrically distinct vesicle populations to serve

as test particles for dielectrophoresis (DEP) based microsystems. We term these new test particles as electrically addressable vesicles (EAVs).

Although much recent work on GUVs has focused on the dynamics and structure of the vesicles themselves, the potential of these particles for metrology has been largely unexplored. The ability to control the composition of the aqueous core and membrane, in addition to enabling the study of membrane biophysics, also allows for the creation of vesicles spanning a wide range of electrical and mechanical properties. Accordingly, any system intended to manipulate cells or particles on the basis of their electromechanical properties can be characterized more thoroughly by using test particles specifically designed to encompass the entire range of these properties. DEP-based microsystems are widely used for patterning [75-77], concentrating [78-80] or sorting [4, 81, 82] cells. Dielectrophoresis the force on a polarizable object in a spatially nonuniform electric field depends on the electrical properties of the particle relative to the surrounding medium, and thus requires particles with known electrical properties for full characterization.

Current test particles for DEP consist primarily of polystyrene microspheres which are commercially available in several sizes and with various surface functionalizations (for example, carboxyl groups). While functionalized microspheres (FMs) can be further engineered with phospholipids in an effort to mimic biological membranes [83] they serve as poor models for live cells. This is largely attributable to the disparity between the bulk conductivity and permittivity of polystyrene and that of a cell's cytoplasm; polystyrene lends the particles a negative polarizability at high frequencies (~1 MHz) in nearly any aqueous solution. Furthermore, because the electrical properties of FMs are controlled primarily through the charge density presented at the surface of the particle, tailoring beads to exhibit a specific conductivity is generally not straightforward and may require potentially laborious sequences of reactions to achieve the desired electrical response. To circumvent some of these difficulties, it is possible to take the notion of surface modification to its extreme by coating otherwise electrically insulating particles with a conductive metal layer. These metal-coated particles then present an alternative to the low conductivity and permittivity of polystyrene relative to water. Although such particles have been successfully employed in testing systems where positive dielectrophoresis (pDEP) is essential, they are not as widely used as FMs. This may be

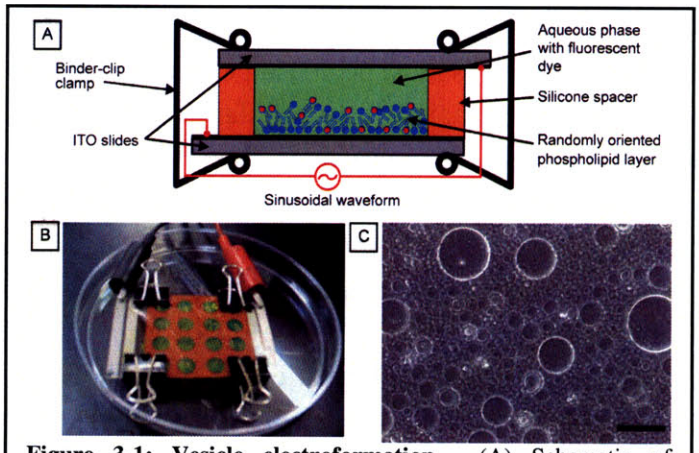

Figure 3-1: Vesicle electroformation. (A) Schematic of electroformation chamber used to create vesicles. (B) Photograph of electroformation chamber setup and (C) representative phase microscopy image of electroformed vesicles. Scale bar 50 μm.

attributable to the fact that they exhibit nearly uniform positive polarizability regardless of the frequency of the applied field or the conductivity of the surrounding medium. For many applications, a particle whose dielectrophoretic response is sensitive to its environment - both electric field frequency and medium electrical properties – is desirable. EAVs offer an alternative in which both the bulk properties of the particle (i.e. the aqueous core) as well as its membrane may be tailored to exhibit a particular DEP spectrum. GUVs enable the generation of test particles over a large range of conductivities (varying over ~100× of physiologically relevant conductivities) which cannot be achieved easily with commercially available FMs. The additional ability to label EAVs with membrane-bound or internalized aqueous fluorescent markers allows information regarding the vesicle's properties to be encoded so that vesicles can be visually identified. Taken together, the degrees of freedom afforded by EAVs with respect to their electrical polarizability and fluorescent signatures make these particles compelling model systems for DEP metrology.

3.2 RESULTS:

3.2.1 Creating EAVs

We have generated EAVs with customizable electrical properties through the process of electroformation [84]. A custom electroformation chamber was constructed from indium tin

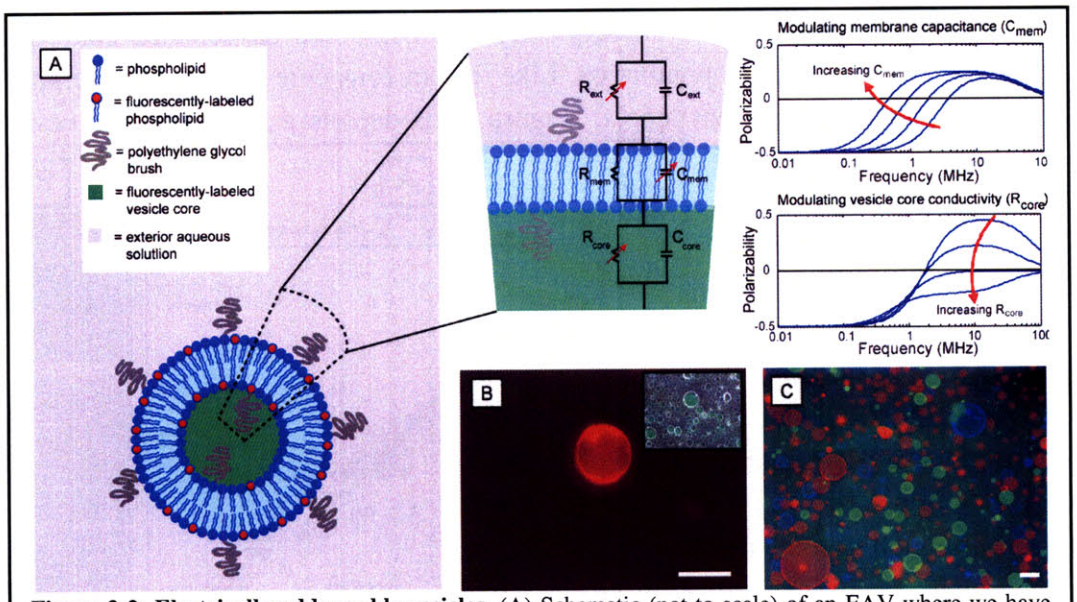

Figure 3-2: Electrically addressable vesicles. (A) Schematic (not to scale) of an EAV where we have independent control over the properties of the vesicle membrane and aqueous core. Control of vesicle membrane and aqueous membrane properties result in distinct electrical polarizabilities and consequently identifiable dielectrophoretic responses. Modulating the membrane capacitance with PEG brushes (schematic, center panel) results in shifting of the DEP spectra towards lower frequencies (plot, upper panel). Modulating the aqueous core conductivity by altering the ionic strength of the encapsulated solution results in lowering the peak polarizability of the respective DEP spectra (plot, low panel). (B) Demonstration of control of membrane and aqueous core properties. Fluorescence microscopy image of a representative EAV with lissamine-rhodamine-labeled membrane. The inset shows merged phase and fluorescence microscopy images with encapsulation of fluorescein salt (green) in the aqueous core of EAVs. (C) Merged fluorescence image of a population of differentially labeled EAVs - lissamine-rhodamine (red), carboxyfluorescein (green) and dansyl PE (blue). Scale bars 50 μm.

oxide (ITO) coated slides with a silicone spacer, as is depicted in Figure 3-1. Figure 3-2 shows a schematic of EAVs in which the composition of both the aqueous core and phospholipid membrane may be tuned independently (or in concert) to confer distinct electrical properties to a vesicle population. The electrical properties of the aqueous core are readily tuned in the electroformation process, by controlling the conductivity of the electroformation buffer and thereby conferring a specific internal conductivity, σ_c, to the formed vesicles. Therefore, by leveraging the electroformation process, it is straightforward to vary the value of σ_c over a broad range. Specifically, we have successfully formed vesicles in solutions ranging in conductivity from ~10^{-4} S/m (deionized water) to ~1.5 S/m (phosphate buffered saline), though we have observed that the size and yield of electroformed vesicles diminishes at conductivities above ~0.1 S/m. Such large variations in conductivity of test particles are challenging to generate with the polystyrene beads most commonly used for DEP metrology. Without significantly altering the conductivity or size distribution, we have also encapsulated fluorescent dyes, including fluorescein (Figure 3-2B, inset) and rhodamine. The encapsulation of fluorescent dyes facilitates the tagging of vesicles of specific conductivity with an identifiable fluorescence spectrum.

An additional degree of freedom in creating vesicles with distinct dielectric spectra is conferred by the phospholipid membrane. Long chain polymers (such as PEG) can be conjugated to the membrane bilayer to change its dielectric properties. PEG brushes serve to modulate the effective membrane thickness and consequently the membrane capacitance conferring unique electrical properties to a vesicle population. Like the aqueous core, the vesicle membrane is also capable of supporting fluorescent labels. Figure 3-2B depicts a representative vesicle formed with a fluorescently-labeled phospholipid, and Figure 3-2C shows a merged fluorescence image of sample EAV populations and indicates the ability to optically distinguish between differentially labeled EAVs. The ability to label vesicles not only allows us to encode information about the properties of the EAVs in their fluorescence signature, but facilitates the tracking and visualization of EAVs in microsystems.

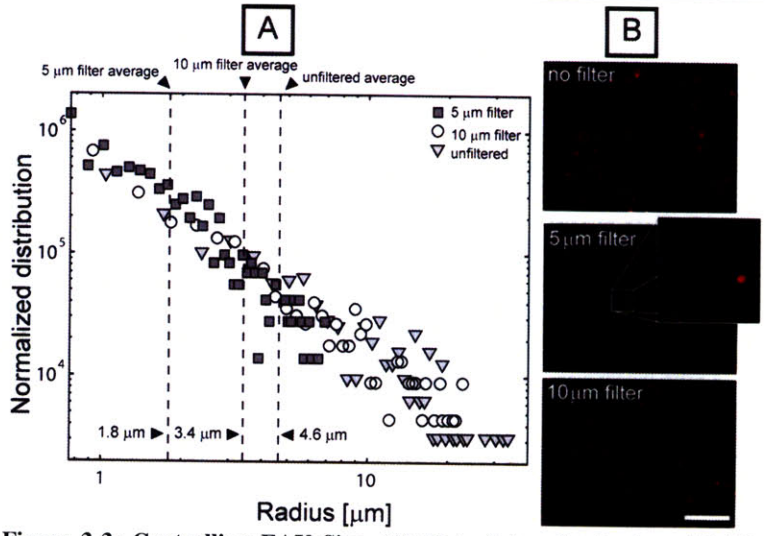

Figure 3-3: Controlling EAV Size. (A) Plot of size distribution of EAVs after filtration through different pore sizes (dark gray squares: 5 μm, white circles: 10 μm, light gray triangles: unfiltered). Dashed lines and accompanying numbers indicate the mean vesicle size for each of the three cases – 1.8 μm for a 5 μm filter, 3.4 μm for a 10 μm filter and 4.6 μm for unfiltered. (B) Fluorescence microscopy images before (top) and after filtering through 5 μm (middle) and 10 μm (bottom) filters showing that EAVs can be selected based on size.

3.2.2 Controlling EAV size

As is evident from Figure 3-2B, electroformation techniques

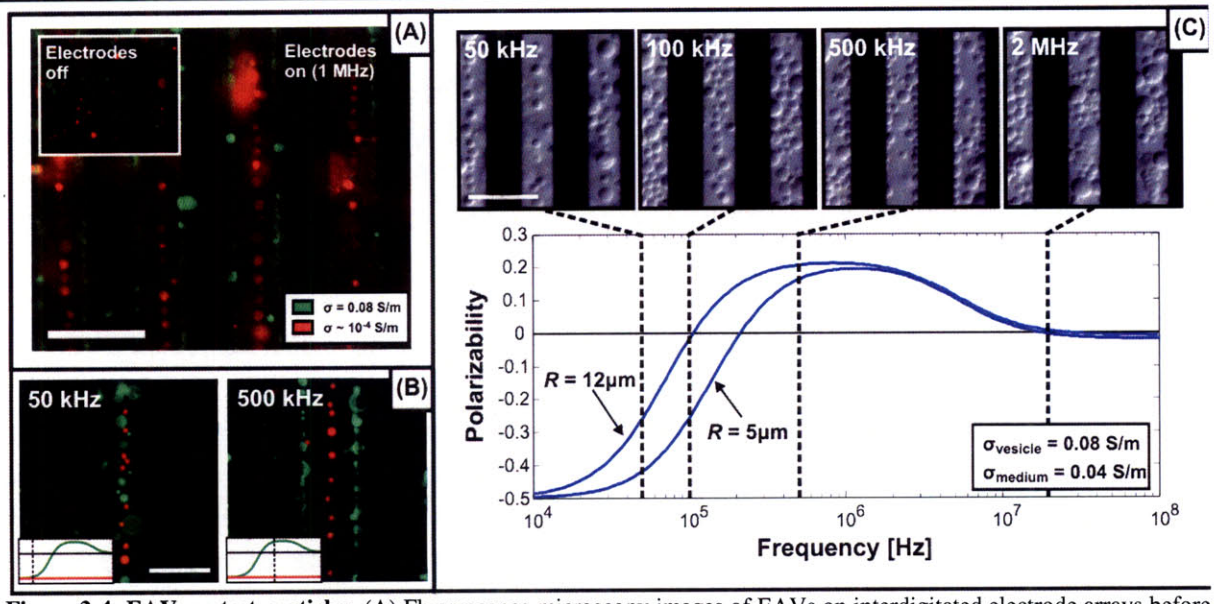

Figure 3-4: EAVs as test particles. (A) Fluorescence microscopy images of EAVs on interdigitated electrode arrays before (inset) and after applying a 1 MHz electric field, showing the different DEP responses of the red and green EAVs. Scale bar 50 μm. (B) Comparison of the dielectrophoretic response of EAVs (green) and polystyrene beads (red). While the beads exhibit a uniform n-DEP response across several orders of magnitude in frequency, the EAVs transition from negative to positive polarizability. Scale bar 25 μm. (C) The DEP spectra of EAVs with an interior conductivity twice that of the surrounding medium. Curves for EAVs with radii of 5 and 12 μm are obtained by fitting crossover frequency measurements to the single shell model of Eq. 1. EAVs of different sizes exhibit different membrane capacitances, resulting in the differences in spectra seen between ~10kHz and 1 MHz. The micrographs above the curves highlight the behavior of an EAV suspension at the indicated frequencies. As the frequency is increased, the EAVs' polarizabilities range from strongly negative (at 50 kHz, indicated in the figure by the exclusion of EAVs from the electrode edges), to weakly negative (100 kHz), to strongly positive (500 kHz, indicated by the accumulation of EAVs at the electrode edge), to nearly zero (at 2 MHz). Scale bar 50 μm.

yield EAVs with a wide range of sizes. To narrow the size distribution of EAVs and tailor them to the DEP system being characterized, we performed filtrations using syringe-attached inline glass frit filters (of 5 μm and 10 μm pore sizes). Figure 3-3A shows quantitative results for sizes of EAVs filtered through 5 and 10 μm pores (where sizes were measured using microscopy). Filtration through a 5 μm pore allows for tuning the mean EAV size from 4.6 μm to 1.8 μm whereas filtration through a 10 μm pores tunes the EAV size from 4.6 μm to 3.4 μm. The fluorescence images in Figure 3-3B show qualitative agreement with these results. The top panel shows unfiltered EAVs (labeled with lissamine rhodamine for fluorescence visualization) and the middle panel shows a fluorescence image after filtration through a 5 μm pore where few large (>10 μm) vesicles are visible indicating that they were blocked or ruptured in the glass frit filter. The bottom panel shows a representative fluorescence image after filtration through a 10 μm pore where several large vesicles are still visible. These results indicate that filtration serves as a reliable technique for being able to tune EAV sizes.

3.2.3 EAVs as test particles

The structure of electroformed GUVs, comprised of an internal aqueous core surrounded by a lipid bilayer membrane, lends these particles a dielectric spectrum which is qualitatively (and potentially quantitatively) similar to that of live cells. This spectrum is characterized by both

high- and low- frequency dispersions, and in the case of EAVs, may be controlled through the conductivity of the aqueous core, □c. By varying □c, it is possible to create test particles with specifically engineered spectra; this is in contrast to many widely available alternative test particles, including both metallic and polystyrene beads, which tend to have uniformly negative and positive dielectrophoretic spectra, respectively. Accordingly, it is possible to create EAVs for which the transition from negative to positive polarizability occurs at a controlled frequency (Figure 3-4A).

In addition to offering spectra distinct from commercially available microspheres, EAVs offer the ability to create suspensions of particles that are both visually and electrically distinct by varying the membrane-bound fluorophore and the conductivity of the internal solution. Figure 3-4A shows an experiment in which EAVs labeled with rhodamine (red) and carboxyfluorescein (green) and encapsulating different conductivities (0.1 and 80 mS/m, respectively, with a medium conductivity of 40 mS/m) respond differently to the application of an electric field at a frequency of 1 MHz. In this part of the spectrum, vesicles with internal conductivities in excess of the medium conductivity (□c > □m) exhibit positive polarizability and are attracted to the electrode edge, whereas vesicles with less conductive cores are negatively polarizable and are repelled to the regions above and between the electrodes. Figure 3-4B presents a related demonstration, where we used red fluorescent polystyrene microspheres to demonstrate the more complex electrical properties that EAVs can present. While the microspheres exhibit a flat dielectric spectrum over a broad range of frequencies, the EAVs undergo a dispersion at ~200 kHz, going from negative polarizability at 50 kHz to positive polarizability at 500 kHz. Figure 3-4C illustrates in greater detail the dielectrophoretic spectrum of an EAV suspension comprising a range of sizes. At 50 kHz, these vesicles have a strong negative polarizability, which weakens as the frequency is increased to 100 kHz. By 500 kHz, nearly all vesicles exhibit positive polarizability, a condition that persists up to about 2 MHz, where the higher of the two crossover frequencies is observed. These dielectrophoretic spectra demonstrate the ability of EAVs to encompass a more complex set of electrical properties than other commonly used test particles for DEP.

3.2.4 Determining membrane characteristics from cross-over frequency.

To characterize the electrical properties of individual EAVs and to compare these properties to those predicted by established theories for single-shelled spherical particles [85], we perform a series of crossover frequency measurements. This allows us to determine the conditions under which the EAVs' polarizabilities vanish [86]. Because we have experimental control over the conductivity and permittivity (σ_c and ε_c respectively) of the EAV core, we focus on the properties of the membrane, which we assume is described by a permittivity ε_{mem} and thickness δ. In a medium of conductivity σ_m and permittivity ε_m, the complex Clausius-Mossotti function at frequency ω for a vesicle is given by:

$$\underline{K}(\omega)=\frac{-\sigma_m\sigma_c+i\omega[ac_m(\sigma_c-\sigma_m)-(\sigma_c\varepsilon_m+\sigma_m\varepsilon_c)]-\omega^2[ac_m(\varepsilon_c-\varepsilon_m)-\varepsilon_c\varepsilon_m]}{2\sigma_m\sigma_c+i\omega[ac_m(\sigma_c+2\sigma_m)+2(\sigma_c\varepsilon_m+\sigma_m\varepsilon_c)]-\omega^2[ac_m(\varepsilon_c+2\varepsilon_m)+2\varepsilon_c\varepsilon_m]} \quad (1)$$

where a represents the radius of the EAV and i= √-1. Here, we have combined the membrane properties into a single capacitance-per-unit-area ($c_m \equiv \varepsilon_{mem}/\square$). To simplify this expression, we begin by addressing only the low-frequency behavior of the polarizability. This allows us to focus more directly on the contribution of the membrane to the EAVs' dielectrophoretic response. In this frequency regime, Eq. 1 simplifies to:

$$\underline{K}(\omega)=\frac{-\sigma_m\sigma_c+i\omega[ac_m(\sigma_c-\sigma_m)-(\sigma_c\varepsilon_m+\sigma_m\varepsilon_c)]}{2\sigma_m\sigma_c+i\omega[ac_m(\sigma_c+2\sigma_m)+2(\sigma_c\varepsilon_m+\sigma_m\varepsilon_c)]} \quad (2)$$

Using (2) and setting Re{$\underline{K}(\square_0)$} = 0, we find an expression for $\square_0$, the lower of the two possible cross-over frequencies permitted by Eq. 1:

$$\omega_0^2=\frac{2(\sigma_m\sigma_c)^2}{[ac_m(\sigma_c-\sigma_m)-(\sigma_c\varepsilon_m+\sigma_m\varepsilon_c)][ac_m(\sigma_c+2\sigma_m)+2(\sigma_c\varepsilon_m+\sigma_m\varepsilon_c)]} \quad (3)$$

To better understand the properties of the EAV membrane, it is convenient to rearrange Eq. 3 so as to relate the crossover frequency, which we observe directly, to □, the membrane thickness:

$$\delta=2a\varepsilon_{mem}\frac{(\sigma_c-\sigma_m)(\sigma_c+2\sigma_m)}{\sigma_c(\sigma_c\varepsilon_m+\sigma_m\varepsilon_c)}\left[4\frac{\sigma_m}{\sigma_c}-1+3\left[1+\frac{8\sigma_m^2(\sigma_c-\sigma_m)(\sigma_c+2\sigma_m)}{9\omega_0^2(\sigma_c\varepsilon_m+\sigma_m\varepsilon_c)^2}\right]^{1/2}\right]^{-1} \quad (4)$$

Measuring crossover frequency across different core and medium conductivities ($\square_c$ and $\square_m$), and across different batches of electroformed EAVs yields an effective membrane thickness of 9.3 ± 4.3 nm. Our measurements are in reasonable agreement with expectation for the thickness of a lipid bilayer and support the validity of this simple model for vesicle polarizability.

Specifically, we find that extracted values of δ are fairly independent

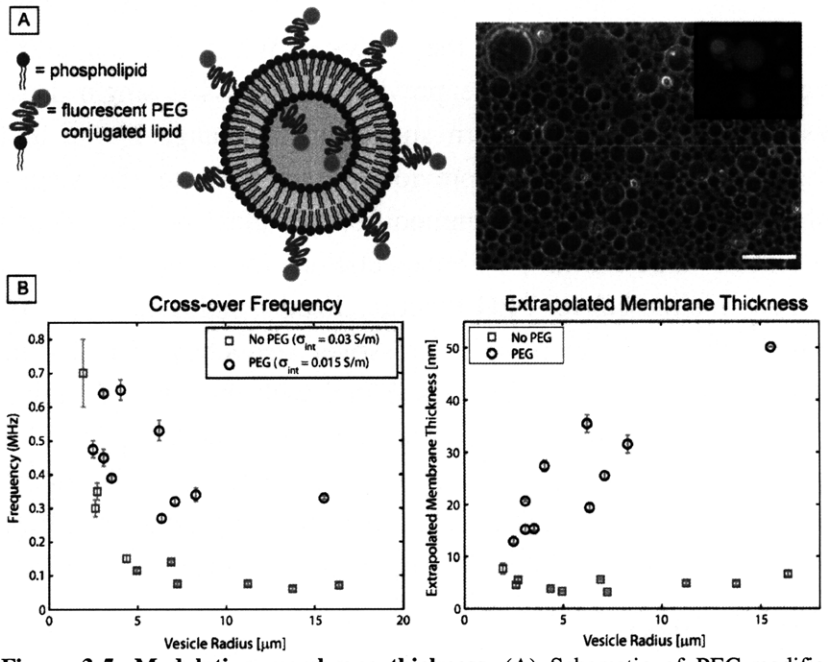

Figure 3-5: Modulating membrane thickness. (A) Schematic of PEG-modified EAV (not drawn to scale) along with phase microscopy images of electroformed EAVs (the inset shows fluorescence images of the EAVs, confirming that they are PEG-modified). Scale bar 50 μm. (B) Plot of EAV radius versus cross-over frequency and plot of estimated effective membrane thickness. While EAVs formed in the absence of PEG show a uniform membrane thickness of ~5 nm, as expected for a single lipid bilayer, PEG-modified EAVs exhibit an increased effective membrane thickness that varies with radius.

of the vesicle radius (correlation coefficient: -0.0026 across 80 individual vesicles) as well as the crossover frequency (correlation coefficient: 0.18), suggesting that Eq. 4 exhibits the correct functional dependencies of □ on these parameters. Additionally, we find that the specific fluorophore incorporated in the membrane does not lead to a change in electrical properties, with carboxyfluorescein-labeled and rhodamine-labeled vesicles exhibiting no observable difference in crossover frequency (not shown).

3.2.5 Modulating membrane capacitance

In addition to the ability to control the electrical properties of the EAVs through their aqueous core, we also demonstrate the ability to modify the vesicles' dielectric spectra through the structure and composition of their membrane (Figure 3-5A). Since the thickness and dielectric constant of the lipid membrane is fairly constant over a wide range of lipids, we decided to alter the membrane properties by incorporating into the membrane lipids conjugated with polymers, which would increase the effective membrane thickness while also altering its effective dielectric constant. We incorporated 5 mole-percent PEG-modified fluorescently tagged lipid into our membranes to verify this hypothesis. The presence of a fluorescence signal in the membrane (Figure 3-5A, inset) indicates that the PEG-modified lipid indeed organizes in to the membrane of the vesicle. As shown in Figure 3-5B, these membrane-modified EAVs displayed different electrical properties than unmodified EAVs. Using the same method for measuring the sizes and crossover frequencies of individual EAVs and interpreting the results in the context of a single-shell spherical model (Eq. 4), we are able to discern changes in the low-frequency dielectrophoretic response of the EAVs. While the unmodified EAVs exhibit crossover frequencies consistent with the previously discussed single shell model, PEG-functionalized EAVs deviate from this pattern suggesting a change in the underlying mechanism of their polarization. As mentioned previously, when fit to the single shell model, we extract a membrane thickness for the unmodified vesicles that is independent of particle radius and consistent in value (~5 nm) with expectations for a phospholipid bilayer. In contrast, extracted membrane thicknesses for PEG-functionalized vesicles increase with vesicle radius. We are able to reliably detect the increase in crossover frequency of PEG-functionalized EAVs over their non-functionalized counterparts associated with this change; however, the increasing extracted membrane thickness suggests that the single shell model of Eq. 4 with the membrane thickness δ independent of all other parameters is no longer sufficient to describe the membrane capacitance of PEG-functionalized EAVs. This may be attributable to differences in PEG conformations within membranes of different curvature, or to the effects of PEG on membrane morphology.

3.3 DISCUSSION

Our results demonstrate the feasibility of creating populations of particles with distinct and controllable optical and electrical properties. These results should open new avenues in both the characterizarion of dielectrophoretic traps and in the electrical manipulation of vesicles. Previously, DEP traps have been primarily characterized with polystyrene microspheres, which prove to be constraining in their electrical properties. Additional functionalizations and surface

chemistry[19] have been performed but they can involve considerable complexity, which makes the route to multiplexing more difficult. Micron-scale metal or metal-coated particles are challenging to fabricate and are commercially available in a very limited size range. Thus, most systems that leverage these highly conductive particles use pDEP and are limited to nanometer-scale particles, (e.g. for self-assembly [87]). Hence, EAVs fill a much needed void in the application space in metrology tools for characterizing DEP traps.

We have shown that EAVs have unique advantages over conventional test particles. However, they do have some limitations that impact the design of electrically distinct populations, specifically, the size polydispersity that results from electroformation. Nonetheless, electroformation has been the predominant technique for the generation of vesicles even though several alternate techniques for formation of vesicles have emerged. These techniques range from lipid film patterning [2], to pulsatile jet flow [88] and microfluidic sheathing flows [71]. In our hands, lipid film patterning proved extremely challenging and it was difficult to generate uniformly sized vesicles. The pulsatile jet flow techniques typically produce vesicles of very large size (> 100 μm), which would preclude their use in DEP-based microsystems for manipulating cell-sized bioparticles in the 1-50 μm size range. The use of microfluidic devices to generate vesicles involves considerable experimental complexity both in the design and operation of the device and in the subsequent generation of unilamellar vesicles by dissolution in ethyl alcohol.

Since electroformation is the predominant method of vesicle formation, it is important to understand how to design desired electrical properties in vesicle populations in the presence of size polydispersity. Size impacts electrical properties by affecting the membrane capacitance of the resulting particle; specifically, larger vesicles exhibit larger membrane capacitances and thus their low frequency dispersion occurs at lower frequencies than that of smaller vesicles. Eq. 3 shows that the crossover frequency may vary strongly with variations in the vesicle radius, a, with $\omega_0 \propto a^{-1}$ for larger vesicles (typically corresponding to a ~1-10 μm). Thus, to design a population with a known dielectric response, one approach is to operate at the plateaus of the dielectric spectra rather than near the crossover frequency, since the plateaus are less affected by size (Figure 3-5C).

Alternatively, operating at high frequency allows the electrical properties of the vesicle to be dominated by the vesicle's internal conductivity and permittivity, which are very well controlled. For intermediate- to high frequencies, the crossover frequency is determined approximately from:

$$\omega_0^2 = \frac{[ac_m(\sigma_c - \sigma_m) - (\sigma_c\varepsilon_m + \sigma_m\varepsilon_c)][ac_m(\sigma_c + 2\sigma_m) + 2(\sigma_c\varepsilon_m + \sigma_m\varepsilon_c)]}{[ac_m(\varepsilon_m - \varepsilon_c) + \varepsilon_c\varepsilon_m][ac_m(\varepsilon_c + 2\varepsilon_m) + 2\varepsilon_c\varepsilon_m]} \quad (5)$$

For sufficiently large vesicles (for which $ac_m >> \varepsilon_m, \varepsilon_c$), equation (5) becomes independent of the vesicle size, reducing to $\omega_0^2 = (\sigma_c - \sigma_m)(\sigma_c + 2\sigma_m)(\varepsilon_m - \varepsilon_c)^{-1}(\varepsilon_c + 2\varepsilon_m)^{-1}$.

The creation of two distinct EAV populations is most easily achieved by selecting the internal conductivity of one vesicle to be below that of the surrounding medium so that its polarizability is uniformly negative at all frequencies, while the other vesicle population, with internal conductivity higher than the surrounding medium, will exhibit polarization that will be positive over some (programmable) frequency range. The difference in the internal conductivity of the vesicle and that of its surrounding solution can result in an osmotic gradient. A vesicle is in osmotic equilibrium when the osmotic pressure drop arising from the solute concentration difference is balanced by the Laplace pressure arising from the tension of the membrane. This leads to the equilibrium condition $RT(c_i - c_o) = -2\gamma/a$, where R is the ideal gas constant, T is the absolute temperature, c_i and c_o are the internal and external osmolarities (respectively), γ is the membrane tension, and a is the vesicle radius. In our experiments, the difference in osmolarity is on the order of 0.5 mM (1× PBS diluted ~300×), with the higher osmolarity typically inside the vesicle, driving the flux of water into the vesicle and causing it to swell. For the membrane tension, we assume that the membrane tension $\gamma = \kappa(\Delta A/A)$, is the product of the elastic area expansion modulus (κ) and the fractional change in membrane area. For a 20 μm diameter vesicle with κ ~ 360 dynes/cm [89], the fractional change in area is under 3.5%, corresponding to a fractional change in volume of ~5%. Although a 5% increase in vesicle volume would create a corresponding decrease in the internal conductivity, in cases where the internal and external conductivities differ by ~2× this does not significantly influence the vesicles' dielectrophoretic response. Accordingly, in interpreting our experiments, we have neglected this effect. Since vesicles typically cannot withstand fractional area changes of ~10% (a volume change of ~15%), vesicles will typically rupture before the flux of water entering the vesicle has a substantial effect on the internal conductivity. Furthermore, osmotic stress can be mitigated altogether through the addition of non-ionic solutes (e.g. sucrose or glucose) to the internal or external phases.

In the case where more than two vesicle populations with distinct spectra are desired, the choice of the internal conductivity is constrained by the range of crossover frequencies, □□₀, exhibited across each subpopulation. Specifically, one wishes to pick internal conductivities that result in EAVs without overlapping dielectrophoretic responses over as large a range of frequencies as possible. To estimate the implications of this requirement, one can approximate the variation in □₀ associated with variations in both vesicle size and internal conductivity. Equating these variations and assuming □ₑ □ □ₘ gives:

$$\frac{d\sigma_c}{\sigma_c} = \frac{-[2(ac_m)^2(\sigma_c - \sigma_m)(\sigma_c + 2\sigma_m) + ac_m\varepsilon_m(\sigma_c - 4\sigma_m)(\sigma_c + \sigma_m)]}{\sigma_m[(ac_m)^2(\sigma_c - 4\sigma_m) + ac_m\varepsilon_m(-3\sigma_c - 8\sigma_m) - 4\varepsilon_m^2(\sigma_c + \sigma_m)]}\frac{da}{a} \qquad (7)$$

By narrowing the size distribution of the EAVs, and choosing the internal conductivity as prescribed approximately by Eq. 7, it is possible to create suspensions comprised of EAVs

undergoing dispersions in distinct ranges of frequency. Alternatively, as described in Eq. 5, operating at high frequency allows one to form multiple electrically distinct vesicles largely independent of the size distribution of the population. Accordingly, even in the presence of considerable polydispersity, it is possible to create populations of particles undergoing transitions from positive to negative polarizability over narrow frequency ranges.

Further control is made possible by modulating the vesicle's interior conductivity at the same time as its membrane capacitance, enabling the creation of EAV populations in which each type of vesicle has a frequency range over which it is the most polarizable member of the population. Increasing the membrane capacitance shifts the spectrum to lower frequencies, whereas increasing the internal conductivity reduces the peak polarizability of the spectra. A population of EAVs for which c_m and σ_i are controlled to vary inversely produces a set of spectra in which each member of the population exhibits the maximum polarizability within the population over a particular range of frequencies.

The modification of giant vesicle membranes with polymers has been the subject of considerable past study [90, 91], specifically in the application of studying the effects of polymers on membrane curvature. Additionally, polymers have been encapsulated within the aqueous phase of giant vesicles [92] and have been used to study compartmentalization in aqueous two-phase systems [93]. Thus, polymers such as PEG have served roles in the modification of both the internal aqueous phase properties and external membrane properties [94]. By decorating vesicles with PEG brushes we have further extended the use of polymer functionalizations to affect changes in the electrical properties of vesicles. This ability to modulate the specific capacitance of membranes has implications from the study of fundamental properties membranes (and the organization of polymers within membranes) and the use of polymer-functionalized vesicles as electrically distinguishable surrogate cells for DEP-based manipulation and separation.

In all, the ability to generate populations of vesicles with distinct polarizabilities opens new avenues for the study of electric field interactions with phospholipid vesicles. Previous work has focused on using electric fields to apply forces to vesicles to study deformations of phosopholipid membranes [95, 96], complex mechanisms of membrane fusion [70], and alterations in vesicle morphology[97]. Thus considerable effort has focused on using electric fields to study vesicles and membranes. Our work opens an avenue of investigation in the use of vesicles to study electric field phenomena, providing the ability to characterize systems that use electric field-based manipulation techniques (such as DEP). Vesicles can now find valuable applications as surrogates for living cells in the characterization of cell manipulation devices.

3.4 CONCLUSIONS

We have demonstrated the ability to generate EAVs as test particles for DEP-based microsystems. These vesicles can be specifically engineered to allow for their dielectrophoretic

manipulation in microsystems. We have demonstrated the ability to create electrically distinct particles using cross-over frequency measurements with a canonical DEP device. Further, we have shown that it is possible to alter the effective membrane thickness of EAV membranes using PEG-conjugated lipids. This shows that vesicles allow considerable control over their chemical composition (and therefore electrical properties) and lend themselves well to the generation of electrically distinct populations of test particles.

We believe these proof-of-principle studies are the first to demonstrate that the electrical properties of vesicles can be specifically engineered to allow their dielectrophoretic manipulation. The generation of EAVs form the first steps toward the development of vesicles as metrology tools for DEP-based microsystems.

3.5 MATERIALS AND METHODS

EAV Electroformation. EAVs were prepared using a previously described electroformation technique [84]. Briefly, electroformation was performed in a chamber consisting of two 50 x 75 mm indium tin oxide (ITO) slides (SPI Supplies) separated by a 1-mm-thick silicone gasket (Press-to-seal gaskets, Invitrogen). ITO slides were cleaned in 1% Micro-90 solution, 2× ultrasonic cleaned in acetone, 2× ultrasonic rinsed in isoproponal and subsequently dried with a nitrogen stream. 1-Stearoyl-2-oleoyl-glycero-3-phoshocholine (SOPC, Avanti Polar Lipids) stock solutions at 10 mg/ml concentration were first diluted to 1 mg/ml concentration (in chloroform) and subsequently pipetted on the bottom slide of the electroformation chamber. The lipid solution was then allowed to dry for approximately one hour in a vacuum dessicator. The internal aqueous solution was pipetted in the gasket reservoirs and then capped with the top ITO slide (with the conducting surfaces facing each other) and clamped with binder clips. A sinusoidal waveform (2 Vp-p, 10 Hz) was applied for two hours. For the preparation of fluorescently labeled EAVs, 1 mol% of lissamine rhodamine phosphatidylethanolamine, fluorescein phosphatidylethanolamine, or dansyl phosphatidylethanolamine (respectively, Lissamine rhodamine PE, Fluorescein PE, and Dansyl PE, Avanti Polar Lipids) was added to the 1 mg/ml SOPC solution prior to vacuum drying. For the generation of PEG-conjugated EAVs, 5 mol% of 1,2-distearoyl-glycero-3-phospoethanolamine-N-polyethylene-glycol-2000-carboxy-fluorescein (DSPE PEG2 CF, Avanti Polar Lipids) was added to the 1 mg/ml SOPC solution prior to vacuum drying.

Light Microscopy. EAVs were imaged immediately after electroformation on an inverted microscope (Axiovert 200, Carl Zeiss Microimaging) using phase microscopy. Once vesicle formation was confirmed, vesicle suspensions were aspirated from the gaskets and resuspended in iso-osmolar glucose solutions (50 mM). The difference in density allowed for the vesicles to settle to the bottom of the chamber and allowed for ease of imaging on an inverted microscope using both phase and fluorescence microscopy. All phase images were captured at 8 bit resolution using a cooled camera (SPOT RT, Diagnostic Instruments). Fluorescence illumination

was provided by an XCite 100 (EXFO Life Sciences and Industrial Division) illumination source. EGFP (Set 38, Carl Zeiss MicroImaging), Texas Red, and DAPI filter sets (31000 and 31002, Chroma Technology) were used for imaging green-fluorescent, red-fluorescent, and blue fluorescent vesicles, respectively. All fluorescence images were captured at 12 bit resolution using a cooled camera (SPOT RT, Diagnostic Instruments).

Interdigitated Electrode Array Design and Fabrication. Interdigitated electrode (IDE) arrays were fabricated using a standard gold lift-off process on pyrex substrates that has been previously described [78]. Briefly, 6" pyrex substrates were cleaned in a piranha solution and subsequently rinsed. Image reversal resist (AZ5214, Clariant) was spun on the wafers and the wafers were pre-baked at 90 °C for 30 minutes. Subsequently, wafers were exposed at 10 mJ/cm^2 for 5 seconds and then post-baked for 30 minutes at 120 °C. Wafers were then flood exposed for 10 seconds and developed for ~1 minute. A 100 Å of titanium and 1000 Å of gold were then deposited using an electron-beam deposition system. The resist was subsequently removed by immersion in an acetone bath overnight. The wafers were then diced with a diamond saw to yield individual chips.

Interdigitated Electrode Array Packaging. For our IDE devices, we packaged individual chips by mounting them on glass slides using double-sided tape. We then affixed the slides to a standard upright microscopy stage insert. We used laser-cut PDMS gaskets (250 μm thick, Bisco Silicones Inc.) around the active chip areas to form flow chambers. We then filled the chambers with vesicle suspensions and capped them with coverslips. We made electrical connections to the on-chip electrodes using alligator clips and delivered signals using an arbitrary waveform generator (Agilent 33250A).

Cross-over frequency measurements. We measure the crossover frequencies of vesicles and fluorescent polystyrene beads (F8834, Invitrogen) using an interdigitated electrode array in which the pitch and spacing of the electrodes are both 50 μm. By diluting EAVs with deionized water at a ratio of 2:1, we set the conductivity of the external medium to approximately half that of the vesicle interior. We pipette ~10μl of the diluted EAV suspension into a laser-cut silicone gasket placed over the electrode array and seal the chamber with a glass coverslip. The device is placed under a fluorescence microscope (Zeiss AxioImager, Carl Zeiss MicroImaging) and imaged using a 20× (0.5 NA) objective. Individual EAVs are selected so as to broadly sample the total distribution of sizes, down to approximately 1 μm. The electrodes are then activated at 3-5 Vp-p and frequencies ranging from ~50kHz – 1MHz while we observe the behavior of the vesicle. We narrow the range of excitation frequencies until the vesicle exhibits minimal response to the application of the electric field. We supplement this determination of the crossover frequency with an image of the vesicle, from which we determine its radius.

3.6 ACKNOWLEDGEMENTS

We thank Margaret Hornton and Luke Theogarajan for helpful discussions regarding vesicle electroformation. We thank Dominic Duvalier for helpful discussions regarding PEG-conjugated lipids. We thank Scott Manalis and the Media Laboratory for access to laser-cutter facilities. We thank Nitzan Gadish for the design of the interdigitated electrode devices. This work was supported by NIH grants (RR199652 and EB005753), the Merck/CSBi Graduate Fellowship (M.D.V.), and the MIT Buschbaum Fund (M.D.V).

3.7 SUPPLEMENTARY INFORMATION

3.7.1 EAV core conductivity sensitivity

A plot showing the percent change in internal conductivity (σ_c) needed to account for a given percent change in vesicle radius (a) to produce the same crossover frequency, based on Eq. 7 is shown in Figure 3-6. Below the dashed line, a given variance in vesicle size requires a lesser change in internal conductivity to create vesicles with a distinct crossover frequency; it is thus advantageous to operate at a conductivity ratio (σ_c/σ_m) that yields a value of < 1.

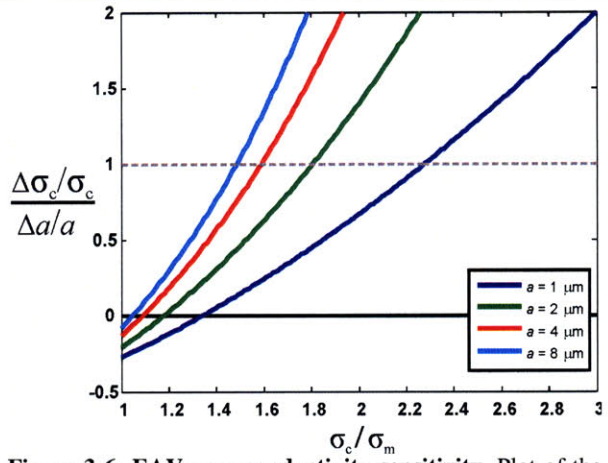

Figure 3-6: EAV core conductivity sensitivity. Plot of the percent change in internal conductivity need to account for a given percent change in vesicle radius.

3.7.2 Vesicle purification techniques

The electroformation process involves the generation of vesicles in the solution which is desired to be encapsulated within the aqueous vesicle core. In the case where these solutions are fluorescently-labeled the removal of these background solutions is desirable (otherwise the vesicle suspensions would have to be greatly diluted to enable significant contrast for fluorescence imaging). Figure 3-7 shows such a "purification" scheme where the vesicles are loaded in to a Sephadex gel column and allowed to incubate. The column is packed with a gel slurry and then a glass filter is placed on top so as to prevent any disturbances at the gel surface. Excess electroformation buffer (without fluorescent dye) is added to the column. Buffer is added as the dye diffuses through the column (as seen in Figure 3-7B) so as to continually dilute the remaining dye concentration and drive the excess buffer

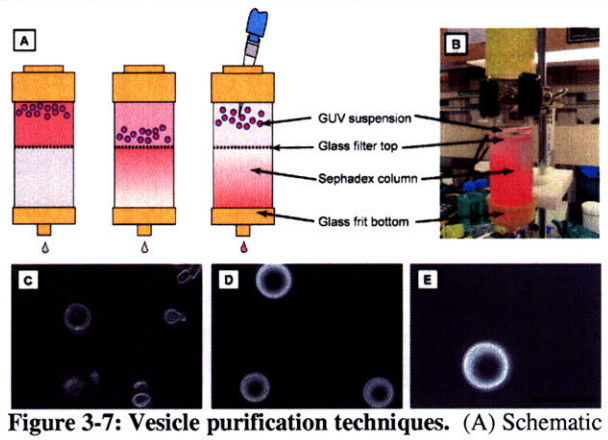

Figure 3-7: Vesicle purification techniques. (A) Schematic of the gel column used to remove the background fluorescence and extraneous lipid aggregates in the electroformed solution. (B) Photograph of setup. (C) Phase microscopy image of electroformed vesicles. (D), (E) Phase microscopy images of eluted vesicles showing that extraneous lipid aggregates have been remove and well-formed vesicles are retained. Scale bar 50 μm.

through the column with hydrostatic pressure. Once the gel-column effluent no longer appears to be fluorescently stained, the vesicle suspension is eluted from the column and imaged on a microscope. Images of electroformed vesicles before (Figure 3-7C) and after (Figure 3-7D and E) this purification step show that vesicle aggregates are effectively removed and only well-formed vesicles are retained. This specific purification process was not used with EAVs as all the EAVs were labeled with fluorescent dyes in their membranes. However, to extend the capabilities of EAVs and truly build libraries of test particles, then a more complex encoding scheme involving labeling both the membrane and aqueous core would be required. This purification scheme would thus be very valuable in the extension of vesicle libraries and in other research involving giant vesicles.

3.7.3 PEGylated EAV image processing

The incorporation of PEG in to phospholipid membranes has been the subject of considerable past research [94]. To validate that the PEGylated EAVs that we had electroformed had similar concentrations of PEG incorporated in their membranes we undertook and imaging study. This study involved the electroformation of vesicles that incorporated lissamine-rhodamine-labeled lipids in addition to the fluorescently-labeled PEG lipids. Examples of such dual-stained electroformed lipids are show in Figure 3-8A. The rhodamine-labeled lipids were used so as to aid in the visualization of the membrane. Fluorescence images from the red-fluorescence channel were thresholded and used to generate a mask for downstream image processing. As is shown in Figure 3-8A, such a mask can be easily generated and shows a distinct membrane region (indicated by the arrowhead). This mask can now be applied to the fluorescence image obtained from the green-channel (showing the PEG molecules) and the resultant image is then used for comparison to other images obtained from the same batch of electroformed vesicles. Care was taken to ensure that the PEG-images were taken at the same exposure time and under the same imaging conditions. The fluorescence intensity in the membranes identified by thresholding was then calculated and normalized to the thresholded area. Comparing this normalized fluorescence intensity across vesicles yielded values that were within ~10 % (for 50 imaged vesicles).

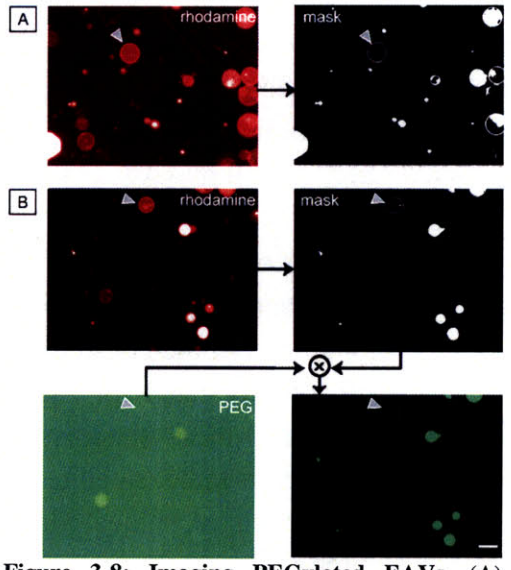

Figure 3-8: Imaging PEGylated EAVs. (A) Fluorescence image acquired using rhodamine fluorescence channel (left) and corresponding thresholded image (right) showing that the vesicle membrane can be clearly delineated (gray arrowhead). Final image (bottom right) shows clear demarcation of PEG fluorescence signal localized to the membrane (gray arrowhead). Scale bar 10 μm.

3.7.4 Lipid patterning

The electroformation process yields polydisperse populations of vesicles. The generation of monodisperse populations on the size scale of cells remains a challenging research problem. We attempted to address this problem by pre-patterning the lipid film prior to electroformation to bias the formation of specific-sized vesicles (in effect by controlling the concentration and spatial arrangement of lipid molecules available at each vesicle nucleation site). This approach has proved promising and has been previously reported [2]. To pattern the lipids we used a newly developed thermal inkjet printing system (TIPS) that enabled the jetting of various combinations of lipids (as shown in Figure 3-9A). Results of the pattern were very promising with clean patterns of lipid spots (25 μm) in diameter with 100 μm spacing. These patterns were easy to generate and alter on demand, allowing the testing of a wide parameter space which would be prohibitively time-consuming with micro-contact printing (as a new master and stamp would have to be fabricated for each design iteration). Unfortunately, when performing the electroformation step these patterns were smeared (as shown in Figure 3-9B) resulting in the formation of micron-scale satellite vesicles rather than cell-sized vesicles. The patterns generated through this technique could prove to be valuable for other research, such as in the building of large-scale lipid arrays for studying drug-lipid interactions.

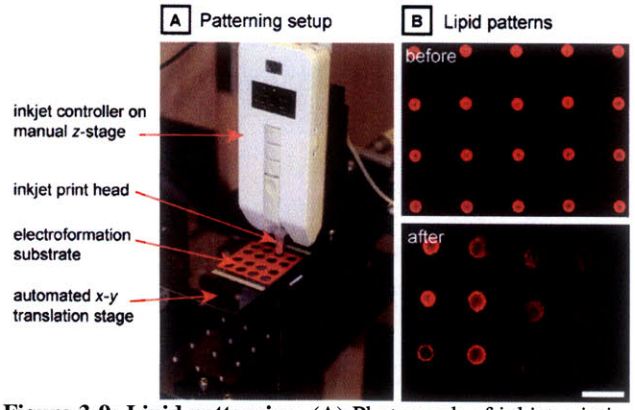

Figure 3-9: Lipid patterning. (A) Photograph of inkjet printing setup with inkjet head directly patterning in to the conductive substrate of the electroformation chamber. (B) Fluorescence image (top) of lipid patterns showing that arrays of lipid spots can be readily patterned on the size scales comparable to those previously reported for electroformation from patterns [2]. Lower image shows the smearing and washing away of patterns during the process of filling the electroformation chamber, resulting in the formation of small, satellite vesicles at the pattern site. Scale bar 50 μm.

Chapter 4 – **Electric-field Impact on Cellular Physiology**

Cells are complex and dynamic biological systems. Unraveling the complexity of cellular processes at the single cell level has important implications in biotechnology and biological engineering – from screening for small molecule drugs to building live-cell-based sensors. Obtaining information from single live cells can be both greatly simplified and highly automated using technologies for cell manipulation and patterning. These manipulation technologies could involve *active* techniques such as dielectrophoresis [98] and optical tweezers [99] or *passive* techniques such as microcontact printing of extracellular matrix proteins [100] and elastomeric stencil-based patterning [36]. Among these techniques, dielectrophoresis (DEP) has emerged as an important tool for the manipulation of live cells. Since DEP traps can leverage mature microfabrication technologies, they can scale to trap biological entities from the sub-micron range (from viruses to bacteria) to the tens of micron range (encompassing a large variety of mammalian cells). Importantly, this scalability can be used to design traps with single-cell to thousands-of-cells trapping resolution. DEP can be used for "catch-and-release" of live cells by turning traps on and off thereby enabling live-cell sorting operations. While significant work has been done in the area of DEP trap modeling, fabrication, and design, comparatively little work has been done in understanding cell health issues with regards to trapping.

This chapter presents a body of work that aims to highlight the research done in understanding cell health issues with regards to DEP trapping. After a background on DEP and likely mechanisms of electric-field-induced physiological changes, previous research work in this area will be presented and discussed. Importantly, the results obtained from previous studies guide our hypotheses of possible interactions between cells and electric fields (at dielectrophoretic trapping frequencies). These hypotheses will be tested by the construction of a DEP-based system and initial results will be presented. The limitations of the DEP-trapping based system and the need for a higher-throughput system will be discussed (details of the higher throughput system will be discussed in the following chapter, Chapter 5).

4.1 INTRODUCTION

Although dielectrophoresis has been used to manipulate cells, little is understood about the electric field effects (at dielectrophoretic trapping frequencies) on or their coupling with cellular physiology and behavior. Nevertheless, electrical fields will result in temperature gradients around the cell and result in direct cell-field interactions which could lead to alterations in cellular behavior. These changes in cellular behavior could be relevant both in understanding the cellular processing of physical forces and more importantly in determining the optimal conditions for cellular manipulation using electric fields.

Manipulating cells, irrespective of the technique, will certainly have some effect on cellular behavior and physiology. Clearly, each manipulation technique will have a different level of physiological impact which will dictate its guidelines for usage and the appropriate controls necessary. For example, trypsinization of adherent cells is routinely used as a technique for cell manipulation and is known to affect certain cellular pathways [101]. However, by allowing cells sufficient time to recover from this enzymatic manipulation we can still perform meaningful experiments without the manipulation technique itself occluding the results. Consequently, it is imperative that we understand the effects of DEP trapping on cellular physiology over a range of trap operating conditions for two main reasons – (1) to determine whether there are any gross effects (such as viability and changes in proliferation rate) that preclude the use of DEP traps altogether at certain operating regimes, and (2) whether there are more subtle effects (such as the activation of signaling pathways) that mask or alter particular phenotypes of interest. The results will dictate the optimal operating regimes and the types of controls necessary for using DEP-based cell manipulation in the future.

4.2 Hypotheses and Objectives

To address the main motivating factors for this study of electric-field impacts on cellular physiology, I have outlined the following hypotheses which will serve to guide this study and form a framework of assays detailed in this and the next chapter (Chapter 5).

Hypothesis 1: I hypothesize that an electric field could alter the physiological state of a cell in a dielectrophoretic trap by activating the cellular stress response pathway of the cell.
Objective: To determine the effect of an applied sinusoidal trapping waveform over a wide range of field strengths, frequencies and durations on the synthesis and activation of proteins comprising the cellular stress response pathway.

Hypothesis 2: I hypothesize that an electric field could alter the physiological state of a cell in a dielectrophoretic trap by altering the transmembrane voltage of the cell.
Objective: To determine the effect of an applied sinusoidal trapping waveform over a wide frequency range of field strengths, frequencies and durations on the transmembrane potential of the cell.

Hypothesis 3: I hypothesize that an electric field could alter the physiological state of a cell in a dielectrophoretic trap by compromising its viability and its ability to proliferate
Objective: To determine the effect of an applied sinusoidal trapping waveform over a wide frequency range of field strengths, frequencies and durations on the viability and proliferation rate of the cell.

4.3 Dielectrophoresis (DEP)

DEP refers to the action of a cell in a spatially non-uniform electric field. When a cell is placed in an electric field, an electric dipole is induced in the cell. In the case of DEP, the spatial non-uniformity of the field results in an imbalance in the electrical forces pulling on each half of the dipole. This force imbalance pushes the cell either to the maximum field intensity in the case of positive DEP (pDEP) or the minimum field intensity in the case of negative DEP (nDEP). Whether a cell experiences nDEP or pDEP is dependent on the relative polarizabilities of the cell versus the media it is suspended in. The two schemes of DEP trapping are outlined in Figure 4-1, where cells are trapped using a planar interdigitated electrode geometry.

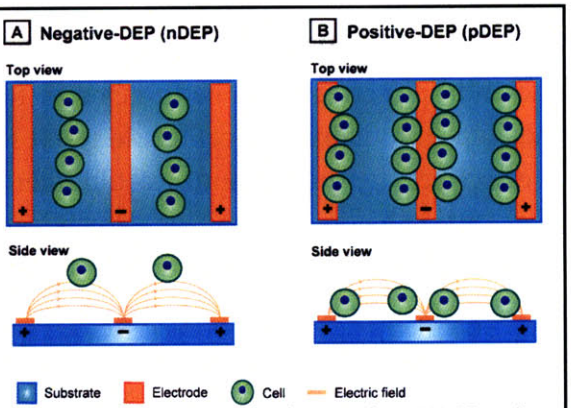

Figure 4-1: Dielectrophoretic trapping. (A) Negative dielectrophoresis involves the patterning of cells at the lowest field regions, specifically between the electrodes in the case of interdigitated electrodes. (B) Conversely, positive dielectrophoresis involves the patterning of cells at the high field regions, specifically at the electrode edges in the case of interdigitated electrodes. nDEP patterning can be performed in physiological media, such as those used for routine cell culture, and therefore is more amenable to live-cell studies. pDEP is performed in low conductivity buffers, though more likely detrimental to cell health provide the benefit of decreased Joule heating.

Long-term studies of trapped or patterned cells necessitate the use of physiological buffers for cell manipulation. To this end, nDEP techniques are utilized [102-105] because the cells can be suspended in physiological solutions such as standard cell culture media (typically Dulbecco's Modified Eagle Medium). This enables cells to be viable within the trapped regions for longer periods of time and in the case of adherent cells enables attachment without the need for switching buffers. Furthermore, nDEP traps position cells at the region of the lowest electric field and hence are less likely to have a gross influence on cellular morphology and physiology than a equivalent pDEP trap. Conversely, pDEP traps [106] use non-physiological, low conductivity buffers (on the order of 0.01 S/m) and hence are less suited for long-term studies. Unlike nDEP traps, pDEP traps position cells in the high field regions at the electrodes. However, as pDEP traps pull cells towards the electrodes they are relatively easier to design and construct compared to nDEP traps. In addition to low-conductivity buffer operation these traps can in some cases result in the cells irreversibly sticking to the electrodes [107]. Thin dielectric layers serve as a technique to prevent this type of sticking enabling the subsequent release of cells [108], however this involves an additional step of cleanroom processing.

This thesis outlines techniques for studying physiological impact using either nDEP or pDEP and is essentially trap architecture independent, though the primary focus is on studying physiological impact in standard cell culture media (as in the case of nDEP as it is the most commonly used trapping scheme for long term cell studies). In the context of these trapping schemes, it should be emphasized that the trap architecture described in this chapter is that of a

canonical interdigitated electrode design (as schematically depicted in Figure 4-1). In choosing this design, my aim was to present results that could be extrapolated to other trap designs. Moreover, in the following chapter, a system that utilizes uniform fields (and therefore DEP-independent) is described and is even more generalizable to other techniques that utilize electric fields such as electrophoresis. Further, while all the experiments in this thesis are performed in physiological media, the techniques and the microfabricated platform described herein could equally be used for more in-depth studies using lower conductivity media, with the caveat that the physiological impact of these low-conductivity media first be tested on the cells independently (using a panel of stress-activation assays, to determine if there are responsible for appreciable levels of physiological stress).

4.4 Electric field effects on cells

Electric field effects can be grouped in to (1) current based – Joule heating in the conductive medium surrounding the cell could result in the initiation of the stress response, (2) charge based – direct cell-field interactions could alter the transmembrane potential of the cell and thereby alter the behavior of voltage dependent proteins such as voltage-gated ion channels, (3) electrochemical – the generation of an ionic current in the liquid medium could result in the generation of radical species, and (4) migratory – DC electric fields exceeding 1 V/cm occur during wound healing, morphogenesis, and tumor growth, and such fields have been shown to induce directional migration of a variety of different cells [109].

The coupled nature of the current and charge-based interactions may prove to make it difficult to pin-point the contributions of each effect independently on the physiological state of the cell. As will be discussed in the next chapter (Chapter 5) of this thesis, the decoupling of these parameters and the study of membrane depolarizers will be presented. These results will be presented in the context of the stress-reporter cell line developed and discussed in the context of Chapter 5.

4.4.1 Thermal effects and cellular stress

Media typically used to culture cells have high electrical conductivity, on the order of 1 S/m. Consequently, electric fields in conducting media such as DMEM-based cell culture media or phosphate-buffered saline (PBS) will cause power dissipation in the form of Joule heating. A cell in a DEP trap operating in cell culture medium (or PBS) will experience a temperature gradient in its vicinity which could have a profound effect on cellular physiology. Elevated temperatures above 46°C can lead to rapid cell death in the case of mammalian cells [110, 111]. Temperature excursions in the 39°C to 44°C range constitute "heat shock" and activate the cellular stress response comprising molecular chaperones involved in protein homeostasis. Additionally, there is evidence that suggests that in response to stress the cell begins to actively inhibit transcription of various genes and transitions in to a transcriptionally quiescent state [112]. This has important

implications for trap operation and design, and a common guideline is to keep variations to less than 1°C (around 37 °C), which is the approximate daily variation in body temperature [113].

The exact steady-state temperature rise in a DEP trap is determined by the details of electrode geometry and the operating characteristics. However, the temperature rise has been shown to scale as [114],

$$\Delta T \sim \sigma \cdot V^2 \cdot L^3 \qquad (1)$$

where, σ is the conductivity of the medium, V is the applied voltage and L is the characteristic length scale of the trapping system. For a given trap geometry and medium, V can be varied to determine the temperature changes in the system and thereby determine the appropriate cut-offs for operation, using the previously mentioned 1°C guideline. To obtain a more detailed map of temperature in a DEP trap for various trap operating frequencies, field strengths and durations, subsequent sections will describe the use of microfabricated thermistors located at each electrode site to measure temperature. These thermistors allow *in situ* measurements of the microenvironment within a canonical DEP trap and provide valuable feedback as to the magnitude of the stressors acting on the cell.

4.4.2 Direct cell-field interactions

Living cells have a maintained difference of electric potential of ~70 mV across the plasma membrane which is termed as the resting potential [115]. This potential arises from the high permerability of potassium ions across the membrane through ion channels and ion pumps that maintain the potassium ion concentration (and consequently resting potential). This endogenous resting potential changes in response to numerous physicochemical variables such as – temperature, pH, extracellular ion concentrations and extrinsic electric current. These membrane potential changes can have profound effects on cellular behavior and function across a variety of mammalian cell types. For example, (after Weiss [115]) – in secretory cells, changes in the membrane potential initiate the secretion of a chemical substance and in pre-synaptic cells, neurotransmitters are released at chemical junctions in response to changes in its membrane potential. Additionally, changes in the membrane potential can also affect the mechanical properties of cells (after Weiss [115]) – membrane potential changes result in contractions in muscle fibers and affect the beating of cilia in ciliated cells. Thus electric field interactions at the membrane could have a profound effect on the electromechanical properties of a cell

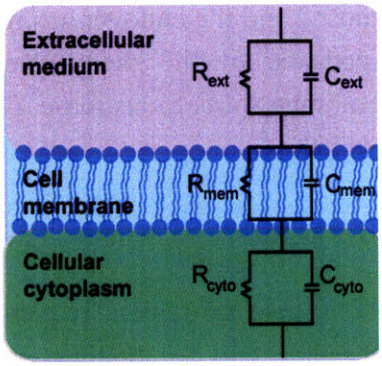

Figure 4-2: Lumped element electrical model of the cell. The model consists of three capacitor-resistor pairs in series representing the cellular cytoplasm, the cell membrane and the extracellular medium respectively. The transmembrane voltage is equivalent to the voltage across the membrane capacitor.

and thereby alter its physiological state.

Extrinsic fields at DEP trapping frequencies – in the 100's kilohertz to 10's megahertz range – could interact with the endogenous transmembrane potential either indirectly through temperature changes or by direct mechanisms [116]. At lower frequencies, the applied voltage is dropped across the membrane capacitor, making alterations in membrane physiology more like. For example, on possible effect of DEP on transmembrane potential is to alter the behavior of voltage-gated ion channels and consequently disrupt the transport of ions across the membrane [117]; this could have a profound impact on electrically excitable cells such as neurons. It is also likely that membrane proteins themselves could alter their conformations based on external stimulation. For example, there is evidence that some membrane-bound ATPases respond to fields in the kilohertz to megahertz range [116]. Electrofusion and electroporation are observable phenomena that are more severe manifestations of electric-field membrane coupling mechanisms [118], but they are outside the realm of the field strengths and frequencies typically used for DEP.

We can understand electric field interactions by considering a simple electrical model of a mammalian cell as a sphere consisting of cytoplasm surrounded by a plasma membrane as shown in Figure 4-2. Furthermore, we can use a qualitative electrical model of the membrane as a parallel resistor-capacitor network circuit connected in parallel. At low frequencies from the hertz to kilohertz range, the capacitor is effectively an open circuit and there is a voltage drop across the membrane. This is due to the fact the membrane resistance is comparatively higher than the intrinsic (cytoplasmic) and the extrinsic (external media) resistances respectively. This voltage drop across the membrane is derived from the externally applied field. Hence, the total potential difference across the cell membrane would be given by the superposition of the imposed and the endogenous resting potential. At higher frequencies in the megahertz range, the impedance of the membrane capacitor decreases sufficiently that the voltage across the membrane starts to decrease. Quantitatively, the imposed transmembrane voltage can be derived as [119],

$$|V_{tm}| = \frac{1.5|\mathbf{E}|R}{\sqrt{1+(\omega\tau)^2}} \tag{2}$$

Where, ω is the radian frequency of the applied field, $\mathbf{E}$ is the electric field magnitude, R is the cell radius, and τ is the time constant, which is given by,

$$\tau = \frac{Rc_m\left(\rho_{cyto} + 1/2\rho_{med}\right)}{1+Rg_m\left(\rho_{cyto} + 1/2\rho_{med}\right)} \tag{3}$$

where ρ_{cyto} and ρ_{med} are the cytoplasmic and medium resistivities (Ω-m). At low frequencies, equation (2) can be rewritten as below,

$$|V_{tm}| = \frac{1.5|\mathbf{E}|R}{\sqrt{1+(\omega\tau)^2}} \approx 1.5|\mathbf{E}|R$$
$$|E_{tm}| \approx |V_m|/t = (1.5R/t)\cdot|\mathbf{E}| \quad (4)$$

Hence, $|V_{tm}|$ is approximately constant at $1.5|\mathbf{E}|R$ but decreases above the cut-off frequency ($1/\tau$). This indicates that at the membrane the imposed field is multiplied by a factor of $1.5R/t$ (which is approximately a factor of 1000). Clearly, this can lead to quite large membrane fields.

As in the case of thermal effects (discussed in the previous section), we require guidelines for trap operation to mitigate physiological impact. One possible guideline for minimizing induced transmembrane potential is to keep $|V_{tm}|$ much lower than 70 mV [120], the assumption being that any imposed voltages that are lower than the resting potential would likely have minimal potential and be within the range of variation of V_{tm} in constitutive physiological processes. To tease apart the effects due to thermal stressors and direct cell-field interaction, I will use low conductivity media to minimize Joule heating and isolate the direct cell-field interaction component of the stress response. Efforts have been made to directly measure these membrane potentials using fast-switching dyes (such as di-8-ANEPPS) and custom-built, high-speed microscopy systems, which require both significant technological development and keen experimental design [121, 122] and have not been experimentally explored in this thesis work.

4.4.3 Electrochemical Effects

Generation of reactive oxygen species (ROS) and phenomena resulting from their action on cells such as lipid peroxidation have been previously observed during electroporation experiments. Among ROSs, hydrogen peroxide (H_2O_2) is probably one of the most important products engendering long-term effects due to its ability to break down in the presence of transition metal ions to produce the most reactive and damaging of the oxygen free radicals, the hydroxyl radical [123]. Furthermore, it has been shown that hydrogen peroxide can cause modifications and damage to cells [124]. Specifically, it can alter cell membrane permeability and can cause temporary or permanent cell cycle arrest, apoptosis, senescence and necrosis. In the case of temporary arrest of cells in one or more phases of the cell cycle, the cell cycle time will be prolonged. These electrochemical effects can play a role in both DC and AC fields, and work presented in subsequent sections and Chapter 5 will describe experiments used to elucidate the contribution of these electrochemical effects and their role in the activation of the stress response.

4.4.4 Migratory Effects

DC electric fields of 1–2 V/cm have been shown to orient the movements of a wide variety of cells in vitro [125]. Because similar electrical potentials occur across wounds in mammalian skin and cornea, and even larger electric fields (up to 5 V/cm) have been measured in developing limb buds [126], it has been proposed that endogenous, electric fields play a significant role in

directing cell movements during development and wound repair [127]. Application of an external voltage to counter these fields can inhibit normal cell migration in limb buds [128], while supplementing this endogenous field can accelerate it [129]. In particular for mammalian tissues, electrical stimulation has been shown to promote epithelization of epidermal wounds [130] and re-growth of nerve axons across experimentally severed spinal cords [131]. As these effects have all been observed using DC fields, it is unlikely that such effects would be observed with AC fields at the high frequencies (>200 kHz) used in this thesis. However, as migration has been largely explored at such frequencies and in AC fields, and given that it such a pronounced phenomena at DC, experiments will be performed to investigate if there is any biased migration.

The architecture for performing DEP experiments in this chapter is directly impacted by cell migration, however, there was no consistent bias to the migration suggesting that the cells were merely aligning themselves along electrode edges rather than migrating to a specific electrode. In the following chapter (Chapter 5) a new architecture is described which utilizes a transverse, parallel plate electrode (i.e. cells cannot migrate along the electric field axis). Hence this particular migration response has not been quantified across a wide range of field conditions.

4.5 Prior studies

Several studies have specifically investigated the consequences of DEP manipulation on cell physiology. These studies cover a number of different mammalian cell types, various electrode geometries and both nDEP and pDEP trapping methodologies. Most of these studies have examined gross indicators of cellular physiology, such as — viability, morphology and proliferation. Largely, these studies have provided information affirming that these gross parameters remain unchanged [132-135], with the exception of Archer *et al.* [136] whose work provided evidence of slight upregulation of the gene *fos*. A summary of a selected few past studies provide insight in to the kinds of mechanisms that might alter the physiological state of cells and are pertinent to the kinds of questions this chapter addresses.

Archer *et al.* [136] performed pDEP trapping (using sawtooth interdigitated electrode arrays) of fibroblast-like BHK 21 C13 cells and monitored cell morphology, cell doubling time, mitochondrial stress using the MTT assay, and alterations in expression in immediate-early fos-protein and non-specific gene transcription [136]. In addition they measured the steady-state temperature using a thermocouple and determined it to be less than 1°C for an applied field of approximately 10^5 V/m at 5 MHz for 15 minutes. It should be emphasized that these experiments were performed in non-physiological, low conductivity (approximately 10 mS/m) solutions required for pDEP operation. By comparison physiological media used for nDEP trapping experiments have two orders of magnitude higher conductivity which could result in appreciable temperature rises. They also calculated the imposed transmembrane potential for their operating parameters and found it to be on the order of 100 μV, which presumably has little effect. In addition, they observed 20-30% upregulation of fos expression and a upregulation of a few unknown genes (determined via mRNA fingerprinting). Though this study does not involve

nDEP trapping it provides insight in to the range of molecular biology assays that have been performed on cells post-trapping. This study suggests that most changes in cellular physiology due to DEP trapping will most likely be subtle, in the form of increased expression of select genes, rather than gross, in the form of changes in morphology. Hence, it is imperative that the biological assays performed to determine physiological state have sufficient dynamic range to capture these subtle changes.

Studies with nDEP trapping (using planar quadrupole electrode geometries) were performed by Fuhr *et al.* [137]. They investigated viability, anchorage time, motility, cell growth rates, and lag times after subjecting L929 and 3T3 fibroblast cells in saline to short (on the order of hours) and long (up to 3 days) exposure to 30-60 kV/m fields at 10-40 MHz. They estimated that the transmembrane load was less than 20 mV. In this case, the fields had no discernable effect. However, they did not monitor temperature or perform assays at the molecular level and hence were not able to discern subtle effects like gene upregulation.

Wang *et al.* [138] performed assays on field-treated media to determine whether hydrogen peroxide was generated during field exposure. They found that for all conditions under which cell growth was delayed by field exposure, the media tested positively for hydrogen peroxide, thus confirming that hydrogen peroxide was indeed produced in the medium during field exposure. In subsequent experiments to determine whether hydrogen peroxide production depended on the particular cell suspending medium used in their experiments, they carried out field exposure experiments in which a custom-media formulation (Roswell Park Memorial Institute 1640 media, developed by Moore et al. [139], commonly referred to as RPMI-1640) was replaced by PBS (phosphate-buffered saline) or KCl, and/or sucrose/dextrose solution was replaced with sorbitol, inositol or pure sucrose solution. None of these changes resulted in any difference in the growth curve study or the hydrogen peroxide assay. In another experiment, they made medium of water and RPMI only, in this case the field-treated medium tested negative for H_2O_2, showing that sugar was required for H_2O_2 production. To eliminate the possibility that sugar-oxidizing enzymes such as glucose oxidase were present due to impurities of the sugar or other ingredients in the cell suspending medium they performed subsequent experiments and determined that the H_2O_2 generation during field exposures depended on the presence of sugar but not on any sugar-oxidizing enzyme. These seminal studies of electrochemical effects in the context of DEP show that the cell suspension medium can play a role in exerting physiological stresses and that by tailoring this medium (either by removing sugars or adding appropriate oxygen scavengers) the impact of these stresses can be mitigated.

Li *et al.* demonstrated that endothelial cells (specifically, bovine arterial endothelial cells, BAECs) do indeed respond to DC electric fields (at amplitudes of 5 V/cm), migrating specifically toward the cathode. In order to understand the underlying molecular mechanism for this effect, they also examined the reorganization of the actin cytoskeleton during field-induced migration [140]. Endothelial cells normally migrate by projecting broad, actin-filled

lamellipodia; so one way an electric field could steer endothelial migration is by polarizing the assembly and/or movement of actin filaments within the cell. Further, Li *et al.* showed that specific changes in the amount and distribution of actin filaments (using immunofluorescence) in electrically stimulated cells that indicate that electric fields can re-orient endothelial cells by redistributing sites of actin filament assembly. These studies point to the role of direct cell-field interactions with the ability of external fields to modulate the protein structure of the cells. My experiments involved the use of image-based, morphometric techniques to assess the morphology of the cells and make quantitative comparisons before and after electric field exposure.

In the context of DEP, the above studies using nDEP and pDEP trapping methodologies shed light on the complexity of the questions being addressed in this thesis, both in verifying the optimal trapping conditions and in determining the physiological state of the cell. Studying the expression of single genes or proteins provides little information about other pathways that might be perturbed and hence no definitive statements can be made regarding cellular behavior.

4.6 Assaying physiological state

The prior work on cell health and electric fields has focused on gross assays and primarily on morphology and proliferation. One of the major goals of this thesis is to extend these gross assays to molecular assays to enable the detection of more subtle changes in phenotype. The motivation for studying these subtle changes in physiology are three-fold – (1) to provide both the engineering community with information regarding optimal DEP operation regimes, (2) to provide the biological community with information regarding subtle changes in gene expression that could occur during DEP-based and (3) build a knowledgebase of pathways that are coupled with electric fields to advance fundamental scientific understanding of coupling of electric fields with cellular physiology.

There are a plethora of probes within a cell to assay for physiological state. Some of these probes are illustrated in Figure 4-3. These probes range from phosphorylated signaling intermediaries to chaperone proteins and proteins involved in stalling the translation of mRNAs. Since I hypothesize that the cells may experience elevated temperatures due to electric fields the

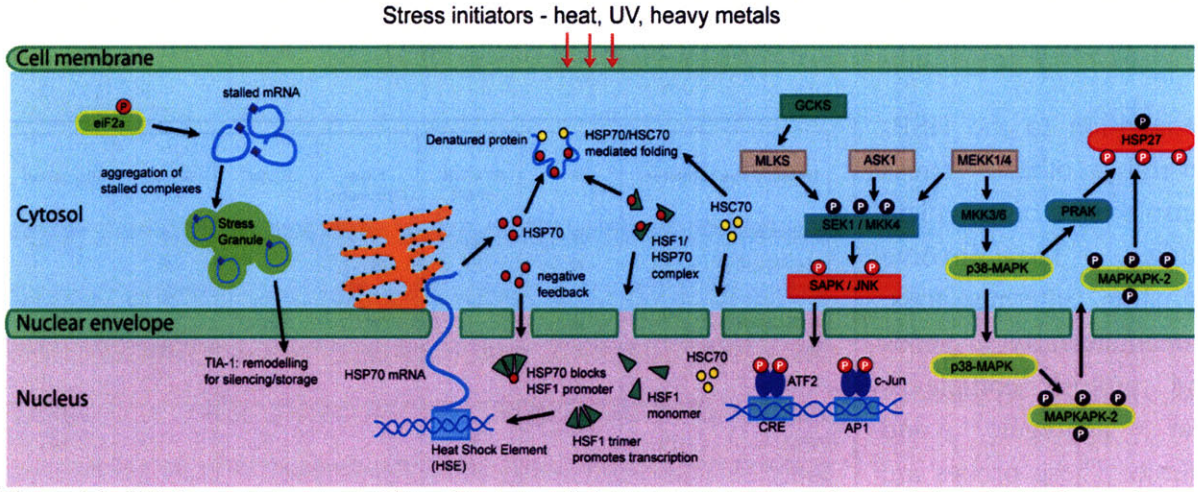

Figure 4-3: Cellular stress response. The endogenous cellular stress response is orchestrated through signaling pathways that culminate in the expression of heat shock proteins (HSPs). The stress-activated protein kinases (SAPKs) are phosphorylated and play an important role in mediating the expression of the HSPs. Additionally, these SAPKs couple with MAP-kinase pathways through a signaling intermediary MEKK4. The MAP-kinase pathway culminates in the activation of p38 and also couples with the HSP27 pathway. HSP27 in turn is phosphorylated as MAPKAPK-2 and this phosphorylation event could also be used as a marker for stress. Central to the stress response is the HSP70 pathway which is a robust stress indicator and the upregulation of HSP70. Additionally, the translocation to the nucleus of its cognate, HSC70, serve as an important component of the cellular stress response. The eIF2α pathway can possibly serve as a morphological indicator of stress as it involved in the mediation of translation by binding mRNAs and stalling the cells ability to make proteins. The phase-dense complexes formed by eIF2α and TIA-1 are termed as "stress granules". These granules are visible under standard light microscopy techniques and could potentially serve as morphological analogs to gene expression assays.

physiology of the cell with regard to stress is what I am most interested in. The cellular stress response has been widely studied and is dominated by the heat shock proteins (HSPs) [110]. These proteins, which are expressed in all major cellular compartments, perform a wide variety of cellular functions such as – protein folding, assembly, secretion, regulation, trafficking as well as assisting in the degradation of other proteins in unstressed cells. Upon exposure to stressors, especially those that affect the protein machinery, certain HSPs are induced and expressed at high levels (such as HSP70). These HSPs play a pivotal role in protecting the cells by maintaining protein homeostasis.

The small HSP family (ranging in size from 12- to 93-kDa) to which HSP70 belongs are expressed at low levels in normal cells but exhibit a 10-20 fold increase under stressful conditions [113]. Additionally, the small HSPs show different expression patterns and tissue localization during growth and development alluding to a major regulatory role [112]. The HSP70 family is one of the most highly conserved gene families consisting of both constitutive and inducible forms that differ in terms of their cellular distribution. Cytosolic forms of HSP70s are critical for post-translational translocation of newly synthesized proteins from the cytosol into the endoplasmic reticulum in an ATP-dependent fashion [112]. Additionally, this family has

been reported to play a critical role in the folding of complex proteins [141]. Interestingly, during stressful conditions, HSP70s have been reported to play a very important role in thermotolerance [142]. Thermotolerance involves a unique buffering response of the cell to stressful conditions by upregulating the expression of heat-shock proteins and allowing them to remain in the cytosol to counter future stressful conditions. Hence mild heat shocks followed by more severe shocks show different dynamics of expression compared to non-graded heat shock stimuli.

In addition to the HSPs several other stress sensors have been widely studied. They involve signaling intermediaries, immediate/early genes and protein complexes that aggregate and shuttle. These probes are highlighted in Figure 4-3 and enumerated in more detailed in the table below along with the specific techniques used to assay for these probes. They cover a wide range of time-scales of response ranging from early signaling events on the time scale of minutes to intermediate events on the time scale of tens of minutes involving shuttling of proteins from the cytosol to the nucleus and the formation of protein complexes, to transcriptional events on the time scales of hours of immediate/early genes involved in the cellular stress response. From a practical standpoint, all the genes/proteins enumerated in the table below could not be studied. As a first pass at paring the down this list, we realize that the ELISA and Western blot techniques require on the order of a million cells. DEP trapping a million cells with the same trapping conditions could prove to be a difficult task. Hence, the techniques that are most amenable are immunofluorescence (IF)/image cytometry, flow cytometry and RT-PCR. Microarray techniques are also a possibility, however the amplification steps required for samples with small numbers of cells, i.e. less that 100,000 cells can introduce significant biases [143] and hence these techniques have not been explored in this thesis. Appropriate control probes such as housekeeping genes which are known to be stress independent (such as GAPDH) have also been selected. Results for control experiments where cells were heat shocked and then assayed using IF, flow cytometry and RT-PCR, are discussed in the Methods section and outlined in the figures in the Results section. Further, the trade-offs of

Protein/Gene of interest	IF	RT-PCR qPCR	Flow Cytometry	ELISA	Western blot	Microarray
phospho-ERK	●		●	●	●	
phospho-JNK	●		●	●	●	
phospho-p38	●		●	●	●	
phospho-eIFα	●		●	●	●	
phospho-hsp27	●		●	●	●	
TIA-1	●					
HSF-1	●		●			●
c-fos		●				●
c-jun		●				●
HSP70	●	●		●	●	●
HSP90		●		●	●	●
HSP27		●		●	●	●
HSC70	●	●		●	●	●
GAPDH [control]		●				●
18S [control]		●				●

Table 4-1: Probes for physiological state. The various signaling intermediaries, proteins and genes studied as possible candidates for markers for physiological state. The proteins/genes are listed alongside techniques that are typically used to assay for these techniques. ELISA, Western blot and microarray-based assays have not been considered in this chapter due to the requirement of large numbers of cells. Instead, I chose to focus on immunofluorescence, PCR and flow-cytometry based techniques.

measuring protein translocation, gene expression, and signaling cascades is provided in the Discussion section.

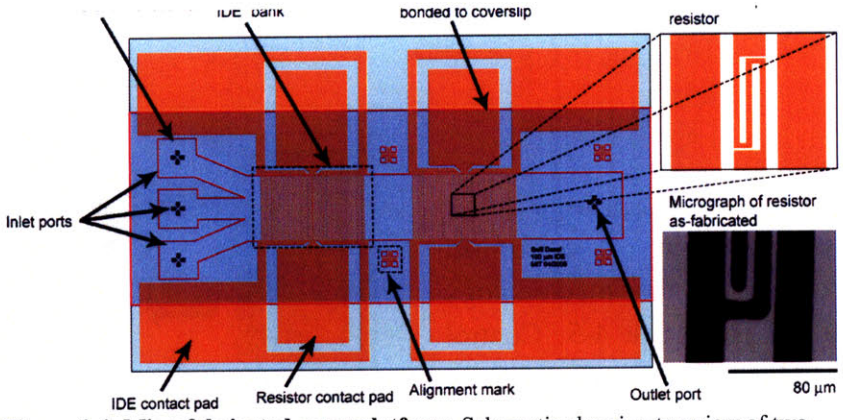

Figure 4-4: Microfabricated assay platform. Schematic showing top view of two banks of IDE arrays with microfluidic channels superimposed (light blue). The inset shows the resistor architecture and an actual image of the resistor showing as-fabricated dimensions in the 8-10 µm range.

4.7Assay platforms

To perform these experiments we required the design of both a macroscale platform for performing the positive and negative control experiments and a microscale platform consisting of a DEP device for studying the effects of electric fields. These assay platforms were specifically designed to allow for the study of small numbers of cells (~1000s) as compared to more traditional dish-based culture platforms (~100,000-1 million of cells). These platforms fit in to a larger assay methodology which is detailed in Figure 4-5. The flaskette (Nunc Inc.) was chosen as the "macroscale" platform as it had a format comparable to that of a glass slide (amenable to automated microscopy) and a culture chamber that could be tightly closed and therefore more easily isolated for use in cellular stress experiments. The microscale platform consisted of an array of interdigitated electrodes that serve as a canonical device for DEP manipulation (and has been widely used for both pDEP and nDEP-based manipulation of live cells [136, 144]). These interdigitated electrode arrays were fabricated using standard microfabrication techniques (as delineated in the methods section). Each electrode array chip consists of dual banks of independently controlled electrodes, and each bank has a fabricated resistor for *in situ* temperature measurements. A simplified schematic of the device is detailed in Figure 4-5.

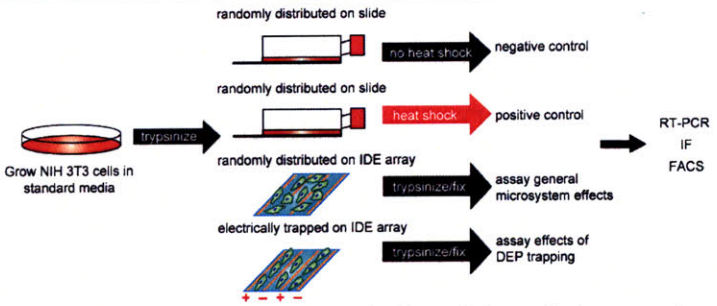

Figure 4-5: Assay methodology. Outline of the techniques used to perform the assays using the same cell passage number at the "macroscale" using flask-on-slide culture chambers and microscale IDE chips (with similar form factors to a slide).

4.8 Assay methodology

Assays were performed according to the methodology outlined in Figure 4-5. Control experiments were all done in flaskettes to hone techniques that could be applied to the assays performed on the IDEs. Detailed techniques on the methodology for individual assays can be found in the Methods and Supplementary Information section.

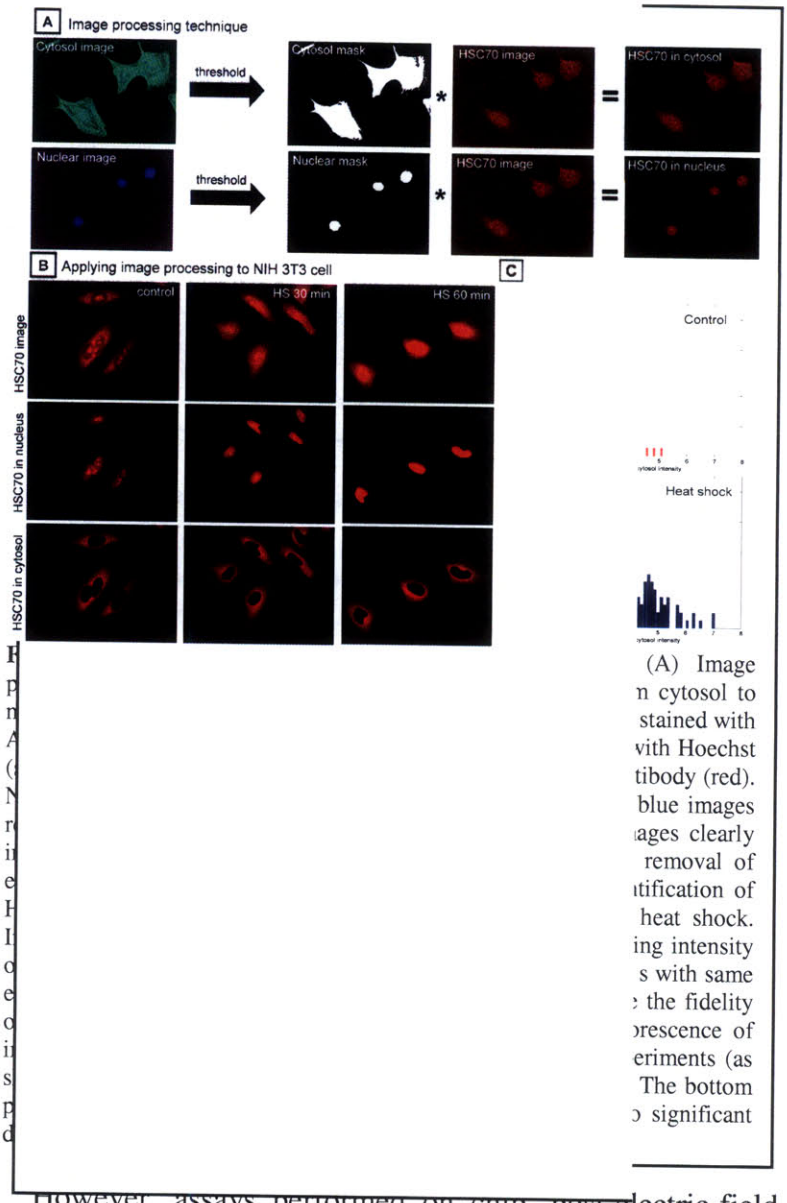

(A) Image
n cytosol to
stained with
vith Hoechst
tibody (red).
blue images
ages clearly
removal of
itification of
heat shock.
ing intensity
s with same
the fidelity
orescence of
eriments (as
The bottom
significant

4.9 RESULTS

Immunofluorescence and image cytometry. Image cytometry of translocation of HSC70 was readily detectable using the flaskette platform as is shown in Figure 4-6. Quantification of immunofluorescent images showed a significant difference between the control and heat shocked population (using t-test). However, assays performed on chip, post-electric-field exposure showed inconclusive results with no significant difference detectable (Figure 4-6C).

Gene expression. Upregulation of HSP70 between control and heat-shocked populations is robustly detected using gel electrophoresis techniques, as shown in Figure 4-7A. Assays performed on-chip, however, only show a slight upregulation in HSP70 as shown in Figure 4-7B. This might likely be due to migration of cells to different regions of the chip prior to electrical stimulation, resulting in a weaker and possibly more heterogeneous response.

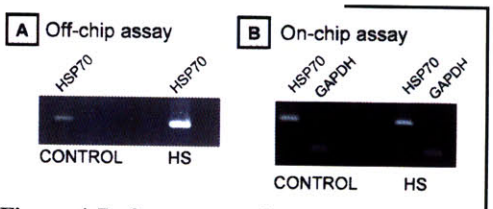

Figure 4-7: Gene expression assays. Off-chip control assays (A) show significant upregulation whereas those on-chip (B) only show slight upregulation.

Kinase assays. Immunofluorescence assays coupled with flow cytometry analysis indicate that phosphorylation of stress-activated protein kinases (SAPKs) such as JNK are detected (see Figure 4-8). In this case, cells were serum starved (1% serum v/v in cell culture media) for 24hrs, pulsed with arsenite for 30 min (see Materials and Methods) and washed in PBS. Cells were then immediately fixed and stained. However, the use of serum starvation techniques [145] to reduce background phosphorylation poses some concerns as an additional experimental condition that could confound downstream biological analysis. However, a more challenging problem arose from the fact that these results were not easily repeatable, due to the fact that cells needed to be fixed, stained and then subsequently trypsinized. This is contrast to standard protocols for the immunofluorescent staining where cells are first trypsinized then fixed and stained. This alternate technique was chosen to allow for experiments where ~10,000 cells could be used. When starting with such small numbers of cells, the repeated spinning and washing techniques used in the staining of trypsinized cells results in the loss of large number of cells (up to an order of magnitude), thus posing problems for downstream analysis and generation of statistical significance. Several techniques for effective removal of fixed cells from substrates were explored – ranging from the use of higher concentrations of trypsin EDTA (10× or 2.5% trypsin EDTA), the use of versene and other enzymes for long periods of time (up to 30 minutes). The use of these different enzymatic agents was highly variable, fixed cells would sometimes be removed by a 15 minute, 10X trypsinization but in some cases a large fraction would still remain (not shown). Similar results were observed with other enzymatic release agents (such as versene and Accumax). This could possibly be due to the variability in the degree to which cells were fixed, resulting in variability in the ability of the cells to be removed from the substrate. Due to the inability to reliably get the cells off the substrate after fixation, this technique of performing kinase assays on small populations of adhered cells was abandoned.

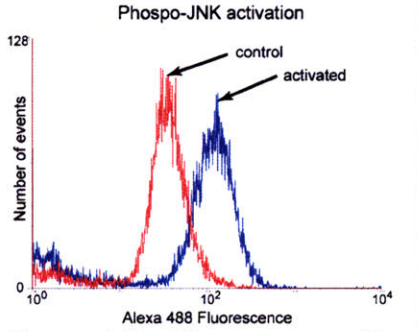

Figure 4-8: Kinase assay. The detection of phosphorylation of JNK using flow cytometry, showing an ~5X increase in phosphorylation in response to stressful events.

Cell migration. The assays explored in this chapter were successfully completed for the macroscale platform but were significantly more challenging to interpret for the microscale, IDE-based platform. A significant contributor to this discrepancy was the movement of cells after they had been patterned between the electrodes. Hence, prior to electric field-based stimulation individual cells were experiencing different electric field intensities. Additionally, cells tend to align themselves along the edges of the electrodes resulting in some cells residing at the

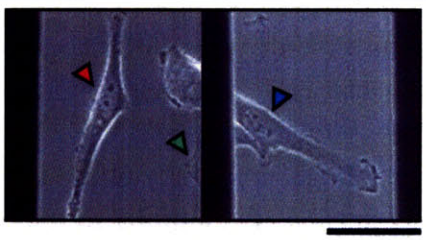

Figure 4-9: Cells on electrodes. Phase microscopy image of a cell ideally situated between the electrodes (red arrowhead), aligned along the electrode (green arrowhead) and straddling an electrode (blue arrowhead). Scale bar 60 μm.

electrode interface. Cells that straddled the electrodes posed challenges in imaging as they exhibited non-uniformity in fluorescence intensity (regions of cells residing on the gold electrode have higher fluorescence intensity due to the high reflectivity of the gold surface [146]). A representative image of cells that have migrated across electrode structures is shown in Figure 4-9. Two techniques were explored to try to mitigate this migratory effect – (1) alter the surface chemistry of the gold surface using thiolated-polyethylene glycol polymers (PEG-thiols) to make the gold a less desirable surface for the cells to attach to, and (2) the use of polystyrene patterning techniques to build islands of polystyrene on top of the glass surface between the electrodes. The PEG-thiols were partially successful in preventing adhesion of cells to the gold electrodes (see Supplementary Information section). The main obstacle in optimizing the protocol was the requirement of highly pure gold for the thiol groups to self-assemble. As my electrode devices were fabricated in an evaporation chamber used for deposition of other materials, trace impurities in the gold were significant enough to affect the outcome of the assay. The polystyrene patterning technique was challenging to reliably replicate for such small electrode gaps (~100 μm) resulting in polystyrene patterns bleeding over and covering the electrodes themselves (see Supplementary Information section). The possibility of patterning polystyrene structures did seem promising and served as a proof-of-concept experiment that could later be applied to the design of microfluidic devices for perfusion culture.

4.10 DISCUSSION

The results obtained in this work using IDE arrays as platforms for trapping and then stimulating cells point for the need for enhanced control of the cells and the need to prevent cells from moving away from the electrode regions and polarizing along the walls of the electrodes. This discussion section presents some approaches to overcome these limitations and also the components of a system that could overcome such limitations.

Need for multiplexed system. The IDE-based system poses several challenges for scaling up the assays and for performing multiple assays on one chip. The overhead of first patterning the cells requires the need for individually-addressed banks of electrodes. Such electrode sites would require increasing real-estate on a chip and in the current configuration, 4 individual electrode sites can be fit into the area of approximately a standard glass microscope slide (25 mm × 75 mm). More efficient packing would likely yield at the most 6 individual electrode banks. Given the voltage, frequency and duration maps that would be of interest to map, a system that can perform 12-16 multiplexed experiments would be more desirable, thereby cutting down the number of experiments performed by a factor of 2.

Live-cell assays. The need to perform molecular-level assays to assess subtle changes in gene expression and therefore overall cell physiological state require significant "processing" of the cells. This could involve extraction of nucleic acids or staining of intracellular proteins. All of

these molecular biology techniques require access to the cells, either through fluidic channels or with pipettes. This requires additional complexity, especially in the case of building more multiplexed systems where collection of samples from each electrode-bank could prove to be the rate-limiting step. Microfluidic access would further complicate the system and result in the need for more chip interfaces for the flushing of cell lysing agents and buffers, and collection reservoirs for cell lysates. The process of harvesting cells from the IDE chips is both tedious and time consuming. Performing assays over a large number of conditions could prohibitively time consuming as cells would have to be fixed/stained or have their RNA extracted for downstream molecular biology assays. This points to the need constructing an assay using live cells which could "report" their physiological state. If such reporters are indeed quantifiable (as I will show in Chapter 5) then a live-cell-based assay would obviate the need for such system complexity in "processing" cells and allow for the design of endpoint assays without the need for fixing/lysing cells.

Need for automation. The IDE-based approach, while viable, is not especially amenable to automation, particularly from the aspect of the biological assays. These assays would all have to be processed by hand. It could be argued that these molecular biology assays could be performed on chip, as has been previously demonstrated [147] but this requires considerable engineering complexity. The use of live-cell-based assays can free up these restrictions and enable a system that is more amenable to automation.

Based on the points discussed above, a new system was designed to incorporate these new features, this new system along with results obtained with it are discussed in the following chapter (Chapter 5).

4.11 CONCLUSIONS

The results and discussion presented in this chapter delineate the complexity of testing the hypotheses presented, both from the standpoint of engineering systems to efficiently address these hypotheses and the biological assays required to perform robust readouts for each experimental condition. To address this complexity, a two-pronged effort of engineering a microfabricated platform capable of performing multiplexed experiments and developing a robust gene-expression assay as an efficient means of biological readout must be undertaken. The following chapter presents the design, fabrication and implementation of this system and the development of a live-cell biological sensor. Results obtained with this new platform will also be presented and their implications for the biological and engineering communities will also be presented.

4.12 MATERIALS & METHODS

Cell culture. Murine fibroblast (NIH 3T3) cell lines were obtained from the ATCC. NIH 3T3 cells were cultured using standard media formulations and culture techniques. Briefly, NIH 3T3 cells were grown in DMEM culture media supplemented with 10 % (v/v) bovine calf serum, 1% (v/v) L-glutamine, and 2% (v/v) penicillin-streptomycin. Cells were split every 2-3 days using 0.25% trypsin EDTA and re-seeded at 1:10 split ratios.

Cellular stress assays. Cellular stress assays were performed using either standard heat shock protocols [112] which employed elevated temperatures of up to 45 °C or using chemical stressors such as sodium arsenite. In the case of heat shock, positive control experiments were performed with cells seeded in flaskettes at a cell-seeding density of 10,000 cells/ml. Twenty-four hours after seeding (giving the cells ample time for attachment and spreading) cells were ready for stress assays. Flaskettes containing cells were placed on a hot plate at 42.5 °C for 30 minutes. Real-time temperature monitoring was performed with a control flaskette with a thermocouple attached to the cell culture surface (an equal volume of media was placed in this flaskette as the flaskette containing cells, and similarly it was allowed to equilibrate in the incubator for the same amount of time). Stressed cells were then placed in the incubator and assayed after 12-14 hours. In the case of chemical stressors, sodium (meta)arsenite (71827, Sigma Aldrich) was dissolved in cell culture media (under aseptic conditions) to a final concentration of 100-250 μg/ml. This "stressing" media was then added to the cells by first aspirating the original media and performing a wash with PBS. The "stressing" media was left on the cells for 30 minutes (at 37 °C) and then aspirated, with 2× PBS washes to ensure trace stressors were removed. Similar to heat shock techniques, cells were assayed 12-14 hours after incubation at 37 °C.

Interdigitated electrode (IDE) fabrication. Interdigitated electrodes were fabricated using standard gold lift-off techniques. Six-inch pyrex wafers were first cleaned in a piranha solution for 10 minutes. The wafers were subsequently dump-rinsed and then dried using a spin-rinse-dryer. Dehydration bakes for 30 min were performed in a vacuum oven at 150 °C. The wafers were then coated in NR-7 negative tone lift-off resist (NR-7-3000P, Futurrex, Inc.) using static dispense techniques, 750 rpm (5 second) spread, and 1500 rpm (35 second) spin. Wafers were then soft-baked at 100 °C on hot plates (with care being taken to read the actual plate temperatures using a thermocouple) for 15 minutes. The wafers were then exposed with i-line UV exposure (10 mJ/cm^2) for 5 seconds using a mask alignment tool (EV620, Electronic Visions). The wafers were then post-baked at 150 °C for 15 minutes (again, with careful attention to the actual plate temperature measurement). Wafers were subsequently developed in custom developer solution (RD6, Futurrex, Inc.) and then triple-rinsed in DI water. Wafers were then loaded in an electron beam deposition system for coating with 10 nm of titanium and 100 nm of gold (using pre-determined recipes). Gold-coated wafers were then placed in a resist remover solution (RR4, Futurrex, Inc.) overnight to lift-off the NR7 resist. Stringers and extraneous metal film were removed by rinsing in DI water. Wafers were subsequently coated with thick positive photoresist (AZ4620) to a thickness of ~10 micron and then baked at 65°C for 30

minutes. Resist-coated wafers were subsequently die-sawed into individual chips using a diamond saw (Disco die-saw). This photoresist coat was removed with an acetone and isopropanol rinse prior to performing any cell-based assays.

Immunofluorescence assays. Cells seeded on flaskettes were fixed in 3.7 % paraformaldehdye for 15 minutes. Fixed cells were then permeabilized for 10 minutes using 0.1% Triton X-100. Cells were then triple rinsed in PBS and incubated with the first blocking buffer solution (BB1, see Supplementary Information). The HSC70 translocation assays and the kinase assays had slightly different protocols. For the HSC70 translocation assays, the primary antibody, anti-HSC70 (SPA 815, Stressgen) at a concentration of 1:100 (v/v) in BB1 was incubated for 30 minutes. After rinsing 3× with PBS, the secondary antibody, Cy3 conjugated, donkey anti-mouse (715-165-150, Jackson ImmunoResearch Laboratories) at 1:200 (v/v), Hoecsht bisbenzimide (33258, Invitrogen) at 1:10,000 and Alexa-488 conjugated phalloidin (A12379, Invitrogen) at 1:100 (v/v) were added in the second blocking buffer BB2 (See Supplementary Information for composition) and incubated for 1 hour. For the kinase assays, the primary antibody, anti-phospho-SAPK (9251, Cell Signaling Technology) at a concentration of 1:25 (v/v) in BB1 was incubated for 30 minutes. After rinsing 3× with PBS, the secondary antibody, Cy3 conjugated, donkey anti-mouse (715-165-150, Jackson ImmunoResearch Laboratories) at 1:200 (v/v), was added in the second blocking buffer BB2 and incubated for 1 hour. The next steps were the same for both translocation and kinase assays. After another 3× rinse in PBS, excess PBS was carefully removed and the slides were subsequently mounted in mounting medium (Fluoromont G, Invitrogen) and a coverslip was carefully placed over the slide as the final seal. Fixed, stained, and mounted slides were subsequently labeled and stored at 4 °C prior to imaging.

Flow Cytometry (FACS). Cells for flow cytometry were fixed and stained as described above in the immunofluorescence methods section described above, with the main difference being that all the above steps were performed in suspension. Hence, the cells were first trypsinized for 5 minutes at 37°C (0.25% Trypsin EDTA, Invitrogen) and harvested prior to fixing and staining. Similarly, all wash steps were performed by spinning cells down at 1000 rpm for 5 minutes. Fixed and stained cells were then spun down and resuspended in 1 ml of PBS and loaded in a flow cytometer (FACScan, BD Biosciences). Gating, detector gains, side-scatter (SSC) and forward scatter (FSC) were all set according to negative controls. These setup parameters were saved in the template file and used for subsequent experiments.

Fluorescence Microscopy and Image Cytometry. Fixed, stained and mounted cells were imaged using fluorescence microscopy. Slides were placed on an upright microscope (AxioImager M1m, Carl Zeiss, Inc.) stage and imaged in epifluorescence mode using a liquid-lightguide-coupled excitation source (XCite 100, EXFO Life Science Inc.). Images of nuclei (stained with Hoechst), cytosol (stained with Alexa-488-conjugated phalloidin) and HSP70/HSC70/TIA-1 (stained with corresponding primary antibody and Cy3-coupled secondary antibody) were imaged using DAPI (31000, Chroma Technology), FITC (41001, Chroma Technology) and Cy3 (41007a, Chroma

Technology) fluorescence filter sets respectively. Images were captured using a 12-bit cooled camera (Imager QE, f : Fision, Inc.). Care was taken to ensure that control and experimental images were taken with identical exposure times. Images were then post-processed in MATLAB using custom-designed algorithms (MATLAB code is enclosed in the Supplementary Information section). Average background intensity was determined from the images from the use of five 10 x 10 pixel regions-of-interest (ROIs). The average value of the 5 ROIs was used to compute the background and subsequently used to correct for each image on a per image basis. Field illumination corrections were deemed to be unnecessary after imaging a blank region of the slide and comparing fluorescence intensities in all channels to a "dark image" i.e. an image taken with the shutter closed and no light incident on the CCD (variations in the intensity across the image were comparable to the noise floor of the camera). Briefly, fluorescence images of the nucleus and cytosol were thresholded using a global threshold algorithm, utilizing Otsu's method [148]. This thresholding algorithm is used to determine an effective threshold value per image and used to generate masks of the unique nuclear and cytosolic regions in each image. These masks were then used to mask the intensity in the nucleus and cytosol of the protein of interest. Figure 4-6 illustrates this technique. Ratios of the intensity in the nucleus and cytoplasm were then plotted as a histogram to illustrate the shuttling of the protein between the nucleus and cytosol (as shown in Figure 4-6C).

Reserve-Transcription Polymerase Chain Reaction (RT-PCR). Cells for gene expression analysis were first harvested using trypsinization and spun down and washed in PBS to generate a cell pellet. RNA extraction was performed using a standard RNA extraction protocol (RNEasy Mini Kit, Qiagen, Inc.). Briefly, cells were first destabilized using Buffer RLT and lysed using the QIAShredder spin column. Lysate was then subsequently spun through a QIAcolumn and the RNA was isolated. The final RNA was eluted using RNAse free water (Ambion Biosciences) and the purity of the isolated RNA was examined using a spectrophotometer (ND-1000, NanoDrop Technologies). Total RNA concentration and 260/280 metrics were recorded. Detailed protocols are described in the Supplementary Information section. Purified RNA was stored at -20°C prior to PCR experiments. Reverse transcription of the RNA to complementary DNA (cDNA) was performed in a one-step kit (Invitrogen, Inc.) using a hot-start Taq polymerase. PCR was performed in capped strip-well tubes with 1 μg of starting RNA template and 50 μl of total volume. Primers were chosen to be 20-mers and designed using Primer 3.0 (Whitehead Institute) and verified using BLAST. Details of primers used for HSP70, GAPDH and 18S are included in the Supplementary Information section. Final PCR product sizes were chosen to be slightly different (specifically, 360 bp for HSP70 and 238 bp for GAPDH) to allow for sufficient spatial separation during gel electrophoresis. PCR protocols were programmed on a thermocycler (MJ Research, Inc.) and performed for 25 cycles. Detailed PCR protocols can be found in the Supplementary Information section. After completion of the PCR, DNA products were stored at -20°C prior to analysis using gel electrophoresis. Gel electrophoresis was performed on pre-cast gels (E-Gel, Invitrogen, Inc.). ranging from 1% to 5% agarose concentrations. PCR samples were mixed with loading dye (1X BlueJuice, Invitogen) to

facilitate tracking in the gels and subsequently loaded with gel-loading pipette tips to prevent bubbles at inlet reservoirs. Commercially available DNA ladders (10380-012, Ready-Load 100 bp ladder, Invitrogen) were loaded at either ends to serve as markers for imaging. Pre-cast gels were run on the associated controller (E-Gel controller, Invitrogen) for 30 minutes. Upon completion of electrophoresis the gels were imaged on a gel documentation system (Ingenius 12, Syngene Corporation) using ultraviolet transillumination. Images were captured with a 12-bit digital camera (QImaging, Inc.).

Dielectrophoretic trapping and stimulation. Chips were stripped of protective photoresist using acetone and subsequently rinsed with isopropanol and ethanol. Chips were then mounted on a custom-designed printed circuit board with electrical connections made between the PCB and chip using 16-gauge wire and conductive silver epoxy (CW#2400, Circuit Works). The PCB was then mounted on the microscope stage. Custom channels were laser-cut from PDMS sheets (HT-PDMS, Bisco Silicones) and were used to form the fluidic channel. The native silicone seal was used to adhere them to the chip surface obviating the need for epoxies or sealants (which may adversely impact cell health themselves). Cell suspensions were then pipetted directly onto the chip and sealed with a glass coverslip. Electrical waveforms were supplied using an arbitrary waveform generator (Agilent Technologies) connected to the PCB using alligator clips. A trapping waveform of 2.5Vp-p at 10 MHz was used to align the cells. The cells were then allowed to settle between the electrodes, with occasional voltage pulses to keep them away from the electrodes. Once the cells had settled between the electrodes the entire setup was carefully moved to the incubator. A final voltage pulse was performed to re-align any errant cells and the cells were then allowed to adhere. After approximately 4 hours, a wavefrom identical to the trapping waveform was applied for 15-30 minutes. After another 4 hours cells were removed from the incubator for downstream biological analysis using methods analogous to those described above, except performed on chip. To perform staining and RNA isolation protocols on chip, the IDE chips were unsealed by carefully placing them in a media containing dish and using a pair of sterile tweezers to gently pry the coverslip off the silicone gasket. The silicone gasket was then peeled back and removed. The chips could now be treated as regular glass slides and used analogously for all staining protocols.

4.13 ACKNOWLEDGEMENTS

I would like to thank Keith Tyo for teaching me the fundamentals of RNA extraction and PCR amplification. Luke Whitesell deserves special mention for providing many insights from his considerable knowledge of cellular stress. Jana Koubova, Mark Gill, Kevin King, Greg Underhill and Martin Duennwald provided several helpful and crucial discussions about biological experiments. Also, I would like to thank the Microsystems Technology Laboratories staff for help with microfabrication. Finally, I would like to thank several faculty members for helpful discussions, namely – David Sabatini, Peter Sorger, Al Grodzinsky and Mary Lou Pardue.

4.14 SUPPLEMENTARY INFORMATION

4.14.1 Blocking buffers for immunofluorescence assays

Two distinct blocking buffers for all immunofluorescence and antibody staining protocols, the first buffer (BB1) was used with the primary antibody and the second buffer (BB2) was used with the secondary antibody. The compositions of these buffers are as below,

Blocking Buffer #1 (BB1)
3% (v/v) Bovine serum albumin
3% (v/v) Fetal bovine serum
94% (v/v) Phosphate buffered saline

Blocking Buffer #2 (BB2)
2% (v/v) Bovine serum albumin
2% (v/v) Normal donkey serum (in the case of donkey derived secondary antibodies)[†]
0.1% (v/v) Tween-20
95.9% (v/v) Phosphate buffered saline

[†] For secondary antibodies derived from other animal sources, the appropriate animal serum should be substituted in the same volume-per-volume ratio.

4.14.2 RNA extraction protocol using QIAGen RNeasy kit

The following protocol utilizes buffers provided in the QIAGen RNeasy kit and the only additional supplies required are 2 ml RNAse free centrifuge tubes for sample collection and washing.

1. Trypsinize cells using 0.25% trypsin EDTA for 5 minutes at 37 °C. Quench with media and perform a cell count using a hemocytometer or coulter counter.
2. Spin cells at 1000 rpm for 5 minutes.
3. Aspirate the supernatant and add Buffer RLT to the cell pellet to disrupt the cells. Vortex or pipet thoroughly to mix the buffer and dissociate the pellet.
4. Pipet the lysate directly into a QIAShredder spin column in a 2 ml collection tube and centrifuge for 2 minutes at 14000 rpm.
5. Add 1 volume of 70% ethanol to the homogenized lysate and mix well by pipeting, do not centrifuge.
6. Transfer 700 µl of the sample to an RNeasy spin column placed in a 2 ml collection tube. Centrifuge for 15s at 10,000 rpm. Discard the flow through.
7. Add 700 µl of Buffer RW1 to the same RNeasy spin column and centrifuge for 15s at 10,000 rpm. Again, discard the flow through.
8. Add 500 µl of Buffer RPE to the same RNeasy spin column and centrifuge for 15s at 10,000 rpm. Again, discard the flow through.
9. Add 500 µl of Buffer RPE to the same RNeasy spin column and centrifuge for 2 minutes at 10,000 rpm. Again, discard the flow through.
10. To prevent buffer carryover, place the RNeasy spin column in a new 2 ml collection tube and centrifuge at 14,000 rpm for 1 minute. Discard the tube and flow through.

11. Place the RNeasy spin column in a new 1.5 ml collection tube. Carefully pipet 50 µl (or as little as 30 µl) of RNase free water on to the RNeasy spin column and centrifuge for 1 minute at 10,000 rpm to elute the RNA.

4.14.3 Primers for PCR

Forward and reverse primers for HSP70, GAPDH and 18S are listed below. The estimated size of the amplicons are 360 bp (HSP70), 238 bp (GAPDH) and 220 bp (18S). Amplicon sizes were verified by gel electrophoresis and comparison to a standard DNA ladder as shown in Figure 4-10.

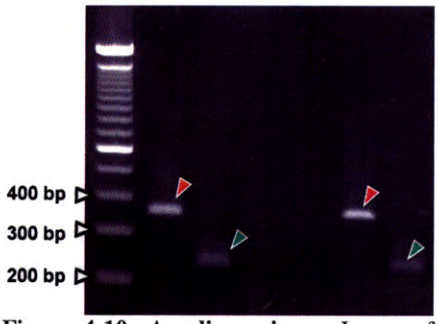

Figure 4-10: Amplicon sizes. Image of agarose gel using UV-transillumination. Leftmost lane shows DNA ladder with 100 bp separation. HSP70 products (red arrowheads) are 360 bp and are situated between the 400 bp and 300 bp ladder markers. Similarly, GAPDH products (green arrowheads) at 238 bp are between

HSP70 forward – TGT TCC GTT TCC AGC CCC CCA
HSP70 reverse– GGG CTT GTC TCC GTC GTT GAT

GAPDH forward – GAG TCA ACG GAT TTG GTC GT
GAPDH reverse – TTG ATT TTG GAG GGA TCT CG

18S forward – CGT CTG CCC TAT CAA CTT TCG
18S reverse – TGC CTT CCT TGG ATG TGG TAG

4.14.4 Protocols for PCR

The Superscript One-Step RT-PCR with Platinum Taq was used for all the PCRs described in this chapter. This kit combines components for both complementary DNA (cDNA) synthesis and PCR. The reaction mixes were thawed on wet ice to 4 °C. The primers were dissolved in nuclease-free water and diluted to a concentration of 10 µM. A nuclease-free work space was created by spraying down the benchtop and gloves with RNAse Zap (Ambion Biosciences). All pipettors were wiped down with RNAse Zap and all pipette tips used were nuclease-free (as per manufacturers' certifications). Below are the recipes for reaction cocktails and thermocycling protocols. Reaction cocktails were prepared and maintained on wet ice until placing them in a thermocycler for reverse transcription immediately followed by PCR.

Reaction cocktails	
2× reaction mix	25 µl
Template RNA	*X* µl (1 µg)
Sense primer (10 µM)	1 µl
Antisense primer (10µM)	1 µl
RT/Platinum Taq mix	1 µl
Autoclaved distilled water to	50 µl

Where *X* is determined from the concentration obtained after RNA extraction (which in my experience can vary over a factor of 5 across samples).

The specific thermal cycling protocol used was,

Step A: cDNA synthesis and denaturation
1 cycle of: 50 °C for 20 min
94 °C for 2 min

Step B: PCR amplification
25 cycles of: Denature at 94 °C for 15 seconds
Anneal at 55 °C for 30 seconds
Extend at 70 °C for 1 min

These steps were determined from general guidelines in the protocol provided with the kit. It is important to note that optimal temperatures for reverse transcription will depend on primer and target sequences, so the above parameters may not be optimal for arbitrary primer lengths and target genes.

4.14.5 Image processing algorithm for image cytometry

MATLAB script for masking specific regions of cells that have been fluorescently labeled.

```
%Salil Desai (desai@mit.edu)
%script for masking and processing different regions of the cell
%specifically the nucleus and the cytosol
%created: 01/05/2005

clear all;
close all;

%load images
c_1_1tt = imread('desai-HeLa-set2-HS60m-cy3-15ms.TIFF');     %image of
interest
d_1_1tt = imread('desai-HeLa-set2-HS60m-dapi-35ms.TIFF');    %used for the
nuclear mask
p_1_1tt = imread('desai-HeLa-set2-HS60m-phall-250ms.TIFF');   %used for the
cytosol mask

%convert rgb images to grayscale
p_1_1t = rgb2gray(p_1_1tt);
d_1_1t = rgb2gray(d_1_1tt);
c_1_1t = rgb2gray(c_1_1tt);

colorim = zeros(size(p_1_1tt,1), size(p_1_1tt,2),3);
colornuc = zeros(size(p_1_1tt,1), size(p_1_1tt,2),3);
colorcyto = zeros(size(p_1_1tt,1), size(p_1_1tt,2),3);

%convert to intensity image, using 0 and 4095 as MIN and MAX intensities
%respectively (since the starting images were 12 bit)
PHAL_1_1 = mat2gray(double(p_1_1t), [0 4095]);
DAPI_1_1 = mat2gray(double(d_1_1t), [0 4095]);
CY3_1_1 = mat2gray(double(c_1_1t), [0 4095]);

colorim(:,:,1) = CY3_1_1;
```

```
%determine threshold levels for the masking images
D_1_1level = graythresh(DAPI_1_1);
P_1_1level = graythresh(PHAL_1_1);

%threshold masking images to create binary mask
DAPI_1_1t = im2bw(DAPI_1_1,D_1_1level);
PHAL_1_1t = im2bw(PHAL_1_1,P_1_1level);

%fill in any holes in the mask
DAPI_1_1bw = imfill(DAPI_1_1t,'holes');
PHAL_1_1bw = imfill(PHAL_1_1t,'holes');

CYTO_1_1bw = PHAL_1_1bw - DAPI_1_1bw;

%apply masks
CY3_nuclear = CY3_1_1 .* DAPI_1_1bw;
CY3_cytosol = CY3_1_1 .* CYTO_1_1bw;

colornuc(:,:,1) = CY3_nuclear;
colorcyto(:,:,1) = CY3_cytosol;

%determine fluorescent intensity in each masked area
nuclear_intensity = sum(sum(CY3_nuclear));
cytosol_intensity = sum(sum(CY3_cytosol));

%determine area covered by each mask
nuclear_area = sum(sum(DAPI_1_1bw));
cytosol_area = sum(sum(CYTO_1_1bw));

fcr = (cytosol_intensity/cytosol_area)
fnr = (nuclear_intensity/nuclear_area)

figure(1), imshow(colorim);
figure(2), imshow(colornuc);
figure(3), imshow(colorcyto);
```

4.14.6 PEG-thiol methods and results

PEG-thiol is a linear chain molecule capable of assembling into a densely packed monolayer on a gold substrate via its thiol residue. The extended PEG brush inhibits the binding of proteins and thereby prevents cell attachment. To prevent the cell attachment to the electrodes, the adsorption of PEG-thiols to the electrodes was performed using a previously published protocol [149]. Briefly, PEG-thiols (PLS-604, Creative PEG-Works), were dissolved to a concentration of 2 mM in ethanol. IDE chips were first cleaned in 2× Nanostrip (Cyantek Corporation) and then 3× rinsed in DI water. Chips were subsequently soaked for 2 hrs in the ethanolic solution. The chips were subsequently removed,

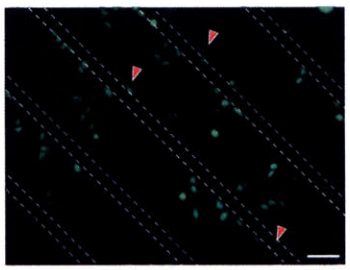

Figure 4-11: PEG-thiols. Fluorescence microscopy image of cells seeded on PEG-thiol functionalized electrodes, showing some cells (red arrowheads) adhered to electrodes (dashed white lines). Scale bar 50 μm.

rinsed 2× in ethanol and dried under a nitrogen stream. The chips were then immediately placed in a bio-cabinet and seeded with NIH 3T3 cells (at ~10,000 cells/ml seeding density). Chips were then placed in an incubator and subsequently imaged after ~12 hrs of culture. A representative image is shown in Figure 4-11, where cells are excluded from the electrodes (excepting a few outliers). These results were challenging to replicate and were not reproducible across the chip. This suggests that either the PEG-thiol had not effectively adsorbed to the surface and is not particularly stable under my culture conditions. Most likely, the fact that the gold substrates used to fabricate these chips have trace contaminants (for example, copper and chrome) could result in the improper adsorption of these films, as proper adsorption requires gold films on the order of 99.990 to 99.999% purity [150]. To further optimize this process, a dedicated evaporator for titanium and gold would have to be used to for deposition. Such a system would have to be found within another user facility or at a collaborating lab, further complicating the fabrication of these devices. Moreover, the investigation of the adsorption of these monolayers would require the use of surface plasmon resonance [149] techniques which would again require access to specialized equipment that would need to incorporate my custom-designed chips. For the aforementioned reasons, the optimization of these techniques was not further investigated.

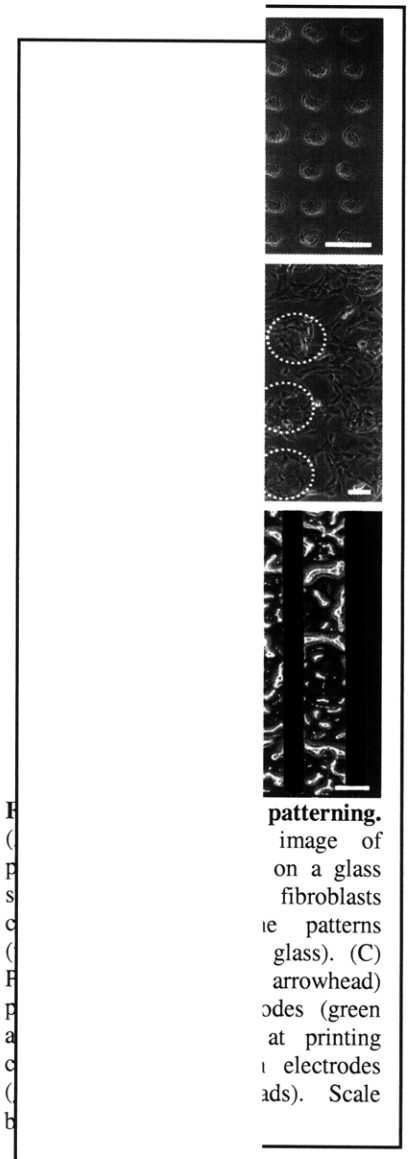

patterning. image of on a glass fibroblasts ıe patterns glass). (C) arrowhead) ɔdes (green at printing ı electrodes ıds). Scale

4.14.7 Polystyrene patterning methods and results

Commercially available polystyrene pellets were dissolved in toluene at a concentration of 10 mg/ml. This polystyrene solution was then loaded in to a thermal inkjet printing system (as detailed §3.7.4) outfitted with a CCD camera for alignment. Test patterns were ink-jetted on to a glass substrate and are shown in Figure 4-12A. These patterns were then gently rinsed with 70% ethanol solution and subsequently placed under UV-illumination for sterilization purposes. The polystyrene-patterned glass substrate was moved to a standard tissue culture dish and seeded with an NIH-3T3 cell suspension. The dish was then placed in a tissue culture incubator to allow for attachment and proliferation of cells. Phase microscopy images (shown in Figure 4-12B) taken ~18 hours after seeding show that the cells adhered to the patches and exhibited morphologies comparable to those seen on standard tissue culture substrates (and in the case of 3T3s even glass substrates). To replicate this patterning strategy on the electrodes, polystyrene spots were jetted between the electrodes, but in a bid to cover more area between the electrodes larger volumes were jetted. This resulted in loss of control of the film thickness with crinkled features (see

Figure 4-12C). The large parameter space than can be explored with such an automated printing technique suggests that this printing process could be optimized, however, as the formation of the film is from discrete drops, it could prove to be challenging to create a smooth film. This idea of polystyrene patterning and the initial results with cell attachment and proliferation seemed very promising to me. As the inkjet printing technique seemed very challenging, I collaborated with Katarina Blagovic to develop a new polystyrene patterning technique using elastomeric stencils [151]. The methods and results of this technique are presented elsewhere, but they present the first steps towards a robust technique that could equally be applied to patterning of polystyrene between electrode structures. As the elastomeric stencils used in this patterning process are transparent they can be readily aligned to electrode structures across the length scales of typical chips used in this study (~ 5 cm x 2 cm).

Chapter 5 – **Live-cell based metrology tools**

Electric fields are widely used in the manipulation, patterning and sorting of live cells. In techniques such as electric-field based fusion cells are first aligned between electrodes and subsequently fused. To pattern live cells, a technique that leverages spatially non-uniform electric fields is used to position cells in specific locations with the help of micropatterned electrodes. This technique is referred to as dielectrophoresis and it has been described in detail in the previous chapter. Dielectrophoresis is also used for the sorting of live cells, where cells are first trapped by pulling them towards electrodes using pDEP [108] or pushing them between electrodes using nDEP [14]. The desired cells are identified via microscopy and are released from traps by turning off the electrodes. This ability to modulate electric fields to manipulate cells has important implications in biotechnology in the identification and purification of useful cell types and in fundamental biology in the isolation and study of rare cells.

5.1 INTRODUCTION

While electric fields have been widely used in the manipulation of live cells there has been comparatively less work in understanding the impact of electric fields on cellular physiology. The overarching goal of this work can be summarized as in Figure 5-1. A normal, healthy, proliferating cell is placed in a high frequency (on the order of MHz) electric field for a short duration (on the order of minutes) and I would like to determine the final state of this electrically "perturbed" cell and more general to perform electrical "screens" to discern electric field effects on cells. Based on the hypothesis outlined in detail in Chapter 4, there could be gross changes in cellular physiology manifested in changes in morphology and rates of proliferation or there could be more subtle changes at the level of signal transduction pathways or gene expression. Previous work as described in Chapter 4 (Section 4.5) has primarily focused on gross physiological assays. My aim is to build on this previous work by performing gene-expression-based assays across a wide range of electric field conditions. Further, these electric field conditions will be chosen so as to mimic those that are typically used in dielectrophoresis-based trapping experiments.

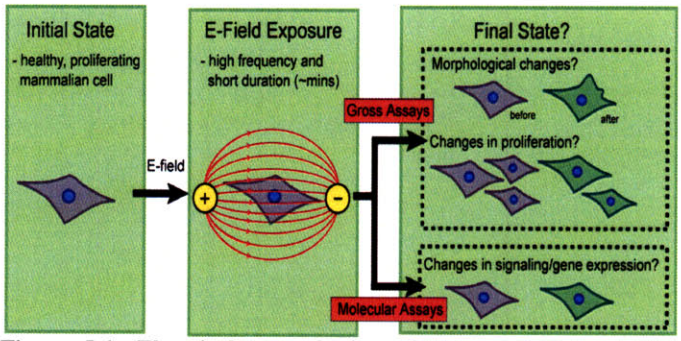

Figure 5-1: Electrical perturbation of cells. A normal, healthy proliferating cell is placed in an electric field and my goal is to determine the nature of this electrical perturbation of the cells. Gross assays can probe morphological changes in the cells whereas molecular level assays can probe more subtle changes in signaling pathways and gene expression.

To achieve this aim of performing an electrical screen there is a need for both a platform and assay with a robust readout and a minimal requirement for the processing of cells to perform molecular assays. To this end I have designed and engineered a microscale platform capable of exposing cells to 16-distinct electrical waveforms. Additionally, to enable facile readout of the assay I developed a reporter cell line that consists of a heat-shock protein promoter that drives GFP expression. This cell line enables an automated microscopy technique for gene expression quantification without the need for processing cells for genetic material (and subsequent molecular biological analysis). The stress responsive pathways in the cells were expounded in detail in the previous chapter and are largely mediated by the heat shock proteins. The specific pathway I chose to focus was the HSP70 pathway due to the robust expression and upregulation of HSP70 in response to stress. Importantly, the HSP70 has been well characterized and is highly conserved across organisms. The HSP70 pathway is tightly regulated with the heat-shock cognate protein HSC70 [110] and the transcription factor HSF-1 [152]. The binding of HSF-1 to the heat shock element (HSE) consensus sequence initiates transcription, thus knockdown of HSF-1 presents a specific target for testing the integrity of the pathway (and is further explored as a internal consistency check using RNA interference techniques later in this chapter). The pathway is schematically depicted in Figure 5-2. By using a plasmid construct with a HSP70 promoter cloned upstream of an EGFP gene I was able to construct a cell line for monitoring HSP70 (and therefore stress levels) using GFP expression levels from single cells.

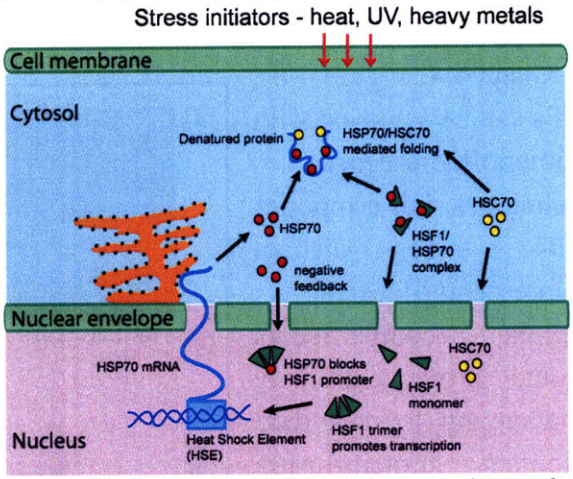

Figure 5-2: HSP70 pathway. Stress activates the dissociation of the HSF1-HSP70 complex, and the HSF1 monomer shuttles to the nucleus. The HSF1 trimerizes and then initiates transcription of HSP70 by binding to the heat shock element (HSE) consensus sequence. HSP70 mRNA is then translated to HSP70 protein and begins its process of mediating folding misfolded proteins. HSP70 and HSC70 also act in concert as self-regulators and are involved in blocking the trimerization of HSF1 and consequently inhibiting expression.

Indeed, heat shock reporters leveraging the HSP70 pathway have been previously explored. Zeng *et al.* [153] developed a HSP70-GFP fusion construct for studying HSP70 shuttling and accumulation in the nucleus of HeLa cells. These cells were constructed using plasmids with the HSP70 promoter and gene (after Rajapandi *et al.* [154]) cloned in to commercially-available pEGFP-C3 plasmids (obtained from Clontech). This generated a C-terminal-EGFP-HSP70 fusion construct which enabled the study of protein translocation in live cells using dynamic fluorescence microscopy techniques such as fluorescence recovery after photobleaching (FRAP). Mitra *et al.* [155] used a rat HSP70 promoter fragment (950 bp in length) to drive GFP expression in mouse mammary EMT6 cell lines. These cells were used to study the activation of heat shock proteins during photodynamic therapy (using meso-tetrahydroxyphenyl chlorin) both *in vitro* and *in vivo*. Molina *et al.* [156] developed a stable transformed fish (EPC — Epithelioma

Papulosum Cyprini) cell line containing a reporter gene under the control of the tilapia HSP70 promoter. Expression of the reporter gene, coding for a green fluorescent protein (GFP)-luciferase fusion protein, was assessed by measuring the luciferase enzymatic activity by chemiluminescence and the GFP expression by fluorescence microscopy and flow cytometry. This cell was developed to study the impact of chemical contaminants on aquatic organism physiology. Taken together, these previously constructed cell lines present important implications for the use of transcriptional reporters using HSP70. Moreover, these reporters have been constructed across a variety of cell types and experimental conditions, pointing to their applicability across multiple organisms. Transcriptional reporters also provide robust gene expression readout using fluorescence microscopy of flow cytometry techniques and are more desirable to protein-fusion constructs as they are easier to quantify. Protein-fusion constructs (such as those described by Zeng *et al.*) require the use of protein translocation within cellular compartments (as was explored in Chapter 4) which can be more challenging to quantify. While such translocation events are inherently ratiometric (in that, the relative amounts of protein that have translocated from one compartment to the other can be quantified), identifying the location of the protein requires that the cellular compartments be identifiable. This in turn requires that the individual compartments be labeled with spectrally distinct fluorescence markers (as is show in Chapter 4, Figure 4-6). This can be achieved with immunofluorescence techniques, but a reporter with three distinct fluorescently-labeled cellular compartments would prove extremely challenging to construct. Similarly, protein-fusion constructs of signaling intermediaries (such as SAPK) would be even more challenging to quantify as they are only meaningful to analyze in their activated, phosphorylated states. Previous work by Ting *et al.* [157] has involved the construction of genetically-encoded fluorescence resonance energy transfer (FRET). Such techniques are very promising but extremely challenging to construct as they require considerable knowledge of the phoshorylation sites and the structural changes induced by phosphorylation. Moreover, the sites for encoding the FRET pairs need to be well

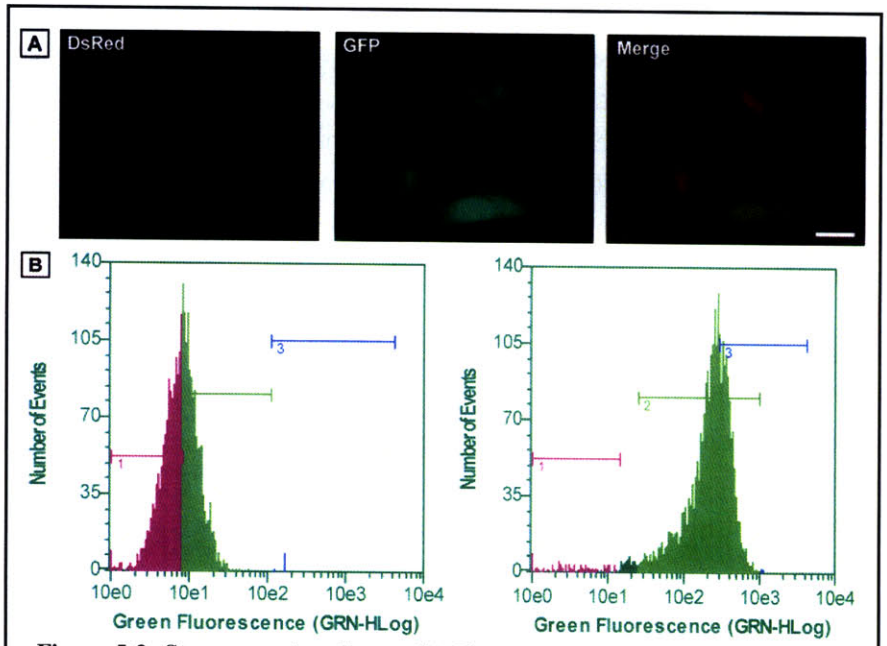

Figure 5-3: Stress reporter clones. (A) Fluoresence microscopy images of single cell clones, showing uniform expression of both DsRed and EGFP. Scale bar 25 μm. (B) Flow cytometry of EGFP expression before (left) and after (right) stress showing a ~50× increase in expression post-stress.

identified and the appropriate fluorescent markers require to be stably integrated. Additionally, specialized filter sets and sensitive detectors would be required to detect these FRET-based events. Taken the together, the complexity of this task would necessitate that the generation of a new, stress-associated kinase reporter be some form of collaborative effort with structural and molecular biologists.

I chose to develop a new cell line, based on three main reasons – (1) the previously cited cell line (Zeng *et al.*) was transiently transfected and had limited applications for my studies, which would require the use of a stable construct, (2) the cell line constructed by Mitra *et al.* was not readily available and was not constructed from plasmids based on open standards, and (3) the cell line constructed by Molina *et al.* was based on a non-mammalian cell type and hence would be less applicable to mammalian cell lines that are of interest to our group. Similarly, the corresponding plasmids used for the transfection were not readily available. One of the main goals of our work is to build a cell line that would be based on well known parental cell line (i.e. NIH 3T3) and would be well characterized so as to be disseminated to both the microsystems and biological communities. Moreover, the cell lines are engineered from plasmids that are based on open standards and can be readily cloned and amplified in any biological laboratory.

5.2 RESULTS

5.2.1 Single cell cloned reporter cell line

The cloned cell line was prepared using co-transfection techniques using an NIH 3T3 parental cell line and characterized using flow cytometry techniques as detailed in the Methods section. Imaging of the cells using fluorescence microscopy indicated uniform expression of both DsRed and EGFP (post exposure to cellular stressing agents) as shown in Figure 5-3A. Importantly, the cell lines showed robust upregulation of HSP70 with a ~ 50× increase in expression as measured using flow cytometry, the narrow distribution and broad distribution between stressed and control populations (Figure 5-3B) indicate that the single cell cloning was successfully accomplished. As an independent assay these cloned populations were assayed for expression of HSP70 via reverse transcription-polymerase chain reaction (RT-PCR). These RT-PCR reactions were performed with exactly the same protocols as described in the previous chapter (see Supplementary Information section). Results from PCR on stressed and control populations show that an increase in GFP expression correlates with an increase in the amount of HSP70 mRNA production (see Figure 5-4). The control band in this figure shows HSP70 expression which is expected given there is constitutive, baseline expression of HSP70.

Figure 5-4: RT-PCR results. Left band (red arrowhead) is the amplification of HSP70 cDNA in the control (unstressed) reporter. Right band shows HSP70 cDNA from the stressed reporter.

5.2.2 Microfabricated platform

The previously explored microfabricated platform (described in Chapter 4) consisted of interdigitated elelctrode arrays. These were deemed to be inadequate as they were difficult to

scale or multiplex to the degree that would be required to fulfill the goals of this thesis. To this end a new platform was conceived and a large part of the motivation for the new platform was to prevent the need for patterning cells. Having removed the requirement of using spatially non-uniform fields for patterning, it was clear that uniform electric fields would be easier to realize. This led to the exploration of a design space that would fulfill the requirements of – (1) ability to realize with routine microfabrication processes, (2) amenable to high-contrast fluorescence micrcscopy, (3) compatible with adherent cells, and (4) capability to multiplex. Based on these criterion it was determined that instead of patterning cells between two planarized electrodes it would be significantly easier to instead have the cells randomly oriented between two parallel plate electrodes. Such a system could be fabricated with transparent top and bottom electrodes to enable imaging and cells could be seeded on the bottom electrode. By patterning the bottom electrode and building discrete wells around each electrode it would be possible to realize individual electrode patches. Taken together, these features enabled the design and construction of the new microfabricated platform. Comparing the difference between the electrode attached cells and suspended cells in an electric field provided insight in to how the coupling of the fields might differ from the idealized case (see Supplementary Information). By modeling the impedance of the parallel-plate configuration, it is possible to determine an optimized cell seeding density to prevent cells from screening the field, providing valuable information as to how the device should be set up prior to an assay.

The assay platform was microfabricated as described in the Methods section. A schematic and microscope image of the device and packaging scheme are shown in Figure 5-5. The device consists of 16 individually addressed electrodes, and each electrode has a corresponding temperature-sensing resistor. Cells seeded in the clamped electrode chamber were able to attach, spread and proliferate (not shown). The transparent indium tin oxide (ITO) enables imaging with both upright and inverted microscopy techniques. Coupled with the automated waveform generation system and automated microscopy readout, assays were readily performed using this platform (see subsequent sections).

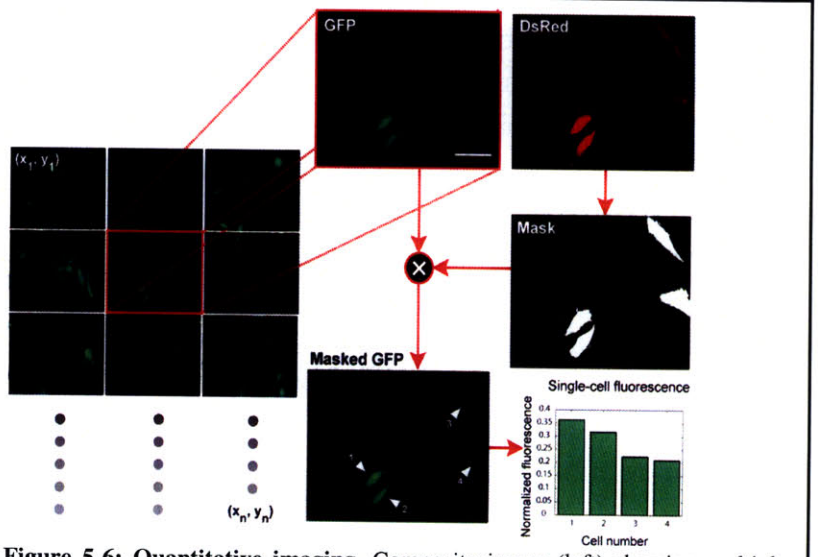

Figure 5-6: Quantitative imaging. Composite image (left) showing multiple scan points from a single electrode. Multi-wavelength fluorescence imaging of each region of the electrode allows using DsRed images to mask the GFP images and extract quantitative information from single cells in the GFP image (right). Scale bar 40 μm.

5.2.3 Image cytometry

The imaging algorithms successfully segment the image and identify single cells. As depicted in

Figure 5-5 it is possible to take a set of dual wavelength images from a two-dimensional scan of the electrode and extract quantitative information of the fluorescence intensity of that cell. Now, by comparing these intensities to the baseline intensity from the control population of cells it is possible to extract a number for the expression level of a particular cell population.

5.2.4 Voltage sweep

Using the automated system for generating waveforms, a series of waveforms at increasing voltages was swept across the electrodes (Figure 5-6A). The average temperature at each electrode site was also measured as an internal consistency check to corroborate the levels of stress. As is expected with increasing temperature levels, I see an increasing amount of stress. The stress level saturates after a certain likely due to the fact that feedback mechanism of HSP70 kicks in to regulate expression. This trend of increasing stress with increasing voltage was observed across different durations of electric field application (as show in Figure 5-6B). Further, this trend across durations indicates that there is a trade-off between applied electric field magnitude and duration, i.e. the same amount of stress can be exacted by a low voltage applied for a long duration as a high voltage for a short duration. This has important implications for designers and users of DEP-based traps in setting an optimal voltage and duration for a given assay.

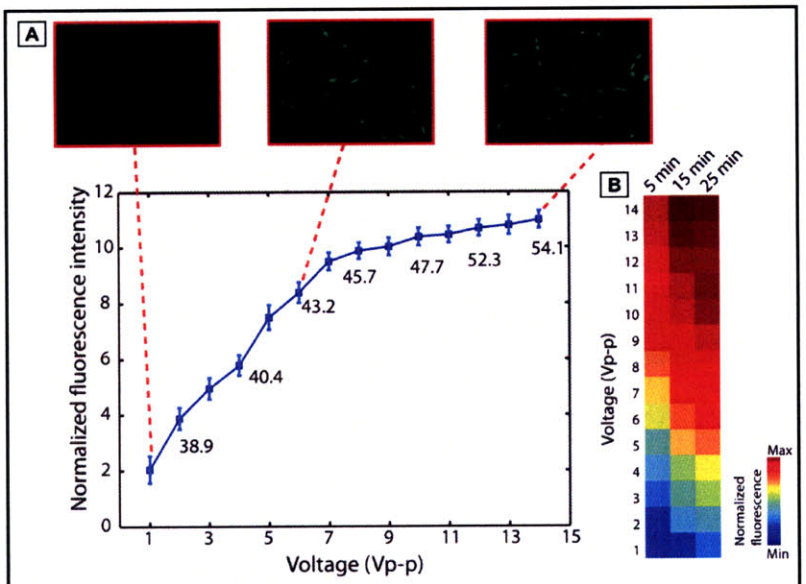

Figure 5-8: Voltage sweep. (A) The voltage sweep along with representative images from select scans shows a dramatic increase in cellular stress with increase in voltage. (B) A heat map showing a voltage sweep for different durations of field exposure. Longer durations of exposure show increased cellular stress levels.

5.2.5 Frequency sweep

Analogous to the voltage sweep, a range of frequencies can be swept across the electrodes and the fluorescence intensity of the cells averaged for each individual electrode. The fluorescence intensities are then normalized to the average intensity of the control electrode. As in the case of the voltage sweep, each assay performed has internal negative and positive controls on

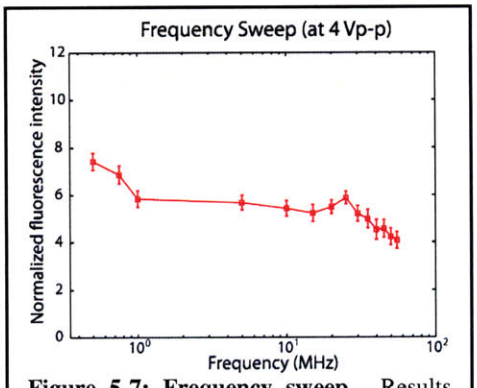

Figure 5-7: Frequency sweep. Results from a frequency sweep performed at 4Vp-p indicating that cells exhibit higher levels of stress at low frequencies (less than ~ 1 MHz) compared to higher frequencies (greater than ~10 MHz).

chip to ensure that comparisons can be made both between electrodes and between experiments. The frequency sweep shows some unexpected trends of higher stress at low frequencies (less than ~ 1 MHz) compared to higher frequencies (greater than ~10 MHz). My hypothesis was that this trend was likely due to higher transmembrane loading at low frequencies, where the majority of the voltage was dropped across the membrane capacitor. To test this hypothesis, assays of membrane depolarization were performed and the results are detailed in § 5.2.6. To test whether this low-frequency trend was repeatable and indeed significant, a number of frequency sweeps were performed at lower frequencies. The results of these assays are summarized in the heat map shown in Figure 5-9.

The consistent pattern of high stress at low frequencies posed an intriguing question as to the mechanisms of the stress reporter cell line. The expected transmembrane potentials suggest that

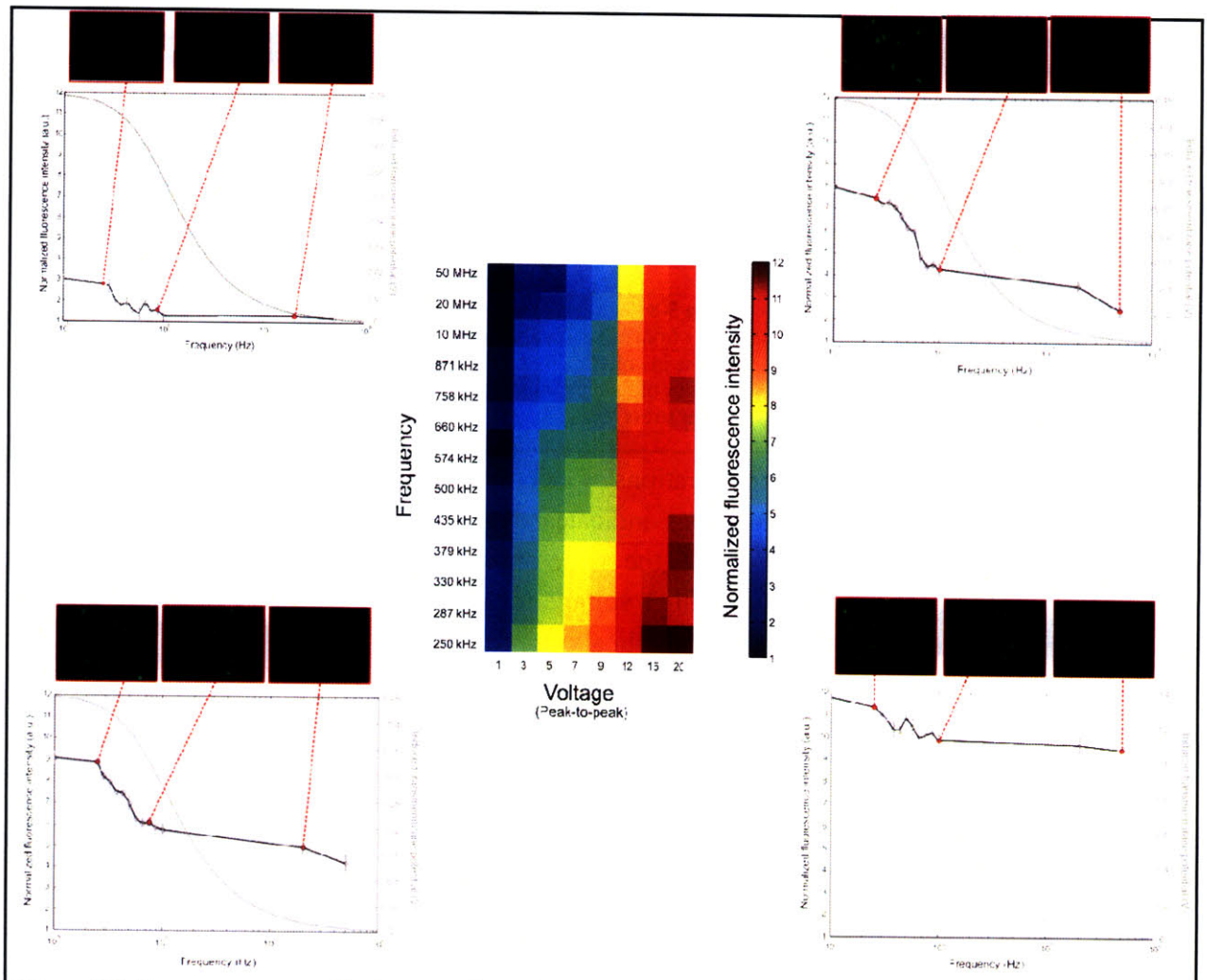

Figure 5-9: Frequency sweeps. The heatmap shows frequency sweeps ranging from 250 kHz to 50 MHz over a range of voltages. Voltage sweeps for 1 Vp-p, 5 Vp-p, 9 Vp-p and 15 Vp-p are shown alongwith three representative images from the sweep. In addition to the images, the voltage sweeps are also overlayed with the expected transmembrane potential.

the cells were being subjected to potentials much higher than the ~ 1 V required to electroporate

the cells. The higher voltage sweeps (15 Vp-p in particular) showed significantly more dead cells than those at lower voltages. In addition to membrane polarization effects, another hypothesis I was interested in exploring was the generation of reactive species in the media that could be coupling with the stress response. The results from assays done to test these hypotheses are described in the subsequent sections (specifically § 5.2.6 and § 5.2.7)

5.2.6 Membrane loading

The effect of transmembrane loading on the stress response was determined by performing a depolarization of the membrane using an H^+ ion analog. Specifically, this ion analog, nigericin, mediates non-electrogenic exchange of H^+ ions for K^+ ions [158]. The buildup of excess H^+ ions in the surrounding medium at the expense of K^+ ions results in the collapse of the membrane potential maintained by the K^+ ion gradient. Nigericin was pulsed on the reporter cells and the stress-response was measured using flow cytometry. The results of the flow cytometry indicate that there was no significant difference between the control and nigericin-stimulated population (Figure 5-9). Care was taken to perform the assay in pH balanced solutions and in a buffer that closely approximated the ionic content of the cytosol. Nigericin concentrations were those previously shown [159] to have a discernible effect on membrane polarization (as measured using fluorescence-based imaging of voltage-sensitive membrane dyes).

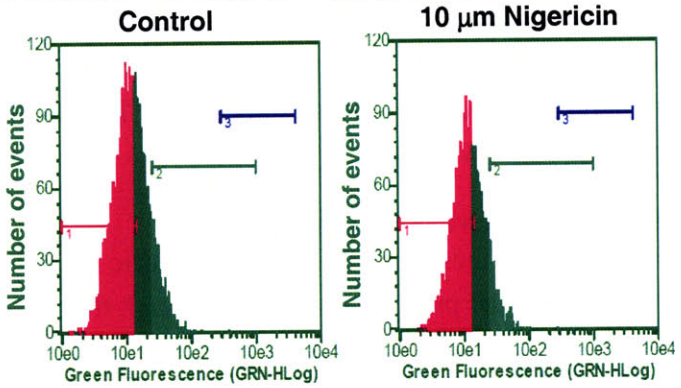

Figure 5-10: Membrane polarization assay. The left panel shows a flow cytometry plot of the control population of reporter cells showing baseline, unstimulated GFP expression. The right panel shows the the flow cytometry plot of the 10 μM nigericin-stimulated population.

5.2.7 Reactive species generation

The generation of reactive species due to electric field was previously explored by Wang *et al.* [138]. They found that for all conditions under which cell growth was delayed by field exposure, the media tested positively for hydrogen peroxide, thus confirming that hydrogen peroxide was indeed produced in the medium during field exposure. In subsequent experiments to determine whether hydrogen peroxide production depended on the particular cell suspending medium used in their

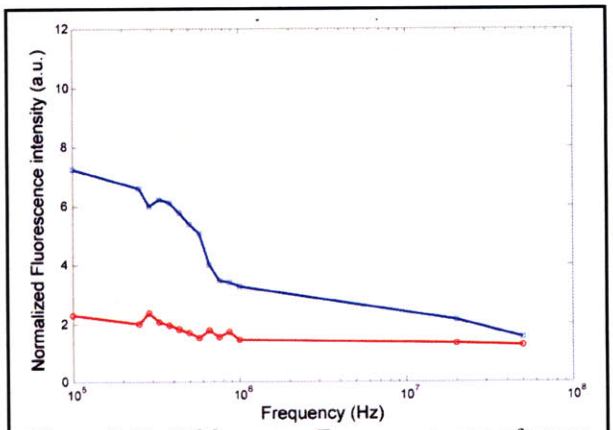

Figure 5-11: ROS assay. Frequency sweep of stress reporting cell line in the absence of catalase (blue) and in the presence of 100 mg/ml of catalase (red).

experiments, they determined that the glucose in the media was most likely dissociated in the formation of radicals. To test the generation of reactive oxygen species I performed assays using cell-permeable hydrogen peroxide sensing dyes and horse-radish peroxidase coupled cell-free assay (see Supplementary Information). Both these assays showed a pronounced trend of oxygen radicals at low frequencies and the presence of radicals could be attenuated with the addition of an appropriate radical scavenger. To confirm that oxygen radicals were indeed the dominant reactive species, an oxygen scavenger (100 μg/ml catalase) was dissolved in the media and the assay was repeated. The corresponding amount of oxygen scavenger was then used for the assays performed with the reporter cell line. These assays were repeated with the stress reporter cell line and the results are shown in Figure 5-10. The addition of an appropriate oxygen radical scavenger shows a ~ 3× decrease in the fluorescence intensity suggesting that the stress reporter cell line is responding to both heat and oxidative stress at low frequencies and that the increased stress at low frequencies is likely due to the integration of both these stressing factors at the very least.

5.2.8 MCF-10A verification assays

To verify that these results are not specific to the lineage of the parental cell type in which the reporter is constructed, a new reporter was constructed using MCF-10A cells [160]. MCF-10A cells are non-tumorigenic, human mammary epithelial cells which are adherent and importantly exhibit characteristic morphologies (i.e. comparable to those obtained on standard tissue culture substrates) when cultured on ITO substrates. This cell line was chosen as it was distinct in lineage from NIH 3T3 which are immortalized mouse mesenchymal cells. Additionally, MCF-10As are routinely cultured in biological labs and are well characterized [161]. Voltage and frequency sweeps performed with the MCF-10A cell line were comparable to those obtained with the NIH-3T3 cell lines, the main difference being that the time dynamics of the expression of these cells was different. Figure 5-11 shows a representative result of the MCF-10A reporter cell line. Importantly, it has a similar trend of increased stress at lower frequencies and provides further proof that the electric fields are interacting with the media to create these effects, which in turn are coupled to the cells through the oxidative stress response.

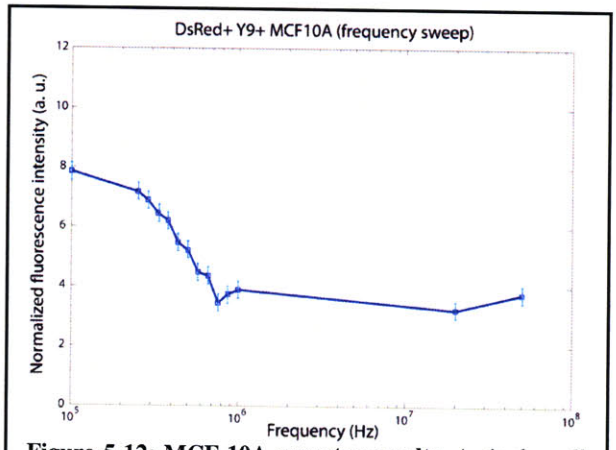

Figure 5-12: MCF-10A reporter results. A single, cell cloned reporter cell line generated in MCF-10A showed similar results to those obtained with the NIH-3T3 reporter cell line. The characteristic high stress at low frequency is exhibited in this assay as well.

5.3 DISCUSSION

The results presented in this chapter have important implications in Results open up important implications to both engineering and biology. The voltage sweeps indicate an increasing stress with the increase voltage (and consequently increasing heating) as is expected. Hence there is a trade-off with the design and operation of electrical traps (and more general electric-field based manipulation schemes) in that increased voltages could provide stronger traps but would also be more harmful to cell physiology. Decreasing voltage could be offset by providing increased duration of electrical field operation, thereby balancing cell health effect with trap efficacy. The dominance of reactive oxygen radical mediated stress at low frequencies indicates that high-frequency operation is considerably more desirable and would be a safer operating regime (at reasonably low voltages). The exact nature of these low frequency electric field stress would have to be investigated in further detail, one possible avenues could be the use of more specific cell reporters to hydrogen peroxide [162] that could be investigated using the platform presented herein. The implications of this work to fundamental biology involve the use of the microfabricated platform and associated electronics to study electric field interactions across large numbers of genes and numerous cell types. For example, by performing some minor redesigns of the platform it would be possible to collect a population of cells amenable to microarray-based analysis thereby providing a snapshot of electrically perturbed genes. Further, it could be used as a platform to study how particularly fastidious cell types, such as embryonic stem cells, would behave when exposed to such high-frequency fields. Finally, the stress reporting cell line itself is a valuable tool for both engineers and biologists in providing a convenient technique for either studying the impact of microsystems on cellular physiology and the study of drugs that promote or inhibit the heat shock response.

5.4 CONCLUSIONS

I have shown the design and implementation of a microfabricated platform with automated waveform generation for the electrical screening of mammalian cells. These electrical screens have been performed using well-characterized stress reporting cell lines and are the first assays to my knowledge that enable gene-expression analyses in response to electric fields. The results obtained with these assays provide information across applied voltage, frequency and duration enabling the generation of complex maps of cellular behavior.

5.5 MATERIALS & METHODS

Cell culture. NIH 3T3, DsRed^{+}NIH3T3, and MCF-10A cell lines were obtained from the ATCC. NIH 3T3 and DsRed^{+}NIH 3T3 cells were cultured using identical techniques with standard media formulations and culture practices (the DsRed^{+}NIH 3T3 cells were constructed as constitutive expressors of DsRed and generated using the pDsRed.T4 plasmid and have been previously used in microfluidic devices [163]). Briefly, NIH 3T3 and DsRed^{+}NIH 3T3 cells were grown in DMEM culture media supplemented with 10 % (v/v) bovine calf serum, 1% (v/v) L-glutamine, and 2% (v/v) penicillin-streptomycin. Cells were split every 2-3 days using standard trypsinization protocols (see Chapter 4 for details) and re-seeded at 1:10 split ratios.

MCF-10A cells were cultured in defined mammary epithelial growth media (CC-2571, MEGM Bullet Kit, Lonza, Inc.) supplanted with bovine pituitary extract and epidermal growth factor. MCF-10A cells were dissociated using Accumax (Innovative Cell Technologies) for 15 minutes at 37C and then quenched with specially prepared quenching media (DMEM with 20% fetal bovine serum). Accumax was used in lieu of trypsin as it was more effective in dissociating clumped cells and in generating more uniform single cell suspensions when performing seeding. Cells were subsequently spun down at 1000 rpm for 5 minutes. The supernatant was subsequently aspirated and supplanted with MEGM-based media. The cell pellet was then broken up by gentle trituration. The cells were then split at 1:2 split ratio.

Plasmids and plasmid preparation. Plasmids pDsRed.T4 (identical to the commercially available DsRED-CMV-Express, 632412, Clontech) and pY9 were provided courtesy of the Lindquist Lab. pDsRed.T4 (detailed plasmid map is provided in the Supplementary Information Section) is based on the pcDNA 3.1 backbone with a gentamicin antibiotic resistance gene. Plasmid pY9 based on the pHOT-MCS vector was generated by Vasanawala *et al.* and has been previously described [164]. Briefly, the cytomegalovirus (CMV) promoter of pcDNA3 (Invitrogen) was replaced by a BamHI—HindIII fragment of the human HSP70B promoter from the p173OR plasmid (StressGen, Victoria, BC). Importantly, this BamHI—HindIII fragment of the HSP70B promoter is merely 451 bp in size compared to the full length promoter (2.3 kbp) and provided ease of cloning. Additionally, like the pDsRed vector the pY9 vector that enables the selection of stable transfectants. The pY9 vector has the EGFP gene (Clontech) inserted as a reporter gene into the Kpn I—Not I multiple cloning site of the pHOT-MCS backbone. A detailed map of the pY9 plasmid is provided in the Supplementary Information section. Both the plasmids were cloned in chemically-competent bacterial strain, DH5α, and plated on kanamycin containing agarose plates. The antibiotic resistant colonies were then identified and a single colony was picked (using a colony-picker) and inoculated in a media-containing culture tube. This media tube was then placed in a shaker-incubator and allowed to grow overnight. The resultant culture was then used to "charge" a 150 ml flask of culture media which was again allowed to grow overnight at 37 °C. The resultant culture was now used for plasmid preparation. Plasmid preparation was performed using a standard plasmid purification kit (High-Speed Plasmid Purification kit – Midi, QIAGen, Inc.). Detailed protocols are provided in the Supplementary Information Section. Plasmid purity and concentration were then assessed using spectrophotometric techniques (ND-1000, NanoDrop Technologies, Inc.). Plasmids were subsequently labeled and stored at -20 °C for further use.

Transfection. NIH 3T3 cells were transfected using standard lipid-based transfection techniques. Briefly, plasmids were thawed and concentrations verified using spectrophotometry. For each plasmid, a final concentration of 1μg was obtained in 100 μl of serum-free and antibiotic-free media, specifically DMEM with 2 % (v/v) L-glutamine. Care was taken not to touch the sides of the tube while pipetting the plasmid solution. The plasmid constructs were mixed into the serum-free media by gently flicking the centrifuge tube. Fugene 6 transfection

reagent was then mixed in a 3:1 (v/v) ratio for pDsRed and 6:1 (v/v) ratio for pY9 and allowed to incubate for 15 minutes. The transfection media (transfection reagent + plasmid DNA + serum-free media) was then added to the cells in a drop-wise fashion. The 6-well plate was then swirled gently to ensure uniform mixing. The well plate was then returned to the incubator. Expression was then observed 12 hrs, 24 hrs and 48 hrs after transfection using fluorescence microscopy. MCF-10A cells were transfected with specialized buffers using an Amaxa electroporation system (following standard Amaxa electroporation programs and using standard Amaxa reagents, Nuclefection kit R, Lonza, Inc.). Again, cell expression was verified 24 hrs and 48 hrs after transfection using fluorescence microscopy to assess transfection efficiencies. Once cell expression had been verified both cell types were prepared for selection in antibiotic media. Prior to selection in antibiotic media a kill curve is constructed to determine the antibiotic concentration. The kill curve provides the minimum antibiotic concentration to use and is the lowest concentration that kills 100% of the cells in 1 - 5 days from the start of antibiotic selection. For the NIH-3T3 cells, the selection concentration was determined to be 1 mg/ml whereas for the MCF-10A it was determined to be 100 μg/ml.

Single Cell Cloning. The single cell cloning was initially performed using limiting dilution into 96-well plates. Cells were first sorted via FACS in two rounds to sort for highly-expressing reporters (top 5% in EGFP expression) and medium-expressing DsRed cells (top 25% in DsRed expression). Highly expressing DsRed cells were not chosen as there has been some evidence that high DsRed expression can prove to be cytotoxic. The two round of initial sorts served to take the starting heterogeneous transfected population that has been through 3 weeks of selection and turn it in to a more homogeneous of reporter cells which all had some level of EGFP and DsRed integration suggestion stable integration of both the pDsRed and pY9 plasmids. The sorted cells were grown to 70-80% confluence, trypsinized, quenched and subsequently counted on a Coulter counter. The cells were then primed for a dilution of 3 cells per well, 1 cell per well and 0.3 cells per well of a 96-well plate. This limiting dilution ratio was based on a 100 μL volume for each well in the 96-well plate, hence the final concentrations for the dilutions we 30 cells/mL, 10 cells/mL and 3 cells/mL. These dilutions were achieved by taking the trypsinized cells and re-suspending them in the corresponding volume of fresh culture media. These cell solutions were pipetted in to a sterile tray (typically 10 mL was pipette in to each tray) for subsequent seeding in to 96-well plates. Multichannel pipettes were then used to seed each well of the 96-well plate with 100 μL of media (each cell concentration was seeded in 3 96-plates, resulting in a total of 9 plates). The plates were then placed in the incubator to allow for cell attachment. 48 hours after seeding each of the plates was examined, and wells containing cells were marked. After another 48 hours, the plates were again examined to determine how many of the marked cells had colonies resulting from single cells (this was discerned by looking for single, isolated colonies in a well). After these wells were defined, the cells were allowed to proliferate for another day and a cellular stress assay (using 100 μg/ml arsenite) was applied to discern the level of reporter expression (see subsequent section for cellular stress assays). The

three highest expressing clones were determined by using automated microscopy to scan an entire well at both red and green-emission wavelengths and then determining the average intensity of the expression across the well. These clones were then expanded and frozen down for further experimental use. As is evidenced from this technique, the book-keeping of 9 plates can be extremely time-consuming and this places limitations on the number of clones that can be identified and expanded for experimental use. To simplify the first few steps of the process (i.e. dilution and seeding), a flow cytometer capable of sorting in to 96-well plates (MoFlo-3, BD Biosciences) was chosen for single cell cloning of the MCF-10A cells. This greatly simplified the preparation of the plates and reduced the number of plates involved from 9 to 5, and increased the number of wells with single cells (as the cytometer can be programmed to place a single cell in each well). However, the subsequent steps of identifying the viable and correctly expressing clones remains the same and is as detailed above. Again, in the case of the MCF-10A cells the three highest-expressing clones were chosen, expanded and frozen down for further experimental use.

RNA interference. Lentiviral pLKO.1-puro shRNA constructs were provided courtesy of Chengkai Dai. RNA interference using these lentiviral vectors has been previously described [152]. Briefly, genes encoding *GFP*, *H-RasV12D, PDGF-B*, myristoylated *AKT1*, *v-SRC*, *MYC*, and *LTA* were cloned into the retroviral vector pBABE-zeo. Stable virus packaging cell lines were prepared by transfecting individual plasmids into EcoPack2-293 cells using Lipofectamine (Invitrogen) followed by zeocin selection. Lentiviruses were produced by transiently co-transfecting individual shRNA constructs together with plasmids encoding ΔVPR and VSV-G together into 293T cells using Fugene 6 (Roche). Viral supernatants were collected and passed through 0.45μm syringe filters. Viral transduction was achieved by incubating target cells with viral supernatants containing 5μg/L polybrene (Sigma) overnight. The GFP-targeted sequence is: 5'-GCAAGCTGACCCTGAAGTTCA-3'; the sequence with no known homology (scramble) is: 5'-CCTAAGGTTAAGTCGCCCTCG-3'; the *HSF1*-targeted sequences are as followings: C2: 5'-GCTGCATACCTGCTGCCTTTA-3'; C3: 5'-CCCTGAAGAGTGAGGACATAA-3'; hA6: 5'-GCAGGTTGTTCATAGTCAGAA-3'; hA8: 5'- CCAGCAACAGAAAGTCGTCAA-3'; and hA9: 5' GCCCAAGTACTTCAAGCACAA-3'. Total protein content of cells was verified using Western blotting protocols. Detailed techniques for Western blotting can be found in the Supplementary Information section.

Cellular stress assays. Cellular stress assays were performed using the chemical stressor sodium (meta)arsenite. Sodium arsenite was dissolved in cell culture media (under aseptic conditions) to a final concentration of 100-250 μg/ml. This "stressing" media was then added to the cells by first aspirating the original media and performing a wash with PBS. The "stressing" media was left on the cells for 30 minutes (at 37 ºC) and then aspirated, followed by 2× PBS washes to ensure trace stressors were removed. Similar to heat shock techniques (described in Chapter 4), cells were assayed 12-14 hours after incubation at 37 ºC.

Flow cytometry. Cells were analyzed at multiple time points of stress and at various stress levels using a 96-well plate format flow cytometer (PCA-96 system, Guava Technologies). Cells were first trypsinized, quenched and then re-plated in round-bottom 96-well plates for analysis using the automated system. The CytoSoft 5.1 software suite was used to set the forward scatter thresholds, the detector gains (for the red and green fluorescence channels) and the corresponding gating regions. The corresponding wells for the assay were chosen and the system was then monitored while generating its histograms. Care was taken to ensure that all samples were comparisons were to be made were captured using the exact same systems settings. Histograms were then further analyzed using the CytoSoft 5.1 software package.

Microfabrication. Devices were fabricated starting with double-width (50 x 75 mm), indium tin oxide (ITO) coated glass slides with resistivity of 5-8 Ω/□ (SPI Supplies, Inc.). The ITO-coated glass slides were first cleaned with alternating 3× acetone and isopropanol rinses followed by a thorough rinse in DI water. Slides were subsequently baked at 150 °C for 30 minutes to remove any residual moisture. Slides were then coated with thin positive photoresist, OCG-825 (dynamic dispense, 750 rpm ramp, 5s, and final spin 1000 rpm for 35s) and the pre-baked at 90 °C for 30 minutes. Slides were then aligned and exposed on an i-Line ultraviolet exposure system (EV620, Electronic Visions). Exposed slides were subsequently developed in OCG 94 1:1 developer for 35 seconds. Developed slides were carefully observed under a fluorescence microscope to confirm that features had been accurately developed. The ITO features were then etched in dilute (1:1) hydrochloric acid for 20 minutes. The transparent nature of the film can make etch-termination processes difficult to visually characterize and to this end electrical measurements were made across the ITO features to ensure that no residual film remained. ITO-etched slides were 3× rinsed in DI water and subsequently dehydration-baked for 30 minutes at 150 °C. Slides were then coated with NR7-3000P lift-off resist to fabricate the temperature-sensing resistors, contact-pads and individual routing lines to each electrode patch. The slides were then coated in NR-7 negative tone lift-off resist (NR-7-3000P, Futurrex, Inc.) using static dispense techniques, 750 rpm (5 second) spread, and 1500 rpm (35 second) spin. Slides were then soft-baked at 100 °C on hot plates (with care being taken to read the actual plate temperatures using a thermocouple) for 15 minutes. Slides were then exposed

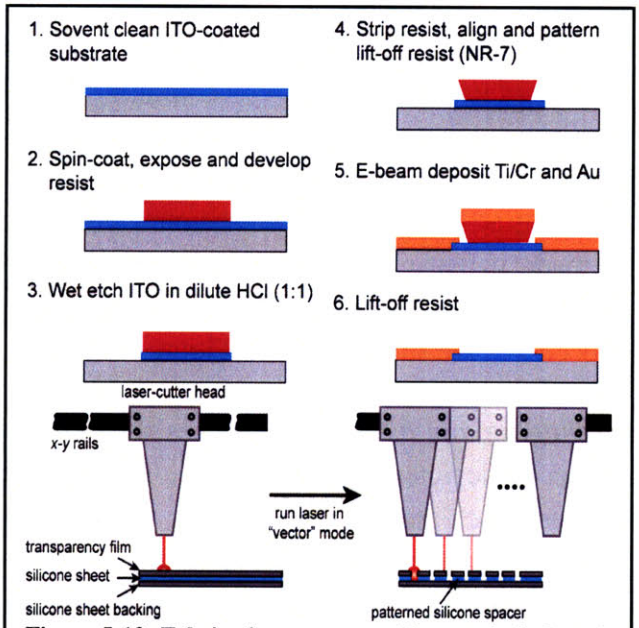

Figure 5-13: Fabrication processes. Top panel, dual mask process for patterning electrode sites, temperature sensing resistors and routing. Bottom panel, maskless process for fabricating silicone spacers to define volume for each electrode well.

with i-Line UV exposure (10 mJ/cm^2) for 5 seconds using a mask alignment tool (EV620, Electronic Visions). The slides were then post-baked at 150 °C for 15 minutes (again, with careful attention to the actual plate temperature measurement). Slides were subsequently developed in custom developer solution (RD6, Futurrex, Inc.) and then triple-rinsed in DI water. Slides were then loaded in an electron beam deposition system for coating with 100 Å of titanium and 1000 Å of gold (using pre-determined recipes). Gold-coated slides were then placed in a resist remover solution (RR4, Futurrex, Inc.) overnight to lift-off the NR7 resist. Stringers and extraneous metal film were removed by rinsing in DI water. Top electrode slides were fabricated in an analogous fashion with the exception that the ITO etching step was not required as the feature sizes are extremely large. The gold lift-off process serves the purpose of building a bus to route the grounding signal to the top electrode. Silicone membranes that serve as discrete wells for holding the cells and as spacers between the top and bottom electrodes are fabricated using laser-cutting techniques. Briefly, silicone sheets (125 μm thick, McMaster Carr Corporation) were clad between two transparency sheets and placed on the laser-cutter bed and aligned to the cutting origin. Well patterns that were drawn in software (CorelDraw 12) and after setting up the laser-cutter parameters (70% power, 50% speed and 1000 ppi), a dummy run is made to ensure that the membrane is correctly aligned. After cutting has completed, the membranes are cleaned with isoproponal and then autoclaved prior to use. The fabrication procedures are summarized in Figure 5-13.

Packaging and assembly. Devices were designed to be used with a reusable packaging scheme which is depicted in Figure 5-5. The packaging device consists of upper and lower plastic frames which are clamped together with the aid of screws in the four corners of the plates. The upper and lower plates each have sections for mounting custom-designed printed-circuit-boards (PCBs) which have rows of metalized push-pin connectors (0908, Mill Max Corp.). These connectors in turn are connected to a flex cable (ERCDA, Samtec Corp.). The flex cable is terminated in a twisted pair cable so that it can be routed through the connections at the back of standard cell culture incubator. The device and package are assembled inside a biosafety cabinet by laying the top electrode in bottom of a standard 15 cm culture dish. The autoclaved, patterned silicone membrane is then carefully laid on top of the electrodes and aligned to ensure that the wells are above the corresponding electrodes. Cells (at 10,000 cells/ml) are then pipetted in to each well (150 μl of cells are typically pipette in each well) and the top electrode is flipped over and gently placed on top of the silicone membrane. Excess media that was forced out of the wells is carefully dabbed off with a sterile swab. The assembled electrode structure is now placed in the bottom plastic frame of the package ensuring that the upper electrode bus is aligned with the push-pin connectors. The upper frame is then aligned with contact pads on the bottom electrode and screwed in to place taking care not to apply lateral forces and perturb the alignment of the pads and connectors. The assembled device was now moved to the incubator to allow for cell attachment and subsequent electrical stimulation to simulate dielectrophoretic trapping environments.

Electrical stimulation. Once the packaged device was assembled and placed in the cell culture incubator, the electrical connections from the package are connected to a custom-designed switchbox. The switchbox consists of a set of electrically-controlled reed relays for switching between different signals. A simple schematic of the system is depicted in Figure 5-12. Timing waveforms in transistor-transistor logic (TTL) format are generated using an off-the-shelf TTL generator (NI-6210, National Instruments). Additionally, connections from resistors were made to a universal serial bus (USB) controlled resistance/temperature logging unit (USB-Temp, Measurement Computing). This unit was used to log the resistance of each on-chip resistor over the course of the experiment (on-chip resistors were calibrated as described in the Supplementary Information section). The overall system was controlled through the generation of a waveform using a computer-controlled waveform generator (Agilent Technologies). A MATLAB script is used to generate initial waveform for stimulation and subsequently set the TTL-generator's pulse to high and thereby route the waveform to the first electrode site. A computerized timer then counts down from the specified time for stimulation and subsequently commands the generation of the next the waveform and routes it to the next electrode site and repeats the process for all 16 electrode sites. The overall MATLAB script therefore describes the entire experiment from the amplitude and frequency of the waveform and the duration of its exposure to the cells. In all, the system presents an automated technique for generating maps of cellular stress across three-dimensions of voltage, frequency and duration.

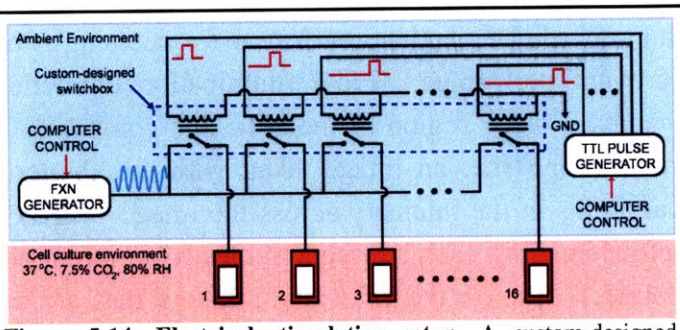

Figure 5-14: Electrical stimulation setup. A custom-designed computer-controlled relay box (dashed line) switches sinusoidal waveforms from a function generator to each individual electrode site. The entire electrical stimulation system resides outside of the incubator while the electrode array resides within the incubator at physiological conditions. Resistance measurements from each temperature sensitive-resistor at each electrode site are logged via a USB-controlled resistance logging unit. Steady-state temperatures are determined by fitting logged values to pre-determined calibration curves.

Automated microscopy and imaging. Once the electrical stimulation is completed the cells were allowed to recover (typically for 6-8 hours, but this varied with the stimulation durations in the experiment). The package was removed from the incubator and placed on a steel microscope stage insert (the base of the package is magnetized and so this prevents the movement of the package during the course of the imaging). The fiduciary markers of the first electrode site are then brought in to focus manually (using real-time video as visual feedback), and the camera and device axes are aligned to this marker. The stage is then translated in the x-direction and the last electrode sites are brought in to focus and the stage height at each focus is stored. This ensures good alignment between the camera and device axes and ensures that all the electrode sites can be imaged without any manual intervention. The stage is then moved back to the top-left-corner of the electrode site and brought in to sharp focus at the CCD camera manually (by viewing real-

time video images). This stage position is now set as the origin and serves as the reference point for all subsequent stage translations. Images using differential interference contrast, green-fluorescence (EGFP) and red-fluorescence (Cy3) are taken at each scan point (labeled with scan point coordinates and stored for post-processing). Image corrections for background correction were not performed. Field illumination corrections were deemed to be unnecessary after imaging a blank region of the slide and comparing fluorescence intensities in all channels to a "dark image" i.e. an image taken with the shutter closed and no light incident on the CCD (variations in the intensity across the image were comparable to the noise floor of the camera). Before imaging each subsequent electrode, an autofocus routine is performed. This autofocus routine is run on the fiduciary markers that are situated adjacent to each electrode. These markers include sets of closely-spaced lines patterned in gold which serve as the autofocus features. A stack of 10 images in the z-plane are obtained with 2 μm separation (by moving the microscope stage in the z position through software commands). This acquired image is subsequently analyzed using a MATLAB script to determine the best plane of focus using (see Supplementary Information section). To perform quantitative single-cell imaging of the reporter cells, the DsRed-image of the cells was used to identify the cells, the image was thresholded and a series of heuristics applied to – (1) remove clumps or grouped cells, (2) automatically disregard cells with a rounded morphology as they are most likely dead cells and hence not representative, (3) extraneous features that are identified with thresholding that are either too large or too small to be considered a considered a single cell, and (4) cells that were part of the boundary of the image were disregarded as the entire cell was not present in the field of view. This imaging technique is schematically depicted in Figure 5-5. The EGFP-image contained the actual information and was multiplied with the masked image to correctly identify the cells in the image; this is particularly important for control images (or weakly expressing cells) where the EGFP is very close to the background fluorescence. In this case, the DsRed-image is imperative for correctly identifying the number of cells. This scenario is depicted in Figure 5-13. Once the cells are correctly identified in the EGFP image, each cell is marked and its corresponding fluorescence intensity is determined by summing across the entire cell area and then normalizing across the cell area. The average fluorescence intensity per cell is then averaged for the entire electrode and normalized to the average fluorescence intensity from the negative control

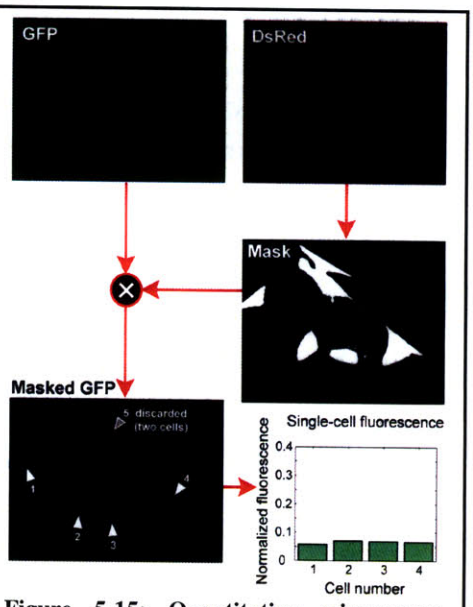

Figure 5-15: Quantitative microscopy. Constitutive DsRed expression plays an important role in the identification of weakly expressing fluorescent cells. The GFP image shows a near uniform fluorescence intensity with no evidence of cellular structures. The DsRed channel however, enables the visualization of these features. Masking these features then enables the identification of the cellular features. The algorithm then discriminates between both acellular features and clumps of cells ('Masked GFP' image). The resultant single cell flourescence data is shown in the plot.

electrode. The mean and standard deviation are plotted as a data point on each plot (hence each data point on the plot originates from ~1500 single cells). It should be emphasized that both the image acquisition and analysis techniques presented here are highly automated with minimal user intervention, with the exception of the set up of the image acquisition, the rest of the steps can be completely automated enabling the ability to perform more complex, high-content screens with the same platform and algorithms (and possibly a different reporter cell line).

Fluorescence microscopy. Fluorescent reporter cells were imaged using an AxioImager microscope (Carl Zeiss MicroImaging, Thornwood, NY) operating in epifluorescence mode. Images were taken using 20× (0.5 NA) and 40× (0.75 NA) LD epiplan objectives (Carl Zeiss MicroImaging). Fluorescence illumination was provided by an XCite 100 (EXFO Life Sciences and Industrial Division, Mississauga, Ontario) illumination source. EGFP (Set 38, Carl Zeiss MicroImaging), and TRITC filter sets (31000 and 31002, Chroma Technology) were used for imaging constitutive EGFP expression. All fluorescence images were acquired with 12-bit resolution using a cooled-CCD camera (ImagerQE, LA Vision). Care was taken to ensure that all images were recorded with identical acquisition parameters (exposure time, camera gain/gamma control and microscope aperture settings).

Reactive oxygen species (ROS) assays. Reactive oxygen species generation was assayed using two methods – (1) using a cell permeant dye to used to assay responses of live cells to ROS, and (2) using a enzymatic, cell-free assay to determine ROS generation in media. For (1), the cell permeant, fluorescent dye 5-(and-6)-carboxy-2',7'-dichlorodihydrofluorescein diacetate (carboxy-H_2DCFDA, component of I36007, Image-iT Live Green Reactive Oxygen Species detection kit, Invitrogen) was first prepared to a stock concentration of 10 mM in DMSO (D2650, Sigma-Aldrich) and then further diluted to a working concentration of 25 μM in DMEM-based cell culture media. NIH 3T3 cells grown in 10-cm dishes were first washed with PBS and then pulsed with 10 ml of this dye-containing media for 30 mins. Cells were subsequently 2× washed in PBS to remove any traces of the dye. Cells were now ready for seeding on the device and were trypsinized and harvested as previously described (see Cell Culture section) and seeded on the device for electrical stimulation. On completion of the electrical stimulation the cells were scanned and analyzed (see Automated microscopy and imaging section). As the carboxy-H_2DCFDA fluoresces at green-wavelengths (analogous to GFP) the imaging techniques and algorithms used were identical. For (2), the dye 10-acetyl-3,7-dihydroxyphenoxazine (Amplex Red, part of Amplex Red Hydrogen Peroxide/Peroxidase Assay kit, A22188, Invitrogen) was first warmed to room temperature and a dissolved in 60 μl of DMSO to prepare a 10 mM stock solution. The 5× Reaction buffer (Component C of Amplex Red kit) was diluted 5 fold in deionized water to generate a 1× Reaction buffer. A stock solution of horseradish peroxidase (HRP) was generated by dissolving the HRP in 1 ml of 1× Reaction buffer. A working solution for detection of hydrogen peroxide with 100 μM Amplex Red concentration is generated by combining 50 μl of 10 mM Amplex Red stock solution, 100 μl of

HRP stock solution, and 4.85 ml of 1× Reaction buffer. This working solution of 100 μM Amplex Red reagent was pipetted in to each well on the microfabricated platform and the electrical stimulation was performed. The platform was then immediately scanned using automated microscopy techniques (see Automated microscopy and imaging section) with the main difference being that no images were taken at green-wavelengths. As no cells were used in the assay, the image analysis comprised of averaging the red-wavelength images and normalizing them to the average of the negative control. To inhibit creation of ROS, oxygen scavenging radicals were used in both (1) and (2), and the assays were repeated to assess the impact of the inhibition. In (1) 100 μg/ml of catalase (C1345, Sigma-Aldrich) was dissolved in the cell culture media (and subsequently 0.2 μm filtered to ensure sterility) prior to the addition of carboxy-H_2DCFDA (subsequent steps in the assay were identical, see above). For (2) a concentration of 100 μg/ml of catalase was dissolved in the Amplex Red detection solution prior to loading the solution in to the wells (subsequent steps in the assay were identical, see above).

Membrane polarization assays. To assay the polarization of the membrane and its effects on the stress response, a known membrane depolarizing agent, 25 μM nigericin was dissolved in [K^+] buffered Ringer's solution (see Supplementary Information section for composition) and placed on the cells for 30 minutes. Cells were subsequently 3× rinsed in PBS to remove any traces of nigericin and were allowed to recover for 16 hours in standard cell culture media. Cells were subsequently trypsinized and analyzed using flow cytometry as described in the flow cytometry methods section.

5.6 ACKNOWLEDGEMENTS

I would like to thank Luke Whitesell for teaching me the fundamentals of bacterial culture, plasmid preparation and purification, and for assistance with all the Western blotting protocols. Chengkai Dai provided the lentiviral constructs. Simon Alberti provided the pDsred.T3 and pDsRed.T4 plasmids, and Brooke Bevis provided several helpful discussions regarding DsRed. Sandro Santaga provided helpful discussions about the heat shock response and specifically the use of $Y9^+$ cells in performing large-scale screens. Professors Bruce Bean and David Calpham provided valuable discussions regarding membrane polarization assays. The Microsystems Technology Laboratories staff provided valuable assistance with microfabrication techniques.

5.7 SUPPLEMENTARY INFORMATION

5.7.1 Western Blotting buffers and protocol

Wash and blocking buffers for the Western blots are described below,

Stock Wash Solution (5× TBSS):
100 mM Tris pH 7.6 (100 ml 1M Tris pH 7.6)
0.25% Tween 20 (2.5 ml Tween 20)

4.5% NaCl (45 g NaCl)

Blocking Buffer (BB):
3% (w/v) Nonfat Carnation milk powder in 1× TTBS (pH should be readjusted with NaOH to pH 7.6 if necessary). To prevent un-dissolved particulates the solution is transferred to a 50 ml tube and spun at ~2000 rpm. The resulting supernatant is used as the buffer.

Western blot protocol:
Whole-cell protein extracts were prepared in cold lysis buffer consisting of: 100 mM NaCl, 30 mM Tris-HCl (pH 7.6), 1% NP-40, 30 mM sodium fluoride, 1 mM EDTA, 1 mM sodium vanadate, and Complete protease inhibitor cocktail tablet (Roche Diagnostics). Samples were incubated on ice for 30 min and post-nuclear supernatants were recovered by centrifugation at 14,000 rpm at 4°C for 10 min. Protein concentrations were determined using BCA colorimetric reagent (Pierce Biochemical) and spectrophotometric absorption at 562 nm. Proteins were then separated on NuPAGE Novex gels and transferred to PROTRAN nitrocellulose membrane (Whatman). After transfer, membranes were stained with ponceau (Pierce Biochemical) assess equal loading of membranes and imaged using white light illumination on a gel documentation system (image shown in Figure 5-16). After imaging, the membrane was de-stained by rinsing briefly in water and then 2-3× in 1× TTBS for about 5 min (ensuring the red stain is no longer visible). Membranes were then blocked in BB for 1 hour and subsequently washed with PBS (pH 7.4) containing 0.1% Tween-20. Membranes were probed with the following antibodies - HSF1 (4356, ThermoFischer Scientific) diluted 1:50 (v/v) in BB and β-Actin (RB9421, ThermoFischer Scientific) diluted 1:100 (v/v) for 1hr at room temperature. Blotted membranes were subsequently washed in 5× (for 5 min each) with 1× TTBS. The secondary antibody was diluted to 1:20,000 (v/v) in BB and incubated for 1 hour at room temperature with the blotted membrane. The membrane was subsequently washed in 5× (for 5 min each) with 1× TTBS. To perform the detection, reagents for enhanced chemiluminescence (ECL) reagents were mixed 1:1 and incubated with the blot for 5 min on a plate rocker (ensuring that reagents were gently washing over the blot and keeping it moist). The blot is then carefully removed using tweezers, left to dry in air briefly (1-2 min) and then covered with Saran Wrap and placed on photographic film for 1 min in a dark room. The film is subsequently developed in an automated development system, and scanned using a flat-bed scanner.

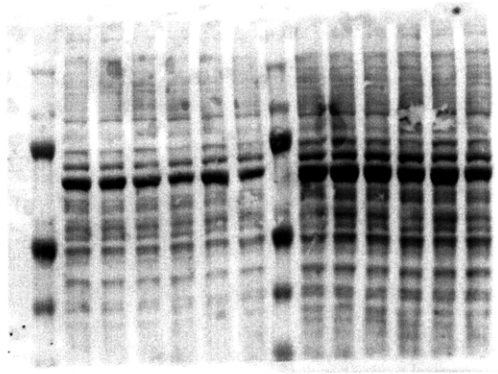

Figure 5-16: Western blot. Digital image of Ponceau-stained blot after gel electrophoresis. Blot shows 12 samples (6 left, 6 right) with two protein ladder markers. Concentrations among the 12 bands vary by 2X (6 bands on the right appear darker as they have a higher protein concentration). The central bands across all lanes represent proteins present in abundant quantities such as cytoskeletal proteins.

5.7.2 Plasmid Maps

5.7.2.1 DsRed plasmid

The DsRed plasmid is based on the pcDNA 3.1 plasmid backbone with an ampicillin antibiotic resistance gene. A CMV promoter drives the expression of DsRed. The specific regions of the plasmid map are specified below,

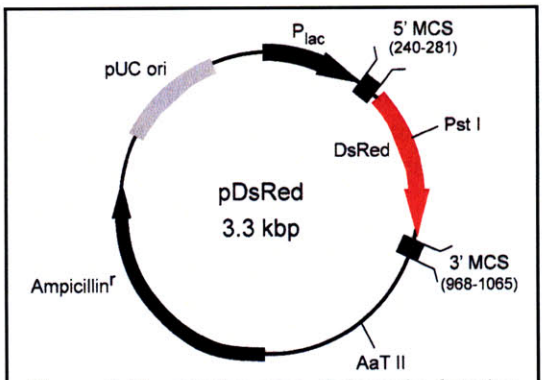

Figure 5-17: pDsRed map. Schematic denoting plasmid promoter, cloning regions, antibiotic resistance gene (ampicillin) and overall compositional makeup.

- Human cytomegalovirus (CMV) immediate early promoter: 1–589
  - Enhancer region: 59–465
  - TATA box: 554–560
  - Transcription start point: 583
  - C□ G mutation to remove *Sac* I site: 569
- MCS: 591–671
- *Discosoma sp.* Red Fluorescent Protein (DsRed) gene
  - Kozak consensus translation initiation site: 672–682
  - Start codon (ATG): 679–681; Stop codon: 1354–1356
- SV40 early mRNA polyadenylation signal
  - Polyadenylation signals: 1508–1513 & 1537–1542; mRNA 3' ends: 1546 & 1558
- f1 single-strand DNA origin: 1605–2060 (Packages the noncoding strand of DsRed2.)
- Bacterial promoter for expression of Kan_r gene:
  - –35 region: 2122–2127; –10 region: 2145–2150
  - Transcription start point: 2157
- SV40 origin of replication: 2401–2536
- SV40 early promoter
  - Enhancer (72-bp tandem repeats): 2234–2305 & 2306–2377
  - 21-bp repeats: 2381–2401, 2402–2422 & 2424–2444
  - Early promoter element: 2457–2463
  - Major transcription start points: 2453, 2491, 2497 & 2502
- Kanamycin/neomycin resistance gene
  - Neomycin phosphotransferase coding sequences: start codon (ATG): 2585–2587; stop codon: 3377–3379
  - G□ A mutation to remove *Pst* I site: 2767
  - C□ A (Arg to Ser) mutation to remove *Bss*H II site: 3113
- Herpes simplex virus (HSV) thymidine kinase (TK) polyadenylation signal
  - Polyadenylation signals: 3615–3620 & 3628–3633
- pUC plasmid replication origin: 3964–460

5.7.2.2 Y9 Plasmid

The Y9 plasmid is based on the pcDNA 3.1 plasmid backbone where the CMV promoter is replaced with a HSP with a 400 bp fragment of the HSP70B promoter. In addition to this promoter, the pcDNA 3.1 backbone possesses the following features – (1) multiple cloning sites in the forward and reverse direction to facilitate cloning, (2) a neomycin resistance gene for selection of stable cell lines, and (3) episomal replication in cell lines that are latently infected with SV40.

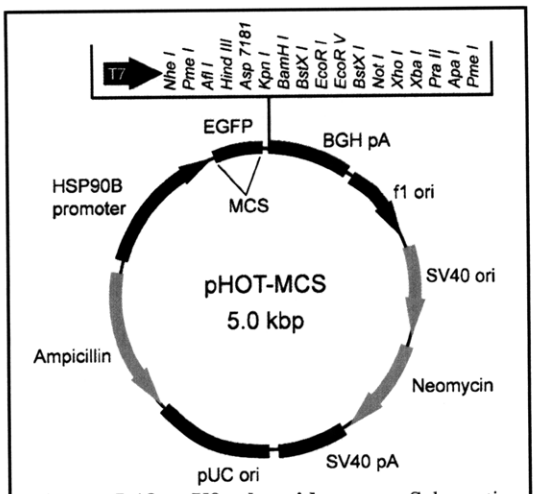

Figure 5-18: pY9 plasmid map. Schematic denoting plasmid promoter, cloning regions and overall compositional makeup.

HSP70B promoter: bases 232-685
T7 promoter/priming site: bases 863-882
Multiple cloning site: bases 895-1010
pcDNA 3.1/BGH reverse priming site: bases 1022-1039
f1 origin: bases 1298-1726
SV40 early promoter and origin: bases 1028-1252
Neomycin resistance gene (ORF): bases 2136-2930
SV40 early polyadenylation signal: bases 3104-3234
pUC origin: bases 3617-4287 (complementary strand)
Ampilicillin resistance gene: bases 4432-5428
Open reading frame: bases 4432-5292
Ribosome binding site: bases 5300-5304
Bla promoter: bases 5327-5333

5.7.3 Modeling

5.7.3.1 Effect of cell shape on electric field and transmembrane potential

A cell adhered to the substrate will reshape the electric field differently than a cell in suspension, and will thus experience a different transmembrane potential. By building a finite element model of a cell in suspension and conserving the area to generate a corresponding cell adhered to the electrodes, comparisons of the transmembrane loading on the cell can be made for each case, as shown in Figure 5-19.

5.7.3.2

If the chamber is covered with cells at an area fraction φ, the effective resistance is:

$$R \approx \frac{\rho_0 \rho_1}{\varphi \rho_0 + (1-\varphi)\rho_1} \frac{H}{WL}$$

where ρ_0 is the resistivity without a cell, and ρ_1 is the resistivity associated with a cell. Assuming the cells are uniformly distributed, the average power density in the chamber is:

$$q \approx \frac{V^2}{H^2}\left[\frac{\varphi\rho_0 + (1-\varphi)\rho_1}{\rho_0\rho_1}\right]$$

The temperature rise is proportional to q, so that the relative temperature rise is:

$$\frac{\Delta T_1}{\Delta T_0} = 1-\varphi\left[1-\frac{\rho_0}{\rho_1}\right]$$

The resistivity ratio can be approximated using the electric field around an adhered cell, and is itself a function of φ. For relatively small area fractions ($\varphi < ½$), we can use $(\rho_1/\rho_0) \approx 1+1.4\,\varphi$, so that:

$$\frac{\Delta T_1}{\Delta T_0} \approx 1-\varphi\left[1-\frac{1}{1+1.4\varphi}\right]$$

For $\varphi = 0.5$, the temperature rise would be ~80% of its value at $\varphi = 0$ and correspondingly for $\varphi = 0.1$, the temperature rise would be ~99% of its value at $\varphi = 0$. Consequently, a seeding density for the cells is determined by trading off the number of cells required to achieve statistical significance between results and the ability to seed single cell populations with the need to ensure that the cells do not completely screen the electric fields. In the case of my experiments, based on the seeding densities used (and with verification from image-based tabulation of total number of cells), corresponds to an average value of φ of ~ 0.35.

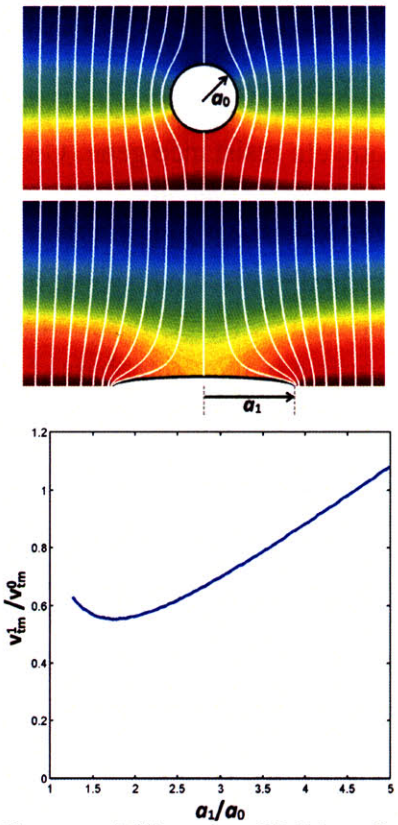

Figure 5-19: Model for transmembrane potential. Top panel shows cross-sectional view of a chamber with a suspended cell (top) and adhered cell (bottom). Bottom panel shows the variation in the transmembrane potential for an adhered cell (with radius a_1) normalized to a suspended cell (with radius a_2).

5.7.4 Plasmid purification

Plasmid purification was performed using a standard plasmid prep kit (Hi-Speed Midi Kit, Qiagen, Inc.). This particular kit was chosen as it eliminated repeated centrifugation steps in the purification process and was easier to perform.

1. A single colony from a freshly streaked selective plate is picked (using a colony picker) and used to inoculate a starter culture of 2–5 ml LB medium containing the appropriate selective antibiotic. The culture is incubated for ~8 h at 37°C with vigorous shaking (at ~300 rpm).
2. The starter culture is diluted 500 to 1000 into 3 ml selective LB medium. Grow at 37°C for 12–16 h with vigorous shaking (~ 300 rpm) and the culture should reach a

cell density of ~ $4x10^9$ cells/ml.
3. Cells are harvested by centrifugation at 6000 x *g* for 15 min at 4 °C. As a starting point for another purification, media is aspirated and the pellet is labeled and frozen at -20 °C.
4. The bacterial pellet is resuspended in 0.3 ml of Buffer P1 (ensuring that RNAse A has been added to Buffer P1 beforehand).
5. 0.3 ml of Buffer P2 is added and mix thoroughly by vigorously inverting the sealed tube 4–6 times. The tube is then incubated at room temperature (15–25°C) for 5 min.
6. 0.3 ml of chilled Buffer P3 is added. This is mixed immediately and thoroughly by vigorously inverting the tip 4–6 times, and incubated on wet ice for 5 min.
7. This solution is centrifuged at 14,000 rpm in a microcentrifuge for 10 min. The supernatant containing plasmid DNA is promptly removed.
8. A QIAGEN-tip 20 is equilibrated by applying 1 ml Buffer QBT, and allowing the column to empty by gravity flow.
9. The supernatant from step 7 is added to the QIAGEN-tip 20 and allow it to enter the column resin by gravity flow.
10. A 2× wash of the QIAGEN-tip 20 is performed with 2 ml Buffer QC.
11. The DNA is eluted with 0.8 ml Buffer QF.
12. The DNA is precipitated by adding 0.7 volumes (0.56 ml per 0.8 ml of elution volume) of room-temperature isopropanol to the eluted DNA. This is mixed and centrifuged immediately at □10,000 rpm for 30 min in a microcentrifuge. The supernatant is carefully decanted.
13. The DNA pellet is washed with 1 ml of 70% ethanol and centrifuged at 10,000 rpm for 10 min. The supernatant is decanted taking care not to disturb the pellet.
14. The pellet is air-dried for 5–10 min, and the DNA is subsequently re-dissolved in a suitable volume of buffer (e.g., TE buffer, pH 8.0, or 10mM Tris·Cl, pH 8.5). Note that repeated triturating of the DNA to promote resuspension may cause shearing and should be avoided.
15. The dissolved DNA is now analyzed using a spectrophotometer to assess purity and concentration. The concentration is noted on the tube and the plasmid DNA can now be stored at -20 °C until further use.

5.7.5 Ringer's Solution

[K^+]-buffered Ringer's solution should ideally approximate the cellular ionic contents. Usually these concentrations are not known precisely, but a good approximation is to use 120 mM K^+, l0 mM Na^+, 1 mM Mg^{2+}, 30 mM Cl^-, 100 mM Ca^{2+} (or Ca^{2+} free), 100 mM gluconate (or cyclamate or some other impermeant anion), l0 mM glucose, and l0 mM HEPES.

5.7.6 Resistor calibration

On-chip resistors are calibrated by using an adhesive-backed thermocouple (SA1-T, Omega) and placing it on the resistor. The chip is then placed on a hot plate and the temperature is ramped in ~ 5 °C increments starting at room temperature. The resistance value of the resistor is tabulated

using a mulitmeter. The characteristic curve for the resistor is plotted and fitted to a straight line. This fitted function is then used to determine temperature from resistance. This procedure is repeated for each resistor on-chip as resistance values can vary across the device due to non-uniformities in the fabrication process.

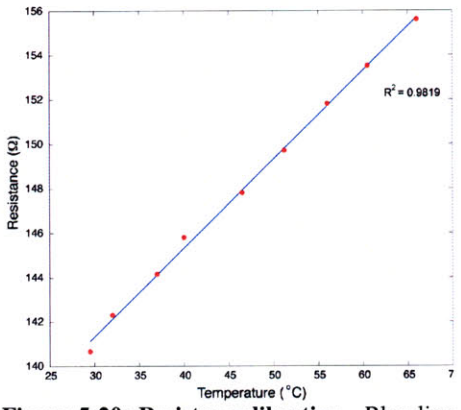

Figure 5-20: Resistor calibration. Blue line shows characteristic fit (with $R^2 = 0.9819$) to measured temperature dependence (red circles) of on-chip resistors. Such fitted functions are used to determine temperature from resistance during temperature and voltage sweep experiments.

5.7.7 Autofocus routines

The autofocus algorithm implemented in MATLAB, takes images at different focal planes and stores the intensity profile across the evenly spaced line features. This intensity profile is compared to a previously stored, best-plane-of-focus profile taken prior to the start of the experiment (only one of these profiles is stored, as the autofocus features are the same for each electrode). The difference between the profiles at each plane and the best-plane-of-focus profile is then stored and compared to each other. By choosing the plane of focus that has the least spatial variation in differential intensity, is chosen as the best plane of focus. The stage position value stored for that particular focal plane is then chosen as the plane-of-focus for that experiment.

Chapter 6 - **Conclusions**

In this chapter I will conclude with the major contributions of this thesis. I will then give my outlook for future work with specific projects that could be pursued to build upon the contributions that have been outlined in this thesis. It is intended that these perspectives on future work serve as guidelines for future investigators.

6.1 Thesis contributions

The contributions of this thesis span fabrication methodologies, metrology tools and biological responses to electric fields. Specifically, this thesis presents the following five main research contributions,

6.1.1 Development of a photopatterned silicone fabrication process

The characterization of photopatterned silicone (PPS) in terms of its feature resolution, alignment capability, autofluorescence, and biocompatibility has been presented and serves as a new material system for biological microsystems. The capabilities of this material system have been exemplified in the design and implementation of a single bioparticle trap capable of leveraging both hydrodynamic capture and dielectrophoretic loading and release. The implications of this material system are wide-ranging as they can enable the design of architectures that could not be previously realized. This is particularly emphasized by the development of the single bioparticle trap that would be extremely challenging to construct using soft-lithography-based fabrication techniques. By providing device designers with a new material system that combines the advantages of both PDMS and SU-8, this material system can now be applied to the construction of highly integrated systems. The in-depth process development and characterization of PPS provide device fabricators and end-users alike with important information about its application space. Previously, PPS has only been characterized in the context of electronics packaging systems. Characterizing its application to biological systems presents an important advance in biological microsystems technology.

6.1.2 Design and implementation of a vesicle-based metrology technique

Giant vesicles have important implications for biophysical studies and serve a role as model particles for elucidating membrane dynamics. In this thesis I have demonstrated the first known use of giant vesicles as electrical test particles. In particular, the use of polymer brushes to alter electrical properties has been previously unexplored. This achievement opens up new avenues for the design of giant vesicles as generalized metrology tools for microsystems. Further, the use of fluorescently-labeled vesicles enables the encoding of vesicle properties within their fluorescent spectra and points to the creation of larger libraries of vesicles with unique electrical properties. Due to the exquisite control over the electromechanical and chemical properties of vesicles, they present a fundamental advance over polystyrene microspheres which are the most commonly used test particles for microsystems. In all, the design, implementation and

characterization of electrically distinct vesicles form the first steps towards the design of large libraries of test particles for use in any dielectrophoresis-based microsystem.

6.1.3 Construction and characterization of a stress-reporting cell line

Characterizing the impact of environmental changes on cells can be performed by a large number of assays ranging from the cell-level, protein-level to the gene-level. These assays can prove time consuming and difficult to quantify. I have created a stress reporter cell line that combines ease of use with sensitive detection in physiological media. This stress reporting cell line with constitutive DsRed expression and stress-inducible GFP expression presents a new, well-characterized cell line that can be used in a wide variety of microsystems. This cell line provides a quantifiable fluorescence-based readout making detection highly streamlined and eliminating the need for performing molecular biology assays such as immunofluorescence and PCR (which can be hard to automate and multiplex). Further, this reporter cell line responds to a number of stressors ranging from heat, oxygen radicals and heavy metals permitting its use in a wide variety of assays and systems. As this reporter cell line provides readout using standard fluorescence microscopy techniques, it enables dissemination of the cell line to other laboratories. Additionally, the stress reporter cell line has a canonical (NIH 3T3) parental cell lineage which presents a simple culture protocol further reducing the barrier to adoption of the cells by other research groups. Taken together, the advantages this cell line present a unique contribution to the biological microsystems community in the development of a new "reagent" for the testing of the physiological impact of any biological microsystems.

6.1.4 Development of a high-content screening platform.

A microfabricated device forms the crux of the high-content screening platform and can be used for the simultaneous investigation of 16 distinct electrical waveforms on the expression of stress-reporting cells. The microfabrication technologies used to realize this platform present distinct enhancements and contributions in and of themselves – (1) the fabrication process flow successfully integrates the processing of gold with indium-tin-oxide, two materials widely used in biological microsystems, but typically not used in conjunction, (2) the use of laser-cutting techniques to create individual silicone well presents a significantly simpler process than the use of stencil molding techniques, and (3) process optimizations for the use of NR-7 photoresists creates a distinctly simpler lift-off process for fabricating gold microstructures compared to conventional image reversal resist. In addition to fabrication advances, this thesis demonstrates the first known system for the screening a wide range of electrical conditions across cells. Such "electrical" screens would be extremely difficult to perform using conventional well-plate-based high-content screening assays. In the construction of this system, the supporting electronics and imaging algorithms result in a highly-automated platform with minimal user intervention capable of scaling up to increasingly complex screens. The imaging algorithms presented herein could be equally applied to other image-based screens and for the quantification of other reporter cell lines. The supporting electronic systems could also be applied for use in other DEP-based microsystems for the controlled switching and routing of electrical waveforms. As constructed,

this system can also be used with practically any adherent, fluorescent reporter cell line to perform fundamental scientific studies to elucidate the effects of electric fields on the expression of other genes of interest.

6.1.5 Elucidating the impact of electric fields on cellular physiology

Using both the stress reporter cell line and the screening platform, a number of assays have been performed to elucidate the effects of electric fields ranging in frequency from 250 kHz to 50 MHz and field strengths from 10 kV/m to 100 kV/m. The ability to routinely perform such assays points the ability to perform large numbers of assays to map electric field effects across field-strength, field-frequency and field application duration. Maps of stress versus voltage indicate that increasing voltage contributes to increasing stress, due to the increased Joule heating in the media. This provides evidence electric fields can indeed alter cell physiology at the level of gene expression. Indeed, the induction of stress It was also discovered that there is a trade-off between applied voltage and duration in the application of voltage i.e. a low voltage applied for a long duration is analogous to a high voltage applied for a short duration. Maps of stress versus frequencies indicate that there are pronounced stressful events at lower frequencies. This increased stress at lower frequencies was determined to be due to contributions from reactive oxygen species generation in the cell culture media.

6.2 Perspectives on future work

The results presented in this thesis present the first steps in the development of several new technologies and provide proof-of-concepts of these techniques. The biological results presented herein represent the use of a reporter for heat stress, and represent the first steps to obtaining an understanding of how electric fields couple with cells. Moving forward there are several compelling directions this research can be built upon to both increase our understanding of cellular physiology and also further our ability to build cell-based microsystems.

6.2.1 Fabrication technologies

Building microwells for non-adherent cell studies. One of the disadvantages of the microfabricated platform for performing electrical screens is that it is optimized for use with adherent cells and would prove difficult to use with non-adherent cells. Tailoring the system for use with non-adherent cells would require the creation of discrete microwells for capturing single cells. Such microwells have been the subject of considerable study [165] and have been demonstrated to have a good ability to capture single cells. Indeed, work in our own research group has leveraged the unique capabilities of microwell arrays to enable patterning of single embryonic stem cells[166]. Microwells are typically fabricated using soft-lithography-based fabrication techniques where wells are formed by relief casting on an array of lithographically defined posts. Thus these microwells are connected with the underlying bulk elastomer, making it difficult to integrate with electrodes. An alternate strategy would be the design of an elastomeric stencil (using a slightly modified molding procedure, which eliminates the bulk

connector). However, such a stencil would be required to be only one cell-diameter thick (~ 15 μm) would be extremely difficult to manipulate and align to electrodes. This clearly points to the need for a new material system that could be aligned and patterned to electrode features. Clearly, PPS is an ideal candidate material due to its demonstrated culture compatibility and ability to be aligned with electrodes. Further, its demonstrated low-autofluorescence is ideal for its integration in to the microscopy techniques use for assay readout. Indeed, the stringent requirements for imaging would preclude the use of SU-8 and other photoresists which have significant autofluoresence in the wavelengths of interest (see § 2.2.4). The PPS could therefore be used to create well-aligned microwell arrays on top of the electrode structures. Importantly, this would not alter any of the subsequent packaging and assembly steps and would require only the generation of an extra mask layer. The descum process for PPS would play an important role in ensuring that the bottoms of the wells are completely free of residue and enable the propagation of electric fields. This descum process is in essence "self-masking", in that the structures themselves would serve as a mask for removal of the residual scum. Consequently, the incorporation of the descum step would add an additional process step but would not require the generation of an additional mask or the need for an alignment step.

Automating OPTOFLUCS. The generation of PPS microwell arrays could have important implications for other live-cell studies. In particular, microwells containing single cells have been previously used in our lab to sequester and monitor large (~10,000) populations of cells [167], in a technique termed OPTOFLUCS. These cells are subsequently interrogated using fluorescence microscopy and cells of interest are isolated using an infrared laser, in a strategy akin to laser capture microdissection. One of the limiting factors in completely automating this technique is the need to refocus the laser for each well of interest. This is due to the fact that variations in the underlying PDMS result in sub-optimal positioning of the laser spot (requiring manual intervention at each site). By eliminating the underlying PDMS by building the wells directly out of PPS presents an opportunity for automating the release of target cells. The design of PPS-based wells would only require minimal changes to the overall system design, in particular because the wells can be fabricated first on a glass coverslip, a larger fluidic channel could be bonded on top of this PPS layer. Again, such a system would rely on an effective descum process that would remove any excess residue from the bottom of the wells. This descum process has already been developed [1] and would only add a single, maskless post-processing step to the fabrication procedure.

Descum process optimizations. As has been previously established, the descum process has been developed and has proven results for the removal of excess residues around structures. This process was established and evaluated on cell capture cups and the process was characterized by taking images of structures before and after descum procedures. The process can easily be further enhanced by increasing RF operating powers and adjusting gas flow rates during reactive ion etching to obtain a more time-efficient process. Certainly, the descum process can also be further characterized, particularly in quantifying how much sharper side-walls become. It would

also be interesting to quantify the roughness of PPS structures before and after descum procedures to see if there is any significant roughening as a result of plasma exposure. SEM images do not indicate any severe alterations in surface features, but a more sensitive technique such as atomic force microscopy (AFM) could be employed to address these concerns. The effects of further improving the descum process could enable the fabrication of PPS structures that are closer representations of mask features, and close the resolution gap between PPS and photoresist-based structures. Such an advance would open up new avenues for the use of PPS in robust, live-cell manipulation architectures.

6.2.2 Vesicle-based metrology tools

Extending the vesicle library. The ability to tailor the electrical properties of vesicles and manipulate them in electric fields has important implications in the design of metrology tools for biological microsystems. In particular, the measurements of key properties within a microsystem could be achieved using such particles. Such properties could involve sensing pH, temperature, and osmolarity. Currently these environmental conditions are measured using fluorescent dyes. While this may prove effective for studying overall system effects it might be valuable to study more localized effects, for example, conditions within a dielectrophoretic or optical trap. Previous studies at measuring such localized effects have involved polystyrene beads infused with thermochromic liquid crystals [168]. While such systems are valuable they are challenging to construct and difficult to multiplex. Alternately, vesicles encapsulating environment-sensitive dye could be used to provide a snapshot of the environment within an electrical or optical trap. Importantly, these vesicles could also incorporate lipophilic dyes, such as voltage-sensitive dyes, opening another avenue of measurements capable with vesicles. Such a set of vesicles could be used as generalized tools for microenvironment measurements within microsystems.

Polymeric test particles. While giant vesicles are readily formed, one of the main drawbacks of the use of giant vesicles is that they have a limited shelf-life at room temperature. They typically are stable for 2-3 days at 4 °C and can be used directly if appropriately stored. In my experience there was a significant attrition in the number of large (greater than 20 μm) vesicles after 3 days. This lifetime of vesicles can be extended by freezing them at -20 °C and then thawing them when needed for experiments. Vesicles thawed after one month at -20 °C behaved as expected but there was significantly more lipid aggregates from ruptured vesicles (presumably generated during the freeze/thaw procedure). To generate a more stable particle, it could be possible to generate particles using polymers. These polymeric analogs of vesicles are termed polymerosomes and have garnered considerable interest as therapeutic models [169]. Polymerosomes can be formed using the same electroformation techniques used for the formation of vesicles. The use of diblock and triblock starting polymers has important applications on the structure and curvature of the resulting polymeric membrane. To preserve the membrane morphology and generate a more stable particle it might be possible to add a small

amount of photopolymerizable lipid to the lipid mixture used to form the vesicle. The vesicle could then be exposed to short pulse of UV-radiation (using a Xenon arc lamp or a collimated fluorescent light source) to polymerize and cross-link the membrane. Assuming that the photopolymerization and cross-linking of the membrane does not confer a large charge on the membrane, this might be a viable strategy for the generation of more stable test particles (which could be stored at room temperatures for weeks at a time).

Tools for membrane metrology. Giant vesicles serve as important model membranes due to the fact that their large size affords ease of visualization and manipulation using micropipettes. Membrane properties are important in conferring overall functional properties to cells. For example, immune type B cell membranes play important roles in communicating with antigens through membrane structures. Importantly, it has been postulated that the mechanical properties of B cell membranes play an important role in the recognition of antigens [170]. In collaboration with Carlos Castro of Biological Engineering at MIT, I was trying to build giant vesicles as test systems for measuring the mechanical properties of membranes (as depicted in Figure 6-1). Specifically these vesicles incorporated biotinylated lipids in their membranes as attachment sites for streptavidin-coated 1 μm beads. The idea was to pull on these beads using laser tweezers and measure the force for pulling tethers from these model membranes. These measurements could then be compared to those for B cells as baseline measurements for the mechanical properties of unmodified membranes and how they compare to a more complex membrane (previous measurements with membrane tethers have involved live cells such as chick embryo fibroblast and NIH 3T3 fibroblasts [171]). It could even be envisioned that proteins could be serially incorporated in to the membrane to determine the contributors of the unique mechanical properties of the B-cell membrane. Vesicles could also find applications in the use of studying the mechanisms of membrane fusion as has been previously demonstrated in understanding the time dynamics of membrane fusion [70]. Given microfluidic devices for cell-pairing and fusion developed in our lab [163], vesicles with fluorescently labeled membranes (as shown in Figure 3-2A & B) could be used as test particles

Figure 6-1: Vesicles for membrane metrology. (A) Schematic of giant vesicles with biotinylated lipids. These lipids act as targets for streptavidin-functionalized microspheres. These phospholipids have been electroformed using standard electroformation techniques, as shown in (B). Scale bar 50 μm. (C) Shows fluorescence microcscopy images with fluorescently modified biotinylated lipids show that these lipids organize in the membrane and can be visualized. Blue arrowheads indicate vesicles with well defined membranes.

to better elucidate the mechanisms of membrane fusion. A microfluidic approach would enable the study the large numbers of paired vesicles.

6.2.3 Live-cell metrology tools for biological microsystems

Extending the capabilities of live-cell reporters. The reporter cell line described in this thesis was specific to cellular stress. While it was capable of integrating the responses of other stressors such as oxidative radicals, it was difficult to use the cell line to isolate effects from different stressors. This could be achieved by using either a dual-reporter system in a single cell line (which might be challenging to clone) but more realistically a number of cell lines could be constructed to assay for other effects of electric fields. These could include intracellular hydrogen peroxide and calcium sensors that have been recently developed [162, 172]. Additionally, plasmids encoding for these sensors are commercially available. Importantly, these sensors can be easily integrated within the cell and used for cell health assays. To study more general effects cell lines that incorporate reporters for a DNA damage pathway could prove to be extremely useful. Indeed, the construction and validation of such cell lines has recently formed the subject of a research grant proposal and could become increasingly important in the biological characterization of microsystems.

Enhancing reporter cell lines. The reporter cell line was constructed using standard techniques for transfection and cloning and with standard, open-source plasmids. Technologies for transfection and construction of reporter systems have progressed rapidly in recent years. In particular, the advent of cell-line optimized protocols and reagents for transfection has increased the transfection efficiencies for certain cell types. Such protocols were crucial in the construction of the MCF-10A [160, 161] reporter line (lipid-based transfection techniques had low transfection efficiencies, making downstream selection and cloning extremely challenging). Moving forward, I would consider the use of such optimized protocols and reagents for electroporation instead of lipid-based transfection techniques. The use of such optimized protocols decrease the time needed to build a cell line and open the door to the construction of reporters in more challenging, hard-to-transfect cell types (e.g. embryonic stem cells). For the purposes of quantification, new reporter constructs provide compelling enhancements to the systems described here. In particular, one the constructs that stands out is the Rheoswitch ® system (New England Biolabs). This involves the addition of a small molecule to the media that inhibits the expression of the reporter system when not activated, resulting in extremely low baseline fluorescence. A system could be envisioned where the reporter cell line is generated using this construct and the small molecule is added prior to seeding the cells on the electrodes. The experiment could then be carried out ensuring that the control population has the lowest baseline expression and assuming negligible autofluorescence of the media could serve as a technique for increasing the dynamic range for detection (by effectively lowering the control population expression).

Extending reporter cell line library. To demonstrate the full power of reporter cell lines as metrology tools, a larger set of parental cell lines would need to be used to construct reporters. This would provide end-users with at the very least a cell line with similar morphology and lineage to their cell line of interest. While it would be prohibitively time consuming to generate large libraries of such reporters, the replication of reporters in at least 4-5 other lineages would decrease their barrier to entry. As a first step toward this, I have constructed a stress reporter cell line in BA/F3 pro B cells. This line still needs to be cloned but as is evident in the images (in Figure 6-2) they are functioning as expected (indicating stable integration of the construct). The construction of this cell line could prove synergistic with efforts to build a system for screening electric field effects in non-adherent cells (as outlined in section). Importantly, such a cell line could also be used for studying the impact of optical tweezer manipulations on type B cells.

Applications of stress-reporter cell line. As has been previously mentioned the reporter cell lines constructed in this thesis are specific to cellular stress. However, there might be other mechanisms that are relevant in microsystems that may also activate this stress response. For example, shear forces in microsystems can reach in excess of 10 dyn/cm^2. Studying the impact of these shear stresses on cellular physiology has important implications in the design of microfluidic perfusion culture systems. The effects of shear in inertial flow focusing [173, 174] is also important and poses an important possible application for these reporter cells. Digital microfluidics [175] is another important application area. In fact, in collaboration with the Wheeler Lab at the University of Toronto the BA/F3 stress reporter cells (mentioned in the previous section) are currently being used to test the effects of manipulation of discrete droplets in microfabricated systems. Such systems employ electrowetting techniques raising the question of electric field coupling with cells, an ideal question that can be answered with the help of this cell line.

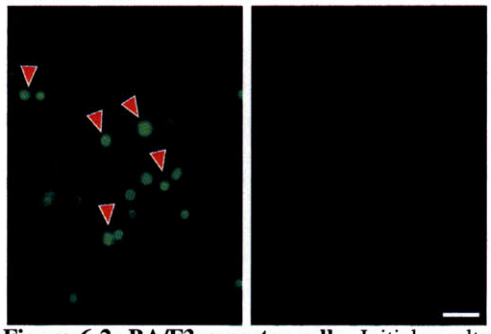

Figure 6-2: BA/F3 reporter cells. Initial results with mouse pro B cells indicates a robust response to stressful conditions as shown in (A) with red arrowheads. Control cell populations have a low baseline fluorescence as is seen in (B). Both (A) and (B) are merged phase and fluorescence microscopy images where care was taken to ensure that imaging conditions and exposure times for both populations were the same. Scale bar 40 μm.

Constitutively-expressing fluorescent cell lines. Constitutive expressing cells have been widely used in our laboratory for use in testing microsystems and to avoid the use of tedious live-cell staining techniques prior to every experiment. These fluorescent cells not only save time and reagents but as they are constantly producing fluorescent protein have a consistent fluorescent signal which does not fade over successive cells divisions (as in the case of staining). This makes these fluorescent cells more amenable to assays where downstream biological function and analysis are important. As previously mentioned red and green fibroblasts have been constructed and used to great effect in cell fusion experiments [163]. To extend this library of

fibroblast cells, the first steps towards constructing a blue-fluorescent protein expressing fibroblast cell line have been undertaken. Initial results are shown in Figure 6-3. These cells are constructed using an open-source PS-CFP2 plasmid [176] and can be cloned using standard cloning techniques. Importantly, they provide another degree-of-freedom when performing proof-of-concept sorting and patterning experiments. They also provide an alternative to calcein-based dyes at blue-wavelengths (which are typically only weakly fluorescing). BA/F3 pro B cells have also been constructed with constitutive red fluorescent (DsRed) protein expression (as was outlined in Chapter 3). Similarly, they provide a useful test cell line for patterning and tracking of cells in microsystems, and these particular cells have even found uses as the cell line of choice for educational projects. Extending these fluorescent lines to the creation of, at the very least, single-cell cloned blue-3T3s, green-BA/F3s and blue-BA/F3s could have a considerable impact on assays performed in our lab. Further, these cells could easily be disseminated to other labs for use in their own microsystems-based assays.

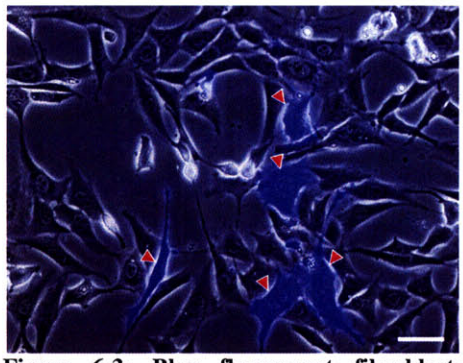

Figure 6-3: Blue fluorescent fibroblasts. Merged fluorescence and phase microscopy image of PS-CFP2-expressing fibroblasts (red arrowheads). Such fibroblasts would present important implications for test screens for cell sorting, patterning and even cell fusion. Scale bar 25 μm.

6.2.4 High-content screening platform

Extending numbers of electrode sites. The high-content screening platform described in this thesis incorporates 16 individually addressable electrodes. The microfabrication techniques could be scaled to incorporate a greater number of electrodes, however, this would have to be balanced to incorporate a similar number of cells on each electrode to maintain statistical significance. Using the same substrate area and with minor revisions to the mask and packaging scheme, it would be possible to increase the number of electrodes by a factor of two. Beyond this, alternative electrode geometries and routing schemes would have to be explored to enable more effective electrode placement. To completely pack the substrate with individually addressable electrodes would require significantly more challenging fabrication schemes which would not be worth pursuing.

Moving towards an inverted microscopy platform. The screens were performed using an automated microscopy system for read out. This system was based on an upright microscopy platform. As the electrode structures are transparent, assay read out could equally be performed on an inverted microscopy system. The inverted microscopy system is more commonly used for live-cell imaging and is compatible with integrated microscopy incubation systems. Inverted microscopy systems also enable phase contrast imaging which is more amenable to brightfield autofocus techniques. This could potentially simplify the design of the platform as autofocus

structures would no longer be required and instead autofocus could be performed on live cells on each electrode structure (using phase contrast images).

Programmable waveform generation system. The current platform utilizes a single waveform generation system that is switched between electrodes. This results in assays being performed sequentially. To perform the assays simultaneously a custom waveform generation system could be designed using field programmable gate arrays (FPGAs). Such a system could read previously stored waveform values from on-board memory and use them to construct waveforms. This would reduce the overall assay time and ensure that all cells have experienced the exact same conditions in the incubation system. This approach was not investigated during the course of this thesis as the design of such system poses a considerable engineering challenge but is certainly feasible. The most significant challenge for building such a system would be the design for waveforms above 10 MHz which would require careful consideration of board-level layout techniques. As the effects of fields higher than 10 MHz is also of considerable interest, the trade-off between longer assay time and an off-the shelf waveform generation system versus a shorter assay time and custom-designed waveform generation system could be more palatable.

6.2.5 Electric field impact on cellular physiology

Genome-wide expression analysis. As previously mentioned the electric field effects have been measured with 16 different electrode sites. Ideally, it would be interesting to understand all the genes that are affected by such electric field stimulations. Genome-wide analysis using microarrays could be one possible technique that could be used to perform this type of an experiment. Similarly, quantitative PCR arrays (StellArray, Lonza, Inc.) could also be used to study a subset (96 or 384) of targeted genes. Performing these types of experiments would involve two critical steps – (1) repeating conditions on a number of electrodes and then pooling those samples, and (2) harvesting cells from the electrodes. As the electrodes are not fluidically addressable, other techniques might be used to access the cells. Thermosensitive polymers that could be cooled to release the cells could be used. The cells could then subsequently be isolated by unclamping the electrode structures in fluid, to prevent disruption of the cells. Most likely, such a scheme would have to involve the use of most of the electrodes for a single condition. This would make the task of comparing large gene expression datasets across conditions challenging and increasingly time consuming. In all, this would only be feasible if a small set of conditions were considered to be more important than others for the study of electric field effects.

DNA damage analysis. The experiments outlined in the thesis cover the effects on electric fields on cellular stress. With sufficient recovery times, cells can recover from these stressful conditions. It would be interesting to determine if there are more permanent effects such as DNA damage that occur at higher field strengths. This might be investigated using specifically constructed reporter cell lines. Understanding the absolute limits for electric field manipulation

and exposure would provide invaluable insight to both designer and end-users of such microsystems.

Electric-field effects across lineages. By propagating cell lines in different lineages it would be interesting if there are differences in the thresholds of stress experienced by these different lineages. Are certain lineages more sensitive to electric field based manipulation? This could point to differences in how cell process electric fields, and might point to differences in the intrinsic electrical properties of cells. This could also provide end-users with important information regarding the types of cell lines that are most robust when manipulated with such electric-field mechanisms.

Designing cell-friendly traps. The system developed in this thesis is a simple parallel plate geometry and was chosen as such to be generalized to any other electrical trap design (at least in terms of peak field strengths). By determining the optimal field conditions that could be tolerated by the cells, these field strengths could serve as additional boundary conditions when modeling traps [177]. This would allow for the comparisons of traps based on cell health impact. This could have considerable impact on the design of dielectrophoretic traps.

References

1. Taff, B.M., Desai, S. P., and Voldman, J., *Electroactive hydrodynamic weirs for microparticle manipulation and patterning* Applied Physics Letters, 2009. **94**.
2. Taylor, P., Xu, C., Fletcher, P. D. I., and Paunov, V. N. , *Fabrication of 2D arrays of giant liposomes on solid substrates by microcontact printing.* Physical Chemistry Chemical Physics, 2003. **5**: p. 4918-4922.
3. Wang, Y.-C., Choi, M. H., and Han, J., *Two-dimensional protein separation with advanced sample and buffer isolation using microfluidic valves.* Analytical Chemistry, 2004. **76**: p. 4426-4431.
4. Hawkins, B.G., Smith, A. E., Syed, Y. A., and Kirby, B. J. , *Continuous-flow particle separation by 3D insulative dielectrophoresis using coherently-shaped, DC-biased, AC electric fields.* Analytical Chemistry, 2007. **79**(19): p. 7291-7300.
5. Vahey, M.D., and Voldman, J., *A new equilibrium method for continuous flow cell-sorting using dielectrophoresis.* Analytical Chemistry, 2008. **80**(9): p. 3135-3143.
6. Gomez-Sjoberg, R., Leyrat, A. A., Pirone, D. M., Chen, C. S., and Quake, S. R., *Versatile, fully automated, microfluidic cell culture system.* Analytical Chemistry, 2007. **79**(22): p. 8557-8563.
7. Wheeler, A.R., Throndset, W. R., Whelan, R. J., Leach, A. M., Zare, R. N., Liao, Y. H., Farrell, K., Manger, I. D., Daridon, A. , *Microfluidic device for single-cell analysis.* Analytical Chemistry, 2003. **75**(14): p. 3581-3586.
8. Kim, L.Y., Vahey, M. D., Lee, H.-Y., and Voldman, J., *Microfluidic arrays for logarithmically perfused embryonic stem cell culture.* Lab Chip, 2006. **6**: p. 394-406.
9. Sampattavanich, S., Taff, B. M., Desai, S. P., and Voldman, J. *Organizing complex multicellular constructs using stencil-delineated electroactive patterning (S-DEP).* in *Micro Total Analysis Systems*. 2008. San Diego, CA.
10. Sivaraman, A., Leach, J. K., Townsend, S., Iida, T., Hogan, B. J., Stolz, D. B., Fry, R., Samson, L. D., Tannenbaum, S. R., and Griffith, L. G., *A microscale in vitro physiological model of the liver: predictive screens for drug metabolism and enzyme induction.* Current Drug Metabolism, 2005. **6**(6): p. 569-591.
11. Takayama, S., Ostuni, E., LeDuc, P., Naruse, K., Ingber, D. E., and Whitesides, G. M., *Laminar flows: Subcellular positioning of small molecules.* Nature, 2001. **411**: p. 1016.
12. Lucchetta, E.M., Lee, J. H., Fu, L. A., Patel, N. H., and Ismagilov, R. F., *Dynamics of Drosophila embryonic patterning network perturbed in space and time using microfluidics.* Nature, 2005. **434**: p. 1134-1138.
13. Rezvin, A., Sekine, K., Sin, A., Tompkins, R. G., and Toner, M., *Development of a microfabricated cytometry platform for characterization and sorting of individual leukocytes.* Lab Chip, 2005. **5**: p. 30-37.
14. Voldman, J., Gray, M. L., Toner, M., and Schmidt, M. A., *A microfabrication-based dynamic array cytometer.* Analytical Chemistry, 2002. **74**: p. 3362-3371.
15. Hu, H., Gaudet, S., Schmidt, M. A., and Jensen, K. F., *A microfabricated device for subcellular organelle sorting.* Analytical Chemistry, 2004. **76**: p. 5705-5712.
16. El-Ali, J., Sorger, P. K, and Jensen, K. F., *Cells on chips.* Nature, 2006. **442**: p. 403-411.
17. Bhagat, A.A.S., P. Jothimuthu, and I. Papautsky. *Photodefinable PDMS for rapid prototyping of disposable lab-on-a-chip systems.* in *Micro Total Analysis Systems 2006.* 2006. Tokyo, Japan: Society for Chemistry and Micro-Nano Systems (CHEMINAS).

18. Choi, K.M., *Photopatternable silicon elastomers with enhanced mechanical properties for high-fidelity nanoresolution soft lithography.* Journal of Physical Chemistry B, 2005. **109**(46): p. 21525-31.
19. Choi, K.M. and J.A. Rogers, *A photocurable poly(dimethylsiloxane) chemistry designed for soft lithographic molding and printing in the nanometer regime.* Journal of the American Chemical Society, 2003. **125**(14): p. 4060-4061.
20. Singh, A.K., Cummings, E. B., and Throckmorton, D. J., *Fluorescent liposome flow markers for microscale particle-image velocimetry.* Analytical Chemistry, 2001. **73**: p. 1057-1061.
21. Desai, S.P., Taff, B. M., and Voldman, J. , *A photopatternable silicone for biological microsystems.* Langmuir, 2008. **24**: p. 575-581.
22. Lee, J.N., et al., *Compatibility of mammalian cells on surfaces of poly(dimethylsiloxane).* Langmuir, 2004. **20**(26): p. 11684-11691.
23. Peterson, S.L., et al., *Poly(dimethylsiloxane) thin films as biocompatible coatings for microfluidic devices: Cell culture and flow studies with glial cells.* Journal of Biomedical Materials Research - Part A, 2005. **72**(1): p. 10-18.
24. Quake, S.R. and A. Scherer, *From micro- to nanofabrication with soft materials.* Science, 2000. **290**(5496): p. 1536-40.
25. Choi, K.M. and J.A. Rogers. *Novel chemical approach to achieve advanced soft lithography by developing new stiffer, photocurable PDMS stamp materials.* in *Nanoengineered Assemblies and Advanced Micro-Nanosystems, 13-16 April 2004.* 2004. San Francisco, CA, USA: Materials Research Society.
26. Jhanvi, H.D., S. Yang, and P.J. Butler, *Improved nanometer-scale particle tracking in optical microscopy using microfabricated fiduciary posts.* BioTechniques, 2007. **42**(4): p. 437-440.
27. Chronis, N. and L.P. Lee, *Electrothermally activated SU-8 microgripper for single cell manipulation in solution.* Journal of Microelectromechanical Systems, 2005. **14**(4): p. 857-63.
28. Salazar, G.T.a., et al., *Micropallet arrays for the separation of single, adherent cells.* Analytical Chemistry, 2007. **79**(2): p. 682-687.
29. Krassow, H., F. Campabadal, and E. Lora-Tamayo. *Wafer level packaging of silicon pressure sensors.* in *Transducers '99: 10th International Conference on Solid State Sensors and Actuators, 7-10 June 1999*

Sensors and Actuators A (Physical). 2000. Sendai, Japan: Elsevier.
30. Vanden Bulcke, M., et al. *Introducing a silicone under the bump configuration for stress relief in a wafer level package.* in *Proceedings of the 5th Electronics Packaging Technology Conference (EPTC 2003), 10-12 Dec. 2003.* 2003. Singapore: IEEE.
31. Meynen, H., et al. *Ultra low stress and low temperature patternable silicone materials for applications within microelectronics.* in *Materials for Advanced Metallization, Mar 7-10 2004.* 2004. Brussels, Belgium: Elsevier, Amsterdam, 1000 AE, Netherlands.
32. Harkness, B.R., et al. *Photopatternable silicone compositions for electronic packaging applications.* in *Advances in Resist Technology and Processing XXI, 23-24 Feb. 2004*

Proceedings of the SPIE - The International Society for Optical Engineering. 2004. Santa Clara, CA, USA: SPIE-Int. Soc. Opt. Eng.
33. Di Carlo, D., Wu, L. Y., Lee, L. P., *Dynamics single cell culture array.* Lab Chip, 2006. **6**: p. 1445-1449.

34. Di Carlo, D., Aghdam, N., Lee, L. P., *Single-cell enzyme concentrations, kinetics, and inhibition analysis using high-density hydrodynamic cell isolation arrays.* Analytical Chemistry, 2006. **78**: p. 4925-4930.
35. Folch, A., et al., *Microfabricated elastomeric stencils for micropatterning cell cultures.* Journal of Biomedical Materials Research, 2000. **52**(2): p. 346-353.
36. Ostuni, E., et al., *Patterning Mammalian Cells Using Elastomeric Membranes.* Langmuir, 2000. **16**(20): p. 7811-7819.
37. Shaw, J.M., et al., *Negative photoresists for optical lithography.* IBM Journal of Research and Development, 1997. **41**(1-2): p. 81-94.
38. Gauthier, T.D., et al., *FLUORESCENCE QUENCHING METHOD FOR DETERMINING EQUILIBRIUM CONSTANTS FOR POLYCYCLIC AROMATIC HYDROCARBONS BINDING TO DISSOLVED HUMIC MATERIALS.* Environmental Science and Technology, 1986. **20**(11): p. 1162-1166.
39. Hasegawa, M., et al., *Molecular aggregation and fluorescence spectra of aromatic polyimides.* European Polymer Journal, 1989. **25**(4): p. 349-354.
40. Nohta, H., et al., *Aromatic glycinonitriles and methylamines as pre-column fluorescence derivatization reagents for catecholamines.* Analytica Chimica Acta, 1997. **344**(3): p. 233.
41. Backhus, D.A. and P.M. Gschwend, *Fluorescent polycyclic aromatic hydrocarbons as probes for studying the impact of colloids on pollutant transport in groundwater.* Environmental Science and Technology, 1990. **24**(8): p. 1214-1223.
42. Nie, S., R. Dadoo, and R.N. Zare, *Ultrasensitive Fluorescence Detection of Polycyclic Aromatic Hydrocarbons in Capillary Electrophoresis.* Analytical Chemistry, 1993. **65**(24): p. 3571-3575.
43. Pinto, C.G., J.L.P. Pavon, and B.M. Cordero, *Cloud Point Preconcentration and High-Performance Liquid Chromatographic Determination of Polycyclic Aromatic Hydrocarbons with Fluorescence Detection.* Analytical Chemistry, 1994. **66**(6): p. 874-881.
44. Roos, W.H., et al., *Freely suspended actin cortex models on arrays of microfabricated pillars.* Chemphyschem, 2003. **4**(8): p. 872-7.
45. Terao, K., H. Kabata, and M. Washizu, *Extending chromosomal DNA in microstructures using electroosmotic flow.* Journal of Physics: Condensed Matter, 2006. **18**(18): p. 653-63.
46. Jackman, R.J., et al., *Microfluidic systems with on-line UV detection fabricated in photodefinable epoxy.* Journal of Micromechanics and Microengineering, 2001. **11**(3): p. 263-9.
47. Fox, M.B., et al., *Electroporation of cells in microfluidic devices: A review.* Analytical and Bioanalytical Chemistry, 2006. **385**(3): p. 474-485.
48. Skulan, A.J., et al., *Fabrication and analysis of spatially uniform field electrokinetic flow devices: Theory and experiment.* Analytical Chemistry, 2005. **77**(21): p. 6790-6797.
49. Rowe, L., et al., *Active 3-D microscaffold system with fluid perfusion for culturing in vitro neuronal networks.* Lab Chip, 2007. **7**(4): p. 475-82.
50. Jenke, M.G., et al., *Micropositioning and microscopic observation of individual picoliter-sized containers within SU-8 microchannels.* Microfluidics and Nanofluidics, 2007. **3**(2): p. 189-194.

51. Wu, Z.-Z., Y. Zhao, and W.S. Kisaalita, *Interfacing SH-SY5Y human neuroblastoma cells with SU-8 microstructures.* Colloids and Surfaces B (Biointerfaces), 2006. **52**(1): p. 14-21.
52. Wilk, S.J., et al. *Microfabricated silicon apertures for ion channel measurement.* in *2005 NSTI Nanotechnology Conference and Trade Show. NSTI Nanotech 2005, 8-12 May 2005.* 2005. Anaheim, CA, USA: Nano Science and Technology Institute.
53. Belanger, M.-C. and Y. Marois, *Hemocompatibility, biocompatibility, inflammatory and in vivo studies of primary reference materials low-density polyethylene and polydimethylsiloxane: A review.* Journal of Biomedical Materials Research, 2001. **58**(5): p. 467-477.
54. Kotzar, G., et al., *Evaluation of MEMS materials of construction for implantable medical devices.* Biomaterials, 2002. **23**(13): p. 2737-2750.
55. Tang, L., et al., *Anti-inflammatory properties of triblock siloxane copolymer-blended materials.* Biomaterials, 1999. **20**(15): p. 1365-1370.
56. Voskerician, G., et al., *Biocompatibility and biofouling of MEMS drug delivery devices.* Biomaterials, 2003. **24**(11): p. 1959-1967.
57. Weisenberg, B.A. and D.L. Mooradian, *Hemocompatibility of materials used in microelectromechanical systems: Platelet adhesion and morphology in vitro.* Journal of Biomedical Materials Research, 2002. **60**(2): p. 283-291.
58. Lindon, J.N., et al., *In vivo assessment in sheep of thromboresistant materials by determination of platelet survival.* Circ Res, 1980. **46**(1): p. 84-90.
59. Predecki, P., L. Life, and M.M. Newman, *PREVENTION OF PLATELET ADHESION TO POROUS SURFACES.* Journal of Biomedical Materials Research, 1980. **14**(4): p. 405-415.
60. Fissell, W.H., et al., *Differentiated growth of human renal tubule cells on thin-film and nanostructured materials.* ASAIO Journal, 2006. **52**(3): p. 221-227.
61. Albrecht, D.R., et al., *Photo- and electropatterning of hydrogel-encapsulated living cell arrays.* Lab on a Chip, 2005. **5**(1): p. 111-18.
62. Bevis, B.J. and B.S. Glick, *Rapidly maturing variants of the Discosoma red fluorescent protein (DsRed).* Nat Biotechnol, 2002. **20**(1): p. 83-7.
63. Kim, L., et al., *Microfluidic arrays for logarithmically perfused embryonic stem cell culture.* Lab on a Chip, 2006. **6**(3): p. 394-406.
64. Ihle, J.N., et al., *Procedures for the purification of interleukin 3 to homogeneity.* J Immunol, 1982. **129**(6): p. 2431-6.
65. Desai, S.P., Vahey, M. D., and Voldman, J., *Electrically addressable vesicles - Tools for dielectrophoresis metrology.* Langmuir, 2009. **25**(6): p. 3867-3875.
66. Long, M.S., Jones, C., Helfrich, M. R., Mangeney-Slavin, L. K., and Keating, C. D. , *Dynamic microcompartmentation within synthetic cells.* Proceedings of the National Academy of Sciences of the United States of America, 2005. **102**: p. 5920-5925.
67. Long, M.S., Cans, A.-S. and Keating, C. D., *Budding and asymmetric protein microcompartmentation in giant vesicles containing two aqueous phases.* Journal of American Chemical Society, 2008. **130**: p. 756-762
68. Upadhyay, A., Chabot, J. R., Andreeva, A., Samadani, A. and van Oudenaarden, A., *Probing polymerization forces by using actin-propelled lipid vesicles.* Proceedings of the National Academy of Sciences of the United States of America, 2003. **100**: p. 4521-4525.

69. Noireaux, V.a.L., A. , *A vesicle bioreactor as a step toward an artificial cell assembly.* Proceedings of the National Academy of Sciences of the United States of America, 2004. **101**: p. 17669-17674.
70. Haluska, C.K., Riske, K. A., Marchi-Artzner, V., Lehn, J. -M., Lipowsky, R. and Dimova, R., *Timescales of membrane fusion revealed by direct imaging of vesicle fusion with high temporal resolution.* Proceedings of the National Academy of Sciences of the United States of America, 2006. **103**: p. 15841-15846.
71. Tan, Y.-C., Hettiarachichi, K., Siu, M., Pan, Y. -R., and Lee, A. P., *Controlled microfluidic encapsulation of cells, proteins, and microbeads in lipid vesicles.* . Journal of American Chemical Society, 2006. **128**: p. 5656-5658.
72. Yoshikawa, K.a.N., S. -I., *Giant phospholipid vesicles entrapping giant DNA.* Giant Vesicles. Perspectives in supramolecular assemblies, 200. **6**: p. 313-317.
73. Ratanabanangkoon, P., Gropper, P., Merkel, M., Sackmann, E., and Gast, A. P., *Two-dimensional streptavidin crystals on giant lipid bilayer vesicles.* Langmuir, 2002. **18**: p. 4270-4276.
74. Ratanabanangkoon, P., Gropper, P., Merkel, M., Sackmann, E., and Gast, A. P., *Mechanics of streptavidin-coated giant lipid bilayer vesicles: A micropipet study.* Langmuir, 2003. **19**: p. 1054-1062.
75. Albrecht, D.R., Underhill, G. H., Mendelson, A., and Bhatia, S. N. , *Multiphase electropatterning of cells and biomaterials.* Lab Chip, 2007. **7**: p. 702-709.
76. Gray, D.S., Tan, J., Voldman, J., and Chen, C. S., *Dielectrophoretic registration of living cells to a microelectrode array.* Biosensors and Bioelectronics, 2004. **19**: p. 1765-1774.
77. Ho, C.-T., Lin, R.-Z., Chang, W.-Y., Chang, H.-W., and Liu, C.-H., *Rapid heterogeneous liver-cell on-chip patterning via enhanced field-induced dielectrophoresis trap.* Lab Chip, 2006. **6**: p. 724-734.
78. Gadish, N.a.V., J., *High-throughput positive-dielectrophoretic bioparticle microconcentrator.* Analytical Chemistry, 2006. **78**(22): p. 7870-7876.
79. Lapizco-Encinas, B.H., Simmons, B. A., Cummings, E. B., and Fintschenko, Y. , *Dielectrophoretic concentration and separation of live and dead bacteria in an array of insulators.* Analytical Chemistry, 2004. **76**: p. 1571-1579.
80. Yang, L., Banada, P. P., Chatni, M. R., Lim, K. S., Bhunia, A. K., Ladisch, M. and Bashir, R., *A multifunctional microfluidic system for dielectrophoretic concentration coupled with immuno-capture of low numbers of Listeria monocytogenes.* Lab Chip, 2006. **6**: p. 896-905.
81. Braschler, T., Demierre, N., Nascimento E., Silva, T., Oliva, A. G., and Renaud, P. , *Continuous separation of cells by balanced dielectrophoretic forces at multiple frequencies.* Lab Chip, 2008. **8**: p. 280-286.
82. Taff, B.M., and Voldman, J., *A scalable and addressable positive-dielectrophoretic cell-sorting array.* Analytical Chemistry, 2005. **77**: p. 7976-7983.
83. Vykoukal, J., Vykoukal, D. M., Sharma, S., Becker, F. F., and Gascoyne, P. R. C., *Dielectrically addressable microspheres engineered using self-assembled monolayers.* Langmuir, 2003. **19**: p. 2425-2433.
84. Angelova, M.I.a.D., D. S., *Liposome electroformation.* Faraday Discussions Chemical Society, 1986. **81**: p. 303-312.
85. Jones, T.B., *Electromechanics of Particles.* 1995, Cambridge: Cambridge Universtiy Press.

86. Gascoyne, P.R.C., Wang, X.-B., Huang, Y., and Becker, F. F., *Dielectrophoretic separation of cancer cells from blood.* IEEE Transactions on Industry Applications, 1997. **33**(3): p. 670-678.
87. Hermanson, K.D., Lumsdon, S. O., Williams, J. P., Kaler, E. W., and Velev, O. D., *Dielectrophoretic assembly of electrically functional microwires from nanoparticle suspensions.* Science, 2001. **294**: p. 1082-1086.
88. Funakoshi, K., Suzuki, H., and Takeuchi, S., *Formation of giant lipid vesicle-like compartments from a planar lipid membrane by a pulse jet flow.* Journal of American Chemical Society, 2007. **129**: p. 12608-12609.
89. Needham, D., *Permeability and stability of lipid bilayers*, ed. E.A.a.S. Disalve, S. A. 1995, Boca Raton, FL: CRC Press.
90. Nikolov, V., Lipowsky, R., and Dimova, R. , *Behavior of giant vesicles with anchored DNA molecules.* Biophysical Journal, 2007. **92**: p. 4356-4368.
91. Sapper, A.a.J., A., *Electrially induced deformation of giant liposomes monitored by thickness shear mode resonators.* Langmuir, 2006. **22**: p. 10869-10873.
92. Dominak, L.M.a.K., C. D., *Polymer encapsulation within giant lipid vesicles.* Langmuir, 2007. **23**: p. 7148-7154.
93. Helfrich, M.R., Mangeney-Slavin, L. K., Long, M. S., Djoko, K. Y., and Keating, C. D., *Aqueous phase separation in giant vesicles.* Journal of American Chemical Society, 2002. **124**: p. 13374-13375.
94. Needham, D.a.K., D. H., *PEG-covered lipid surfaces, bilayers and monolayers.* Colloids and Surfaces B, 2000. **18**: p. 183-195.
95. Korlach, J., Reichle, C., Muller, T., Schnelle, T., and Webb, W. W., *Trapping, deformation and rotation of giant unilamellar vesicles in octode dielectrophoretic field cages.* Biophysical Journal, 2005. **89**: p. 554-562.
96. Riske, K.A., and Dimova, R. , *Electrical pulses induce cylindrical deformations on giant vesicles in salt solutions.* Biophysical Journal, 2006. **91**: p. 1778-1786.
97. Aranda, S., Riske, K., Lipowsky, R., and Dimova, R., *Morphological transitions of vesicles induced by AC electric fields.* Biophysical Journal, 2008. **95**: p. L19-L21.
98. Pethig, R., *Dielectrophoresis: Using Inhomogeneous AC Electrical Fields to Separate and Manipulate Cells.* Critical Reviews in Biotechnology, 1996. **16**(4): p. 331 - 348.
99. Ashkin, A., *Optical trapping and manipulation of neutral particles usingâ€‰lasers.* Proceedings of the National Academy of Sciences of the United States of America, 1997. **94**(10): p. 4853-4860.
100. Chen, C.S., et al., *Geometric Control of Cell Life and Death.* Science, 1997. **276**(5317): p. 1425-1428.
101. Perez, O.D. and G.P. Nolan, *Simultaneous measurement of multiple active kinase states using polychromatic flow cytometry.* Nat Biotech, 2002. **20**(2): p. 155-162.
102. Schnelle, T., Hagedorn, R., Fuhr, G., Fiedler, S. & Muller, T, *Three-Dimensional electric-field traps for manipulation of cells - calculation and experimental verification.* Biochimica Et Biophysica Acta, 1993. **1157**: p. 127-140.
103. Fuhr, G., *Levitation, holding, and rotation of cells within traps made by high-frequency fields.* Biochimica Et Biophysica Acta 1992. **1108**: p. 215-223.
104. Mittal, N., Rosenthal, A., Voldman, J., *nDEP microwells for single-cell patterning in physiological media.* Lab Chip, 2007. **7**(6): p. 681-694.

105. Matsue, T., Matsumoto, N., Uchida, I., *Rapid micropatterning of living cells by dielectrophoretic force.* Electrochim. Acta, 1997. **42**: p. 2131-2147.
106. Suehiro, J.P., R. , *The dielectrophoretic movement and positioning of a biological cell using a three-dimensional grid electrode system.* Journal of Physics D-Applied Physics 1998. **31**: p. 3298-3305.
107. Taff, B.M., *Microsystems platforms for array-based single-cell biological assays*, in *Electrical Engineering and Computer Science.* 2008, Massachusetts Institute of Technology: Cambridge, MA.
108. Taff, B.M. and J. Voldman, *A scalable addressable positive-dielectrophoretic cell-sorting array.* Analytical Chemistry, 2005. **77**(24): p. 7976-7983.
109. Titushkin, I.a.C., M., *Regulation of cell cytoskeleton and membrane mechanics by electric field: Role of linker proteins.* Biophysical Journal, 2009. **96**: p. 717-728.
110. Lindquist, S., *The heat shock response.* Annual Review Biochemistry, 1986. **55**: p. 1151-1191.
111. Craig, E.A., *The heat shock response.* CRC Critical Reviews in Biochemistry, 1985. **18**: p. 239-280.
112. Burdon, R.H., *Heat-shock and the heat-shock proteins.* Biochemical Journal, 1986. **240**: p. 313-324.
113. Subjeck, J.R.a.S., T. T., *Stress protein systems of mammalian cells.* Journal of Physiology, 1986. **250**: p. C1-C17.
114. Jones, T.B., IEEE Proceedings-Nanobiotechnology, 2003. **150**(2): p. 37-39.
115. Weiss, T.F., *Cellular Biophysics.* 1996, Cambridge, MA: MIT Press.
116. Tsong, T.Y., *Molecular recognition and processing of periodic signals in cells - stud of activation of membrane ATPases by alternating electric fields.* Biochimica Et Biophysica Acta, 1992. **1113**: p. 1113.
117. Catterall, W.A., *Structure and function of voltage gated ion channels.* Annual Review of Biochemistry, 1995. **64**: p. 493-531.
118. Zimmerman, U., *Electrical breakdown, electropermeabilization and electrofusion.* Reviews of Physiology, Biochemistry and Pharmacology, 1986. **105**: p. 175-256.
119. Schwan, H.P., *Linear and nonlinear electrode polarization and biological materials.* Annals of Biomedical Engineering, 1992. **20**(3): p. 269-288.
120. Voldman, J., Toner, M., Gray, M. L., Schmidt, M. A., *Design and analysis of extruded quadraploar dielectrophoretic traps.* Journal of Electrostatics, 2003. **57**: p. 69-90.
121. Kuhn, B., Fromherz, P., and Denk, W., *High sensitivity of stark-shift voltage-sensing dyes by one- or two-photon excitation near the red spectral edge.* Biophysical Journal, 2004. **87**: p. 631-639.
122. Frey, W., White, J. A., Price, R. O., Blackmore, P. F, Joshi, R. P., Nuccitelli, R., Beebe, S. J., Schoenbach, K. H. and Kolb, J. F., *Plasma membrane voltage changes during nanosecond pulsed electric field exposure.* Biophysical Journal, 2006. **90**: p. 3608-3615.
123. Riley, P.A., *Free radicals in biology: oxidative stress and the effects of ionizing radiation.* International Journal of Radiation Biology, 1994. **65**(1): p. 27-33.
124. Wiseman, H., and Halliwell, B. , *Damage to DNA by reactive oxygen and nitrogen species: role in inflammatory disease and progression to cancer.* Biochemical Journal, 1996. **313**: p. 17-29.

125. Ridley, A.J., Schwartz, M. A., Burridge, K., Firtel, R. A., Ginsberg, M. H., Borsiy, G., Parsons, J. T., and Horwitz, A. R. , *Cell migration: Integrating signals from front to back.* Science, 2003. **302**: p. 1704-1709.
126. Altizer, A.M., Moriarty, L. J., Bell, S. M., Schreiner, C. M., Scott, W. J., and Borgens, R. B. , *Endogenous electric current is associated with normal development of the vertebrate limb.* Developmental Dynamics, 2001. **221**(4): p. 391-401.
127. Hotary, K.B., and Robinson, K. R., *Evidence of a role for endogenous electrical fields in chick embryo development.* Development, 1992. **114**(4): p. 985-996.
128. Jenkins, L.S., Duerstock, B. S., Borgens, R. B., *Reduction of the current of injury leaving the amputation inhibits limb regeneration in the red spotted newt* Dev Biol, 1996. **178**: p. 251-262.
129. Borgens, R.B., Vanable, J. W. Jr., Jaffe, L. F., *Bioelectricity and regeneration: Initiation of frog limb regeneration by minute currents.* J. Exp. Zool., 1977. **200**: p. 403-416.
130. Alvarez, O.M., Mertz, P. M., Smerbeck, R. V., Eaglstein, W. H., *The healing of superficial wounds is stimulated by external electricl current.* J. Invest. Dermatol., 1983. **81**: p. 144-148.
131. Borgens, R.B., *Electrically mediated regeneration and guidance of adult mammalian spinal axons into polymeric channels.* Neuroscience, 1999. **91**: p. 251-264.
132. Heida, T., Rutten, W. L, and Marani, E. , *Experimental investigation on neural cell survival after dielectrophoretic trapping.* Archives of Physiology and Biochemistry, 2002. **110**: p. 373-382.
133. Glasser, H.a.F., G., *Cultivation of cells under strong ac-electric field - differentiation between heating and trans-membrane potential effects.* . Bioelectrochemistry and Bioenergetics, 1998. **47**: p. 301-310.
134. Fuhr, G., Glasser, H., Muller, T., and Schnelle, T. , *Cell manipulation and cultivation under AC electric-field influence in highly conductive culture media.* Biochimica Et Biophysica Acta-General Subjects, 1994. **1201**: p. 353-360.
135. Doscoslis, A., Kalogerakis, N. and Behie, L. A. , *Dielectrophoretic forces can be safely used to retain viable cells in perfusion cultures of animal cells.* Cytotechnology, 1999. **30**: p. 133-142.
136. Archer, S., Li, T. T., Evans, T. A, Britland, S. T., and Morgan, H., *Cell reactions to dielectrophoretic manipulation.* Biochemical and biophysical research communications, 1999. **257**: p. 687-698.
137. Fuhr, G., Schnelle, T., Muller, T., Hitzler, H., Monajembashi, S., and Greulich, K. O., Applied Physics A-Materials Science and Processing, 1998. **67**.
138. Wang, X., Yang, K., Gascoyne, P. R. C., *Role of peroxide in AC electrical field exposure effects on Friend murine erythroleukemia cells during dielectrophoretic manipulations.* Biochimica Et Biophysica Acta, 1999. **1426**(1): p. 53-68.
139. Moore GE, G.R., Franklin HA, *Culture of normal human lymphocytes.* JAMA, 1967. **199**(8): p. 519-524.
140. Li, X., Kolega, J., *Effects of direct current electric fields on cell migration and actin filament distribution in bovine vascular endothelial cells.* Journal of Vascular Research, 2002. **39**: p. 391-404.
141. Bukau, B., Deuerling, E., Pfund, C., Craig, E. A., *Getting newly synthesized proteins into shape.* Cell, 2000. **101**(2): p. 119-122.

142. Carper. S. W., D., J. J., and Gerner, E. W. , *Heat-shock proteins in thermotolerance and other cellular processes.* Cancer Research, 1987. **47**: p. 5249-5255.
143. Baugh, L.R., Hill, A. A. , Brown, E. L., and Hunter, C. P., *Quantitative analysis of mRNA amplification by in vitro transcription.* Nucleic Acids Research, 2001. **29**.
144. Schnelle, T., Muller, T., Voigt, A. Reimer, K, Wagner, B., and Fuhr, G., *Adhesion-Inhibited Surfaces. Coated and Uncoated Interdigitated Electrode Arrays in the Micrometer and Submicrometer Range.* Langmuir, 1996. **12**(3): p. 801-809.
145. El-Ali, J., Gaudet, S., Gunther, A., Sorger, P. K, and Jensen, K. F., *Cell Stimulus and Lysis in a Microfluidic Device with Segmented Gas–Liquid Flow.* Analytical Chemistry, 2005. **77**(11): p. 3629-3636.
146. Le Moal, E., Fort, E., Leveque-Fort, S., Cordelieres, F. P, Fontaine-Aupart, M. -P., Ricolleau, *Enhanced fluorescence cell imaging with metal coated slides.* Biophysical Journal, 2007. **92**(6): p. 2150-2161.
147. Ottesen, E., Hong, J. W., Quake, S. R., and Leadbetter, J. R. , *Microfluidic Digital PCR Enables Multigene Analysis of Individual Environmental Bacteria.* Science, 2006. **314**: p. 1464-1467.
148. Ostu, N., *A threshold selection method from gray-level histograms.* IEEE Trans. Sys. Man. Cyber, 1979. **9**: p. 62-66.
149. Mrksich, M., Dike, L. E., Tien, J., Ingber, D. E., and Whitesides, G. M., *Using microcontact printing to pattern the attachment of mammalian cells to self-assembled monolayers of alkanethiolates on transparent films of gold and silver.* Experimental Cell Research, 1997. **235**: p. 305-313.
150. Guo, L.-H., Facci, J. S., McLendon, G., Mosher, R., *Effect of gold topography and surface pretreatment on the self-assembly of alkanethiol monolayers.* Langmuir, 1994. **10**: p. 4588-4593.
151. Blagovic, K., Desai, S. P., Kim, L. Y., Voldman, J. . *Patterned polystyrene substrates for integrates microfluidic cell culture devices.* in *Annual meeting of Biomedical Engineering Society*. 2008. St. Louis, MO: Biomedical Engineering Society.
152. Dai, C., Whitesell, L., Rogers, A. B., and Lindquist, S., *Heat Shock Factor 1 is a powerful multifaceted modifier of carcinogenesis.* Cell, 2007. **130**: p. 1005-1018.
153. Zeng, X.-C., Bhasin, S., Wu, X., Lee, J-G., Maffi, S., Nichols, C. J., Lee, K. J., Taylor, J. P., Greene, L. E., and Eisenberg, E., *Hsp70 dynamics in vivo: effect of heat shock and protein aggregation.* Journal of Cell Science, 2004. **117**(21): p. 4991-5000.
154. Rajapandi, T., Wu, C., Eisenberg, E., Greene, L., *Characterization of D10S and K71E mutants of human cytosolic Hsp70.* Biochemistry, 1998. **37**(20): p. 7244-7250.
155. Mitra, S., Goren, E. M., Frelinger, J. G., and Foster, T. H., *Activation of Heat Shock Protein 70 Promoter with meso-Tetrahydorxyphenyl Chlorin Photodynamic Therapy Reporter by Green Fluorescent Protein In Vitro and In Vivo.* Photochemistry and Photobiology, 2003. **78**(6): p. 615-622.
156. Molina, A., Carpeaux, R., Martial, J. A., and Muller, M., *A transformed fish cell line expressing a green fluorescent protein-luciferase fusion gene responding to cellular stress.* Toxicology in Vitro, 2002. **16**: p. 201-207.
157. Ting, A.Y., Kain, K. H., Klemke, R. L., Tsien, R. Y., *Genetically encoded fluorescent reporters of protein tyrosine kinase activities in living cells.* Proceedings of the National Academy of Sciences of the United States of America, 2001. **98**(26): p. 15003-15008.

158. Frelin, C., Vigne, P., Lazdunski, M., *The amiloride-sensitive Na^+/H^+ antiport in 3T3 fibroblasts.* Journal of Biological Chemistry, 1983. **258**(10): p. 6272-6276.
159. Negulescu, P.A., et al., *Intracellular ion activities and membrane transport in parietal cells measured with fluorescent dyes*, in *Methods in Enzymology*. 1990, Academic Press. p. 38-81.
160. Soule, H.D.a.M., C. M., *A simplified methos for passage and long-term growth of human mammary epthelial cells.* In Vitro, 1986. **22**: p. 6-12.
161. Soule, H.D., Maloney, T. M., Wolman, S. R., Peterson, W. D. Jr, Brenz, R., McGrath, C. M., Russo, J., Pauley, R. J., Jones, R. F., and Brooks, S. C., *Isolation and characterization of a spotaneously immortalized human breast epthelial cell line, MCF-10.* Cancer Research, 1990. **50**: p. 6075-6086.
162. Belousov, V.V., Fradkov, A. F., Lukyanov, K. A., Staroverov, D. B., Shakhbazov, K. S, Terskikh, and Lukyanov, S. , *Genetically encoded fluorescent indicator for intracellular hydrogen peroxide.* Nature Methods, 2006. **3**(4): p. 281-286.
163. Skelley, A.M., Kirak, O., Suh, H., Jaenisch, R., and Voldman, J., *Microfluidic control of cell pairing and fusion.* Nature Methods, 2009. **6**: p. 147-152.
164. Vasanawala, F.H., Tsang, T., Fellah, A., Yorgin, P., Harris, D. T., *A novel expression vector induced by heat, γ-radiation and chemotherapy.* Gene Therapy and Molecular Biology, 2000. **5**: p. 1-8.
165. Rettig, J.R.a.F., A., *Large scale single-cell trapping and imaging using microwell arrays.* Analytical Chemistry, 2005. **77**(17): p. 5628-5634.
166. Rosenthal, A., A. Macdonald, and J. Voldman, *Cell patterning chip for controlling the stem cell microenvironment.* Biomaterials, 2007.
167. Kovac, J.R.a.V., J., *Intuitive, image-based cell sorting using opto-fluidic cell sorting.* Analytical Chemistry, 2007. **79**(24): p. 9321-9330.
168. Jaeger, M.S., Mueller, T., and Schnelle, T., *Thermometry in dielectrophoresis chips for contact-free cell handling.* Journal of Applied Physics D: Applied Physics, 2007. **40**: p. 95-105.
169. Mabrouk, E., Cuvelier, D., Brochard-Wyart, F., Nassoy, P., and Li, M.-H., *Bursting of sensitive polymerosomes induced by curling.* Proceedings of the National Academy of Sciences of the United States of America, 2009. **106**(18): p. 7294-7298.
170. Fleire, S.J., Goldman, J. P., Carrasco, Y. R., Weber, M., Bray, D., Batista, F. D., *B cell ligand discrimination through a spreading and contraction response.* Science, 2006. **312**(5774): p. 738-741.
171. Raucher, D.a.S., M. P., *Characteristics of a membrane reservoir buffering membrane tension.* Biophysical Journal, 1999. **77**(4): p. 1992-2002.
172. Souslova, E.A., Belousov, V. V., Lock, J., Stromblad, S., Kasparov, S., Bolshakov, A. P., Pinelis, V. G., Labas, Y. A., Lukyanov, S., Mayr, L. M., Chudakov, D. M., *Single fluorescent protein based Ca2+ sensors with increased dynamic range.* BMC Biotechnology, 2007. **7**(1): p. 37-47.
173. Di Carlo, D., Irimia, D., Tompkins, R. G., Toner, M., *Continuous inertial focusing, ordering and separation of particles in microchannels.* Proceedings of the National Academy of Sciences of the United States of America, 2007. **104**: p. 18892-18897.
174. Di Carlo, D., Edd, J. F., Irimia, D., Tompkins, R. G., Toner, M., *Equilibrium separation and filtration of particles using differential inertial focusing.* Analytical Chemistry, 2008. **80**: p. 2204-2211.

175. Barbulovic-Nad, I., Yang, H., Park, P. S., and Wheeler, A. R., *Digital microfluidics for cell-based assays.* Lab Chip, 2008. **8**: p. 519-526.
176. Chudakov, D.M., Verkhusha, V. V., Staroverov, D. B., Souslova, E. A., Lukyanov, S., Lukyanov, K. A., *Photoswitchable cyan fluorescent protein for protein tracking.* Nat Biotech, 2004. **22**(11): p. 1435-1439.
177. Rosenthal, A., Taff, B. M., and Voldman, J., *Quantitative modeling of dielectrophoretic traps.* Lab Chip, 2006. **6**: p. 508-515.